Investigations on Imaging Properties of Inorganic Scintillation Screens under Irradiation with High Energetic Heavy Ions
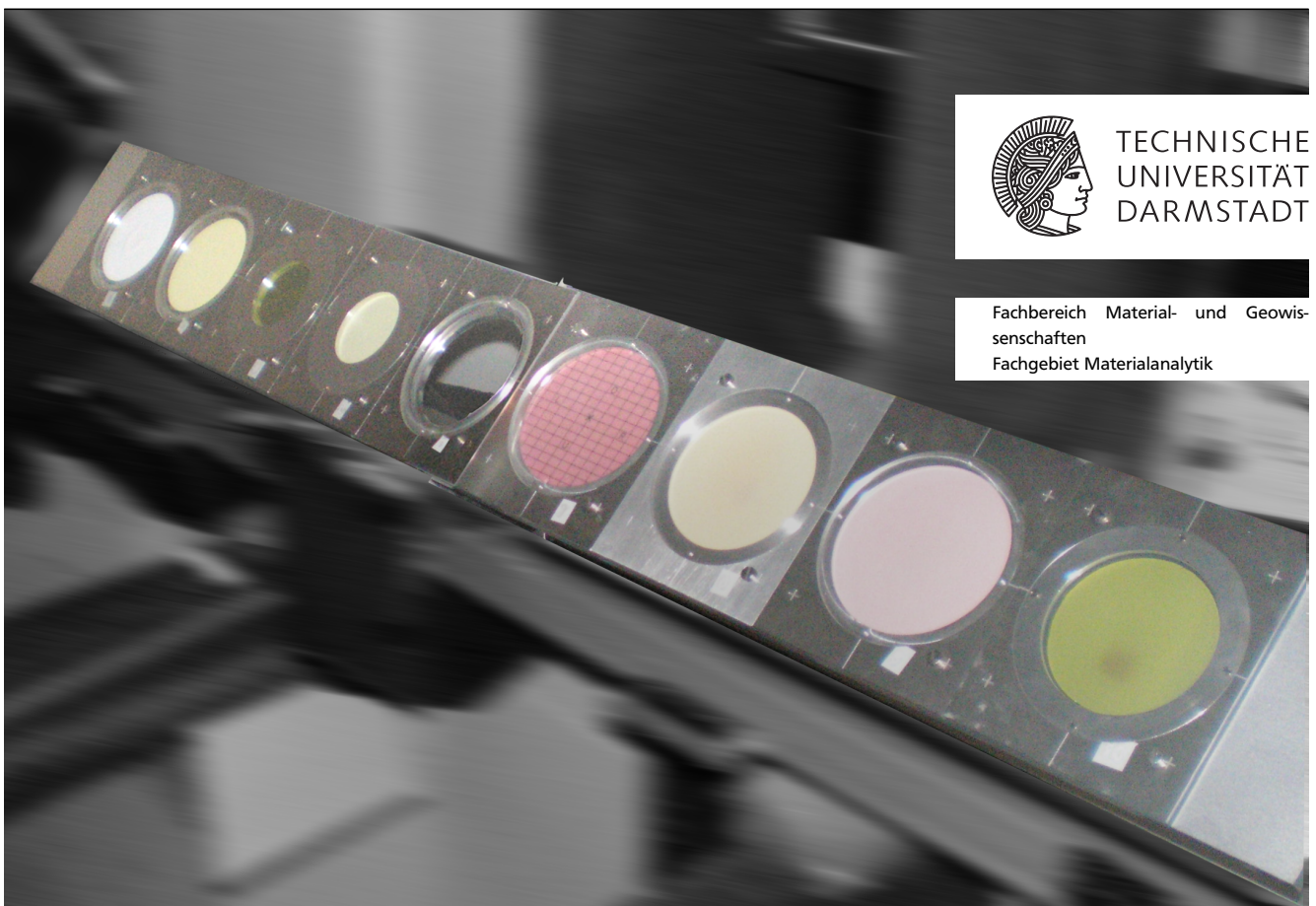
Investigations on Imaging Properties of Inorganic Scintillation Screens under Irradiation with High Energetic Heavy Ions

Untersuchung der Abbildungseigenschaften von anorganischen Leuchtschirmen unter Bestrahlung mit hochenergetischen Schwerionen

Genehmigte Dissertation von Dipl.-Phys. Alice Lieberwirth aus Frankfurt am Main

1. Gutachten: Prof. Dr. Wolfgang Ensinger
2. Gutachten: Prof. Dr. Oliver Kester

Tag der Einreichung: 1. April 2016
Tag der Prüfung: 5. Juli 2016

Darmstadt — D 17
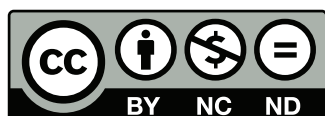
"Success consists of going from failure to failure without loss of enthusiasm."

Winston Churchill

Contents

Abstract

This work represents the investigations in imagine properties of inorganic scintillation screens as diagnostic elements in heavy ion accelerator facilities, that were performed at GSI Helmholtz Centre for Heavy Ion Research (Darmstadt, Germany) and TU Darmstadt. The screen materials can be classified in groups of phosphor screens (P43 and P46 phosphor), single crystals (cerium-doped $Y_3Al_5O_{12}$) and polycrystalline aluminum oxides (pure and Chromium-doped Al_2O_3). Out of these groups, a selection of seven screens were irradiated by five different projectiles (proton, nitrogen, nickel, xenon and uranium), that were extracted from SIS18 in fast (1 μs) and slow (300-400 ms) extraction mode at a specific energy of $E_{spec} = 300$ MeV/u. The number of irradiating particles per pulse was varied between 10^7 and $2 \cdot 10^{10}$ ppp and the scintillation response was recorded by a complex optical system. The records served on the one hand for investigations in the two-dimensional response to the irradiating beam, namely the light output L, the light yield Y and the characteristics of the beam profiles in horizontal and vertical direction. On the other hand the wavelength spectrum of the scintillation was recorded for investigations in variations of the material structure. A data analysis was performed based on a dedicated Python script. Additionally three conventional methods (UV/Vis transmission spectroscopy, X-Ray diffraction, Raman fluorescence spectroscopy) were performed after the beam times for investigations in the material structure. Nevertheless, neither structural variations nor material defects, induced by the ion irradiation, were proven within the accuracy range of the used instrumentation and the given ion fluences.

Besides the irradiation under varying beam intensity, radiation hardness tests with fast and slow extracted Nickel pulses at $2 \cdot 10^9$ ppp and a specific energy around $E_{spec} \approx 300$ MeV/u were performed and the scintillation record was used to examine the material stability under long time application. Here, the light yield Y of the targets was nearly constant or decreased only in the range of 10-15 %, relative to the initial value. For the targets with single crystal characteristic (P46, YAG:Ce), Y even increased slightly and than saturated, offering an enhanced mobility of charge carriers under irradiation. The emission spectra were reproduced continuously and the beam profiles showed good accordance to the reference methods.

Within all performed beam times, the targets offered a great stability. Non-linear characteristics, e.g. due to quenching during irradiation at high beam intensities, were not observed. The light yield Y showed a decreasing tendency as function of calculated electronic energy loss dE/dx. The characteristics of the calculated beam profiles, as well as the recorded emission spectra did not change significantly. So a material degradation in the investigated materials was not verified. This observation is confirmed by the performed material characterization measurements. The need of target replacement, e.g. due to damage, did not occur and was thus not performed during the complete investigations. As material for future beam diagnostics of FAIR cerium-doped $Y_3Al_5O_{12}$ single crystal with a thickness in the range of 300 μm is recommended in cross-points between different storage sections, due to the stable imaging properties for high energy ion beams, even under long-time irradiation. For beam alignment to experimental and research areas, common Al_2O_3:Cr is recommended due to the cost advantage.

Zusammenfassung

Für diese Arbeit wurden die Abbildungseigenschaften anorganischer Szintillatoren unter Bestrahlung mit hochenergetischen Schwerionen untersucht. Hierfür wurden Messungen am GSI Helmholtzzentrum für Schwerionenforschung GmbH (Darmstadt, Deutschland) und der TU Darmstadt mit insgesamt sieben Leuchtschirmen durchgeführt, die sich in drei Gruppen einteilen lassen: Phosphorschirme (P43 und P46), Einkristalle (Cerium-dotiertes $Y_3Al_5O_{12}$) und polykristallines Aluminium Oxid (reines und Chrom-dotiertes Al_2O_3). Sie wurden mit fünf Ionensorten (Wasserstoff, Stickstoff, Nickel, Xenon und Uran) bestrahlt, die einerseits schnell (1 μs) und andererseits langsam (300-400 ms) vom SIS18 mit einer spezifischen Energie von $E_{spec} = 300$ MeV/u extrahiert wurden. Die Zahl der Ionen pro Puls wurde im Bereich zwischen 10^7 und $2 \cdot 10^{10}$ ppp variiert und die induzierte Szintillation wurde während der Bestrahlung mit einem komplexen Kamerasystem aufgenommen. Aus den Daten wurde sowohl die zweidimensionale Leuchterscheinung bestimmt, charakterisiert durch Lichtmenge L, Lichtausbeute Y und Strahlprofile in horizontaler und vertikaler Ausrichtung. Weiterhin wurde das wellenlängenabhängige Emissionsspektrum aufgenommen, um Veränderungen in der Materialstruktur zu untersuchen. Im Anschluss an die Strahlzeiten fand die Datenanalyse mit einem hierfür entwickelten Python Skripts statt. Weiterhin wurden die Materialien mit konventionellen Methoden (UV/Vis Transmissions Spektroskopie, Röntgenbeugung, Raman Fluoreszenz Spektroskopie) untersucht. Im Rahmen der Messgenauigkeit konnten bei den gegebenen Fluenzen keine dauerhaften Materialschäden nachgewiesen werden.

Zur zusätzlichen Charakterisierung der Materialstabilität bei längerer Bestrahlung wurden mit allen Leuchtschirmen *Strahlenhärte Tests* mit schnell und langsam extrahierten Nickel Pulsen bei $2 \cdot 10^9$ ppp und etwa $E_{spec} \approx 300$ MeV/u durchgeführt. Die Lichtausbeute Y blieb hier entweder konstant oder sank in einem Bereich von nur etwa 10-15 % des ursprünglichen Werts. Die Leuchtschirme mit Einkristall-Charakteristik (P46, YAG:Ce) zeigten sogar einen leichten Anstieg von Y, durch eine verbesserte Mobilität der Ladungsträger im Material. Die Emissionsspektren wurden zuverlässig reproduziert und die Strahlprofile stimmten gut mit denen der Referenzmessungen überein.

Die untersuchten Leuchtschirme verhielten sich während der gesamten Bestrahlung sehr stabil und zeigten ein lineares Verhalten bei verschiedenen Strahlparametern. Ein Quenching während der Bestrahlung mit hohen Strahlintensitäten wurde nicht beobachtet. Die Lichtausbeute Y zeigte einen abnehmenden Trend als Funktion des elektronischen Energieverlusts dE/dx. Weder die berechneten Strahlprofile, noch die aufgenommenen Emissionsspektren zeigten signifikante Änderungen. Ein Ersetzen der Leuchtschirme, z.B. wegen Zerstörung, war während der gesamten Messungen nicht nötig. Für die Verwendung in zukünftigen Strahldiagnose Elementen in FAIR werden zwei Arten von Leuchtschirmen genannt: Cerium-dotierte $Y_3Al_5O_{12}$ Einkristalle mit einer Dicke von etwa 300 μm werden für die Strahldiagnose an Schnittstellen zwischen verschiedenen Speicherringen empfohlen, da diese selbst unter Langzeit-Bestrahlung mit hochenergetischen Ionenstrahlen kaum oder unveränderte Abbildungen produzieren. Für die Strahleinstellungen zu Experimentierplätzen werden die bisher bereits üblichen Al_2O_3:Cr Schirme wegen ihres Kostenvorteils empfohlen.

1 Introduction

In the late 1960s the first German facility for heavy ion acceleration was founded by a collaboration of local scientists and as a workplace for nuclear science. Since then researchers were able to prove the existence of six new elements ($^{262}_{107}$Bh, $^{265}_{108}$Hs, $^{266}_{109}$Mt, $^{269}_{110}$Ds, $^{272}_{111}$Rg, $^{277}_{112}$Cn) at the GSI Helmholtz Centre for Heavy Ion Research (short: GSI). This enhanced the fields of nuclear and plasma physics, as well as material science. Since the commissioning of the heavy ion synchrotron SIS18 and the storage ring ESR also atomic and fundamental parts of astro physics are investigated at GSI. Furthermore the support and development for radiation therapy with ions was performed by the facility [1]. Cooperations with national and international research institutes and other acceleration facilities were established with the years so that the panorama of provided acceleration and deceleration skills were improved continuously.
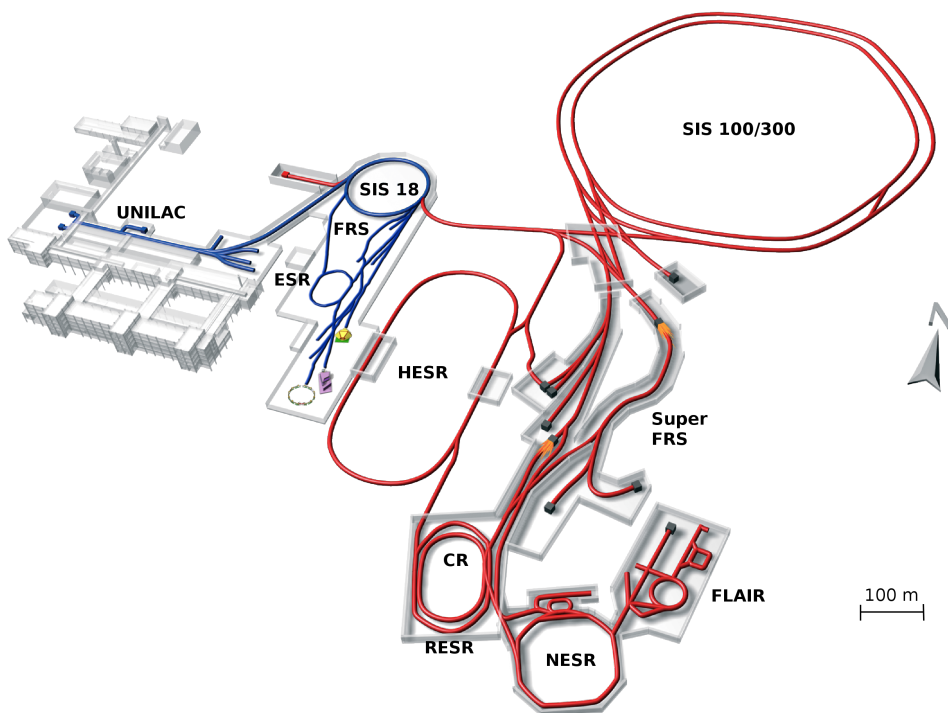
Figure 1.1: Existing GSI facility (blue) and construction plan for FAIR beamlines (red) [2], edited by A. Lieberwirth

However, the limits of the implemented technology are nearly exhausted, so that the FAIR cooperation was initiated in 2007. The goals of the international project are in principle to increase the range of present beam parameters, most notably the reachable energy and intensity, and to provide the generation and acceleration of antiprotons. In this way FAIR should serve for new research projects in quantum and astro physics and increase the parameters for research in atomic and plasma physics and in material research [2, 3]. A construction scheme of the FAIR accelerator system is shown in red in figure 1.1. The

blue lines[1] illustrate the existing accelerator of the GSI facility. These upgrade plans raise the question of appropriate diagnostic systems for the future beam parameters. A commonly used instrument to measure position and size of the accelerated ions is the scintillations screen, moved as an intercepting tool into the beam. Incident particles stimulate the target material to emit light within the optical region so that the visible projection should correspond to the transverse parameters of the accelerated beam.

Previous measurements at the linear accelerator UNILAC with different inorganic scintillation materials revealed a dependence of screen response in respect of beam projection (i.e. the projected horizontal and vertical beam width) and light yield and that the imaging properties are not only a question of material, but also of the irradiating parameters (charge/mass, irradiation duration) [4–6]. Meanwhile investigations with slow extracted beams from SIS18 at 300 MeV/u with similar scintillation screens showed an invariant behavior to the ion bombardment. They offered a linear response to different ion pulse intensities and a high stability during long time irradiation, even though the beam energy was orders higher than at UNILAC [7, 8]. These contradictory observations are part of the research in the *scintillator non-proportionality* subject, for which different models were published in the past. They are either based on the choice of ion as projectile [9–15], on the temporal distribution of the scintillation process [16, 17] or on the amount of deposited energy [18–21], and they give continually the occurring of non-radiative relaxation processes or *quenching* as origin for the observed scintillation loss.

For FAIR ions beams from protons up to uranium, accelerated with energies between 1 and 29 $\frac{\text{GeV}}{\text{u}}$ and with intensities up to $4 \cdot 10^{13}$ ppp, are planned [2,3]. These extreme beam parameters are rarely realized in the world and the response of a material under such irradiation is subject of recent investigations. Nevertheless, the choice of an appropriate material as scintillators for FAIR beam diagnostics must be determined. So for the present thesis, measurements were performed with different ion beams (proton, nitrogen, nickel, xenon, uranium), extracted with $E \approx 300 \frac{\text{MeV}}{\text{u}}$ energy in fast and slow extraction mode from GSI synchrotron SIS18. These beams irradiated a choice of inorganic scintillators at the beam diagnostics test setup (HTP). Taking into account the limited available beam time during the 2013 and 2014 campaign, we limited the number of materials under test to four different inorganic compositions, from which seven testing screens were installed in the beam line (Gd_2O_2S:Tb, $Y_3Al_5O_{12}$:Ce, undoped Al_2O_3 and Al_2O_3:Cr). The targets were irradiated under varying beam intensities to investigate the general response behavior. Also the material stability during use as diagnostic element was tested within a performed hardness test.

The principles of radiation in matter and the process of scintillation will be explained in chapter "2 Physics Background of Beam Interaction with Materials". Afterwards, four distinct models of scintillator non-proportionality will be described. Chapter "3 Application of Scintillation Screens in Accelerator Facilities" will describe the basics of heavy ion acceleration facilities and in detail the use of scintillators in beam diagnostics. Here the choice of materials that were used for investigations are introduced as well. The optical setup that was used to record the material response to the irradiation and the general experimental setup will be described in chapter "4 Ion Beam Experiments". Chapter "5 Data Analysis and Experimental Results" starts with an introduction to the performed calculation and record analysis. Afterwards the results of the beam time records will be presented. In the résumé a recommendation of scintillation material as diagnostic device for FAIR beam alignment is given. Since characteristic

---

[1] The blue lines as well as the detector symbols in the High Energy Beam Transfer area were added manually by A. Lieberwirth

observations during beam time promoted additional questions, two measurement campaigns outside the main project were performed and analyzed. They are presented in chapter "6 Accelerator Specific Investigations". Chapter "7 Characterizing ex-situ Measurements" explains three types of conventional material analysis methods to characterize the structure and eventually occurring damage of a material. The methods were performed after beam times with the investigated scintillation targets and the results are presented. The thesis ends in chapter "8 Conclusion and Outlook" with a summarizing conclusion and an outlook to possible future investigations.

2 Physics Background of Beam Interaction with Materials

2.1 Radiation in Matter

The research of material structure experienced a significant improvement, when Ernest Rutherford irradiated a gold foil with particles from a radioactive source [22]. The released α-particles were detected by the induced scintillation signal on an inorganic phosphor screen (ZnS), placed circularly around the gold target.

The α-particles had total energies in the range of $E \simeq 10$ MeV. Normalizing to the atomic mass, this energy accords to the velocity of the projectile and is then called specific energy[1] E_{spec}. For the classical Rutherford scattering experiment the specific energy is calculated with $E_{spec} \simeq 10$ MeV/u. The scattering is caused by the electromagnetic interaction of the projectile with the electron shell of the target. This principle, that is also responsible for the deceleration is called *electronic stopping power* and takes place for (positive) projectiles with $E_{spec} > 100$ keV/u. It was described closer in 1930s by H. Bethe and later revised by F. Bloch [23, 24]. Projectiles with energies in the upper limit or above the electronic stopping power are able to overcome the Coulomb barrier. Projectiles with these high energies will obey the strong interaction [25]. Nevertheless, the projectile energies for the present thesis were chosen within the range of electronic stopping, where the number of inelastic collisions can be neglected.

The mathematical formulation of the energy loss dE_{ion} per path length dx can be found in various notations, as e.g. in the following way given in [26]:

$$-\frac{dE_{ion}}{dx} = \frac{4\pi N_A z^2 e^4}{m_e V^2} \frac{Z}{A} \left[\ln\left(\frac{2mV^2}{\overline{I}(1-\beta^2)} \right) - \beta^2 \right] \tag{2.1}$$

Here z, m and V are charge, mass and velocity of the projectile, $\beta = \frac{v}{c}$ denotes its relativistic velocity. Z and A give the atomic and the mass number of the target. N_A is the well-known Avogadro-constant while $\overline{I}$ represents the mean ionization potential of the target atoms. The latter is usually in orders of $13.5 \cdot Z$ eV [26].

One conclusion from equation (2.1) is the maximum range of a specific projectile inside the target material. For ions a non-linear energy loss in matter was found, offering a maximum value, called *Bragg peak* [27]. The peak is a result of charge dynamics of the projectile: During passage through a material of specific density, the atomic shell of the ion loses electrons due to the Bohr's criterion. As a consequence the Coulomb force between projectile and the atom nuclei of the target increases. This means an increase of electrical attraction so that the projectile is decelerated over each partial path dx. An example of the

---

[1]　To calculate E_{spec} the total energy E has to be divided by the atomic mass of the projectile. E_{spec} is proportional to the relative velocity $\beta = \frac{v}{c}$.
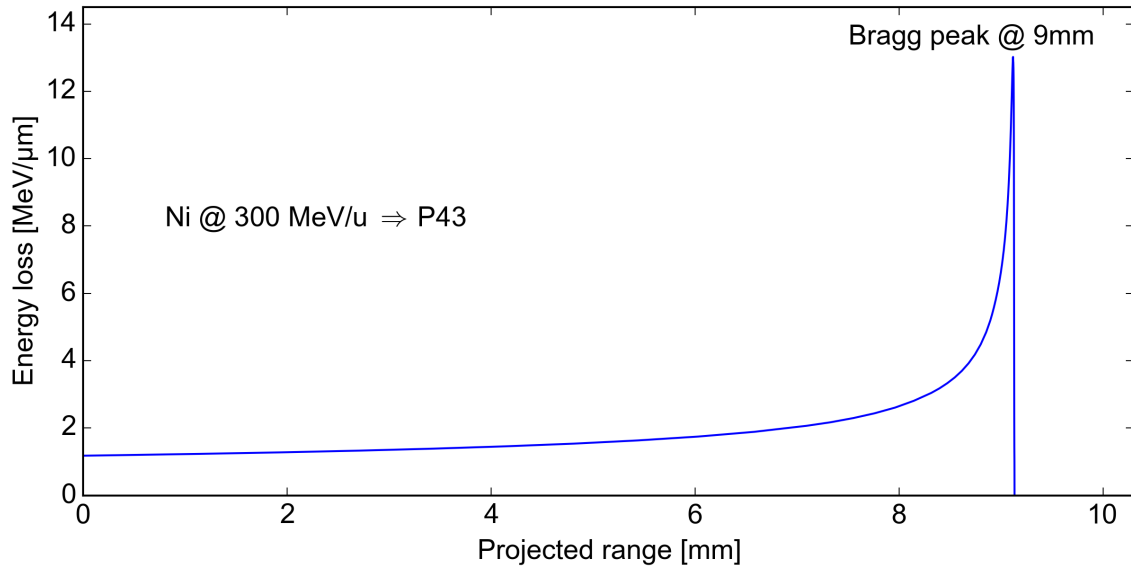
Figure 2.1: Bragg peak of Ni ion in P43, calculated with SRIM [27]
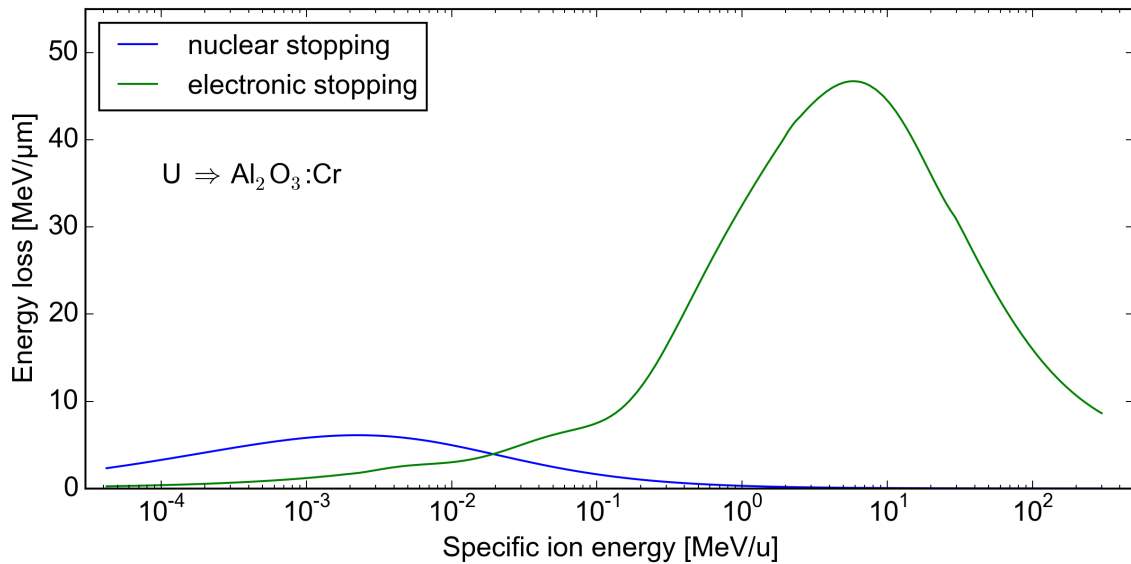
Figure 2.2: Example of nuclear vs electronic stopping power for Uranium ions in Chromium-doped Aluminum Oxide, calculated with SRIM [27]

Bragg distribution is shown in figure 2.1 for a Nickel ion with specific energy of $E_{spec} = 300$ MeV/u in a P43 target with density $\rho = 7.21 \frac{g}{cm^3}$.

Starting from the 1970s the knowledge about stopping power in material was enhanced, mainly by Ziegler et. al. [27, 28]. It was discovered that slower projectiles with $E_{spec} \leq 100 \frac{keV}{u}$ are decelerated mainly by the repulsing Coulomb force between the ion and the target nucleus. This deceleration effect is thus called *nuclear stopping power*. For comparison both types of energy losses are shown exemplary in figure 2.2. The curves were calculated with SRIM [27] for an Uranium ion in Chromium-doped Aluminum Oxide. Since the specific energies of the investigated projectiles in the scope of this thesis were far in the region of electronic stopping, the nuclear stopping will not be examined further here.

The deposited energy is partially converted into light by a large variety of recombination effects. This scintillation process is described in the next section.

2.2 Scintillation Process in Inorganic Materials

Scintillation is induced by energy deposition from ionizing radiation and describes the emission of light, mostly in the ultraviolet or visible part of the spectrum. First observations of the phenomenon were made by T. Sidot in 1866, during development of a ZnS crystal growing method by sublimation [29, 30]. Insulators represent suitable materials and are divided in inorganic and organic (or 'plastic') scintillators. Here only the scintillation process in the first type will be explained closer. Organic scintillators react significantly different. Details can be found in [31, 32] and similar literature.
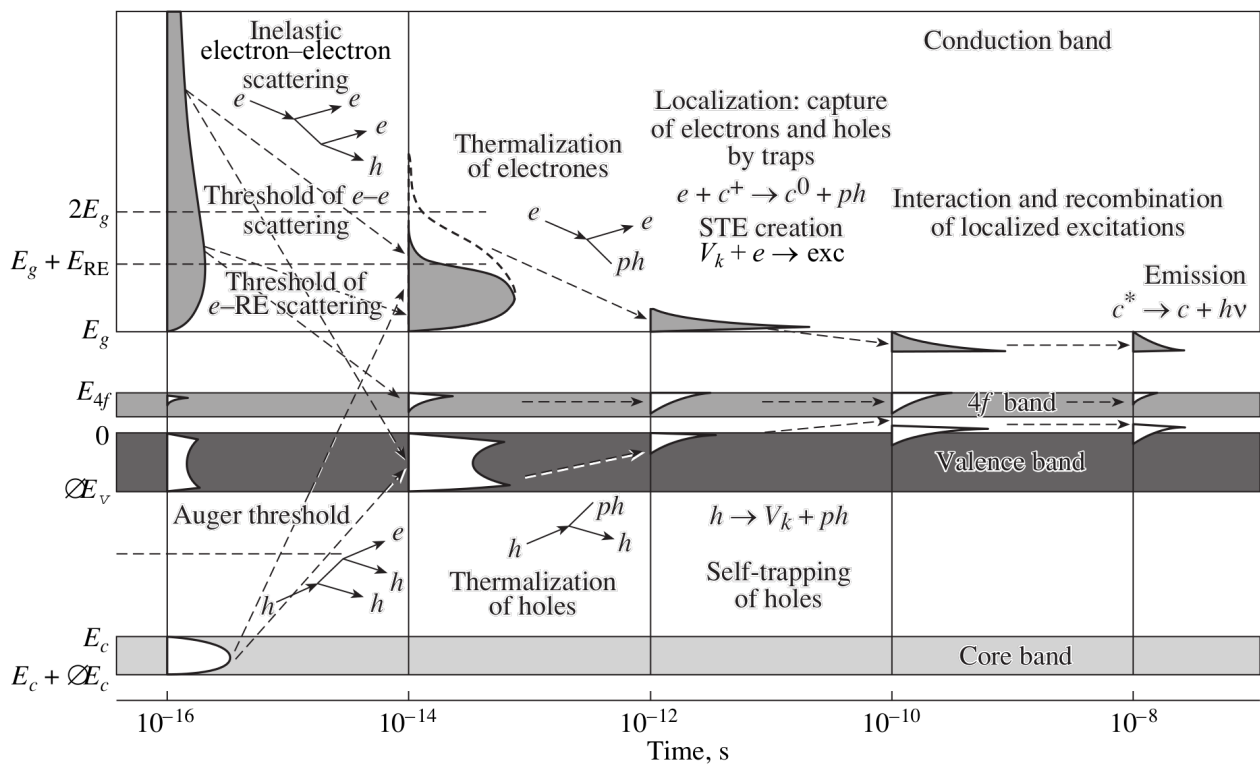
Figure 2.3: Scheme of scintillation process in inorganic scintillators with rare-earth doping, from [33]

The scintillation process is illustrated in figure 2.3. It shows the conversion of energy to photon emission in the electronic band structure. The general energy bands with energies E_c (core band), E_v (valence band) and E_g (energy gap, beginning of conduction band) form the vertical axis and the chronological development of the process is plotted on the horizontal axis. Doping with a rare-earth element (short: RE) causes an interband between the valence and the conduction band. It corresponds to the f-orbital of the RE and since the doping is mainly performed with elements of the lanthanide group, the band is called E_{4f}. In figure 2.3 scintillators with a RE doping are called *extrinsic* and are known for their high scintillation efficiency [33, 34]. Within the present project only extrinsic materials were used with the exception of one screen (Aluminum Oxide A999, see section "3.3 Classifications of Inorganic Scintillator Materials").

The five steps of scintillation process, visible in figure 2.3, will be described in the following and represent a summary of [26, 33, 35].

1. An energy is deposited by irradiation (photonic or corpuscular). After 10^{-18} s an intrinsic material is excited quasi instantaneous and electron-hole-pairs are created in the valence band around the reaction channel. The number of electron-hole pairs N_{eh} depends on the material-specific value for the energy E_{eh}. The electrons are lifted into the conduction band, while the holes do remain in the valence band (*energy conversion*). The created electrons (and holes respectively) scatter inelastically and multiply into further electron-hole-pairs, until the Auger threshold is reached. In extrinsic scintillators it is more probable that the charge carriers will have the energy E_{4f} of the interband, because the threshold is lower (see figure 2.3).

2. 10^{-16}-10^{-12} s after incidence *thermalization* takes place, which means that electrons lose energy by the production of phonons (*lattice vibration*) and therefore get closer to the band gap. The energy E_g of the band gap is a characteristic value for each material and is directly proportional to the energy E_{eh}, that is necessary for the production of electron-hole-pairs (see step 1) [26].

$$E_{eh} = const_{material} \cdot E_g \qquad (2.2)$$

In extrinsic materials the electrons are scattered additionally at the rare-earth dopants, so that the thermalization is continued, until the energy of the electrons becomes smaller than $E_g + E_{RE}$. The holes on the other hand gain energy by interacting with the phonons and so approach the band gap on their way.

3. Due to the thermalization, the energies of the electrons and the holes approach the gap energy E_g. This makes a permutation within the crystal structure possible, so that defects can occur. This step is called *localization* and happens 10^{-12}-10^{-10} s after energy deposition.

4. When the electrons and holes in an intrinsic scintillator are only separated by the gap energy E_g, they are able to form excited pairs, also called *excitons*. This step takes 10^{-12}-10^{-8} s. Alternatively material defects can be created, which trap the charge carriers before their energy exceeds E_g. Defect formations are described in more detail in the dedicated section "2.5 Defect Formations".
   In extrinsic scintillators, the $4f$ band reduces the necessary energy to overcome the insulator gap. Hence, the electrons can perform forbidden transitions additionally, e.g. $4f \rightarrow 4f$ or $5d \rightarrow 4f$ transitions. This leads usually to a delay in the recombination step (*phosphorescence*). The delay time can vary between nanoseconds for 5d-4f transition (e.g. in Ce^{3+}-doped materials) and minutes for parity-forbidden 4f-4f transition (e.g. in Tb^{3+}-doped materials) [26, 33, 34]. Steps 3 and 4 characterize the efficiency T of a material to transfer electrons and holes to luminescence centers and the losses Q due to non-radiative transitions in the material, which again defines the number of photons $N_{photons}$, that are created per number of electron-hole pairs N_{eh} [26]:

$$\frac{N_{photons}}{N_{eh}} = T \cdot Q \qquad (2.3)$$

5. Minimum 10^{-10} s after irradiation the previously formed excitons start to recombine and low-energy photons are emitted. This step is called *luminescence* and is ideally emitting with a wavelength distribution in the visible range. Measuring the luminescence, i.e. the number of photons $N_{photons}$, within a specific range of solid angle Ω, is called *light output L*:

$$L = \int_{\Omega_{start}}^{\Omega_{end}} N_{photon} \, d\Omega \tag{2.4}$$

More details concerning the calculation of L in this thesis will be given in the summary about data analysis in section "5.2 Offline Analysis of Scintillation Response".

From equation (2.3) the efficiency of a scintillator, to transform a deposited energy into light, is derived with [26]:

$$S = \frac{TQ}{c_{material} \cdot E_g} \tag{2.5}$$

Equation (2.5) reduces the defining parameters for the observed scintillation to values, that are characterized only by the chosen material. Thus S serves as general quantity, to compare different scintillator materials under equal irradiation conditions. In the present case the yield Y induced by ion irradiation will be calculated equivalent to equations (2.5) and (2.4):

$$Y = \frac{L}{\Delta E_{per\,ion}} \tag{2.6}$$

where $\Delta E_{per\,ion}$ is the deposited energy per single ion.

The maximum value of S can be approximated by [26]:

$$S_{max} \approx \frac{0.5 \cdot 10^6}{E_g} \left[\frac{\text{photons}}{\text{MeV}} \right] \tag{2.7}$$

Equation (2.7) provides the possibility to estimate the gap energy of different materials by measuring the light yield.

2.3 Franck-Condon Principle

The Franck-Condon principle represents an approach of the quantum mechanical transitions in a material [36, 37] and gives an alternative model of scintillation to the previously described. Atoms (and molecules similarly) are described as harmonic oscillators and their energetic states are described by wave functions around the configuration coordinate Q. At $Q = 0$ the ground state of an atom has its maximum probability, so that the wave function has its defined minimum here. The Franck-Condon principle describes the lattice vibrations as result from the interaction between electrons and atom lattice. The vibrations are defined simultaneously with the terms *vibron* and the different vibronic states n,

in which the system can be located, and they are defined by the local geometry of the harmonic oscillator. The processes, based on the the Franck-Condon principle, are shown exemplarily in figure 2.4 for a ground state i to an excited state f and will be described in the following.
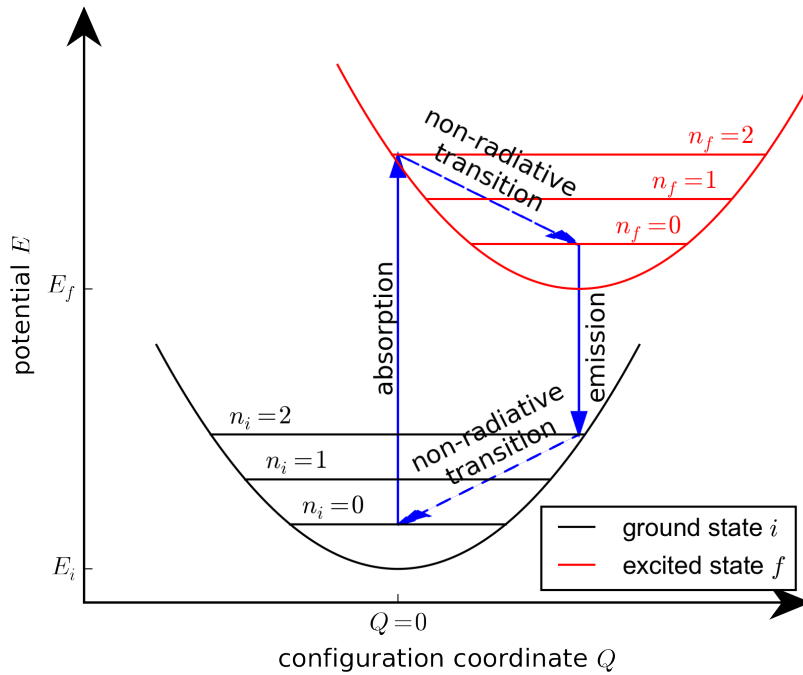
Figure 2.4: Excitation and relaxation by Franck-Condon principle, based on [36]

If an energy is absorbed by an atom, it is excited from the ground state to a level in the excited state. During this transition, a movement of atoms is suppressed, due to the high mass of the nuclei (*semiclassical consideration*). Thus, the absorption happens nearly perpendicular in the configuration diagram and the excited atom ends up in general in a higher vibronic state, as illustrated in figure 2.4.

The semiclassical consideration is valid for the relaxation back into the ground state (i.e. the emission), as well. Nevertheless, the emission starts in general from the lowest excited state ($n_f = 0$). This means in turn, that an atom that was excited recently has to reduce its vibronic level first. Such transition processes are usually non-radiative, which means that no photons are emitted, and they are performed mainly by two process: either by recombination in or close to the interband or the redundant energy is transferred to an electron, which is then returning stepwise into the minimum state without radiation (*Auger process*). Each non-radiative transition can be considered as loss of luminescence and besides the here described processes, other kinds of quenching can occur, as explained in the next section.

2.4 Non-proportionality and Quenching

Apart from the general scintillation as result of the previously described process, non-proportionality of luminescence has been observed and investigated in a wide range of parameters, regarding projectile type and energy and the choice of target material [9–15, 18–21]. Different models have been developed in order to explain the loss of luminescence to non-radiative relaxation mechanisms in the materials. This issue is called *quenching*. Some models are described in more detail in the following sections.

2.4.1 Radial Dose Distribution of δ-electrons

Around the path of one incident ion (also: *ion track*) the deposited energy causes the release of high-energetic electrons. These electrons were called δ-*electrons* by Meyer and Murray, who found first evidence for them in 1962 [38]. Inside the material the δ-electrons transfer the energy radially with respect to the ion track in a radius r. The deposited amount of energy per mass element is called dose $D(r)$ (unit: $1\,\mathrm{Gy} = \frac{\mathrm{J}}{\mathrm{kg}}$) and was described amongst others by Katz et al. [39]. With Z^{*2} and $\beta = \frac{v}{c}$ as the effective charge and velocity of the projectile, respectively and N as the number of dissociated electrons, $D(r)$ is written as [39]:

$$D(r) = \left(\frac{Z^{*2}Ne^4}{\beta^2 m_e c^2}\right) \cdot \underbrace{\left(\frac{1}{\frac{1}{r}+0.6+1.7\beta}\right)}_{a)} \cdot \underbrace{\frac{1}{r^2}}_{b)} \cdot \underbrace{\exp\left(-\left(\frac{r}{0.37 r_{\max}}\right)^2\right)}_{c)} \tag{2.8}$$

Here, e, c and m_e are the natural constants for elementary charge, speed of light and mass of an electron. r_{max} marks the maximum radius, in which δ-electrons are created by the deposited energy W_{max} (in eV). This energy was described for the general case by the Particle Data Group [40], but can be approximated to a quadratic function of velocity $c \cdot \beta$ and the relativistic Lorentz factor $\gamma = \frac{1}{\sqrt{1-\beta^2}}$ of the projectile with [4]:

$$W_{max} = 2m_e(c \cdot \beta)^2 \cdot \gamma^2 \tag{2.9}$$

High relativistic projectiles deposit more energy W_{max} into the material, which leads to higher maximal radii r_{max}. This fact is represented in equation (2.8) with term $c)$, which determines as well the point where $D(r)$ drops. For medium radii r decreases with term $b)$ and so in principle quadratic. For small radii $r \gtrsim 0$ close to the ion track term $a)$ causes a linear decrease of $D(r)$, especially for non-relativistic projectiles.

An example for the radial dose distribution is given in figure 2.5. It shows the radial dose distribution $D(r)$ calculated for water, irradiated with a Ne ion. The black line is here taken from reference [39] and a maximum radius of $r_{max} = 4.0$ mm was calculated for it. For comparison the green, red and blue lines were included in the figure and their ion energies were here chosen in a way, that the maximum radii of the resulting δ-electron-cascade correspond to $r_{max} = 0.04$ mm, $r_{max} = 0.8$ mm and $r_{max} = 20.0$ mm, respectively. As can be seen, the amplitude of $D(r)$ is decreasing with increasing ion energy.

As a reference, the dashed magenta line was plotted additionally in figure 2.5. It illustrates the radial dose distribution for a Helium ion at 377 MeV/u in water. The calculated maximum radius $r_{max} = 4.0$ mm results only from the velocity of the projectile and is thus the same as for Neon ions in water. The amplitude of $D(r)$ is smaller than for the black line. This illustrates the dependence of the model from the projectile's charge Z.
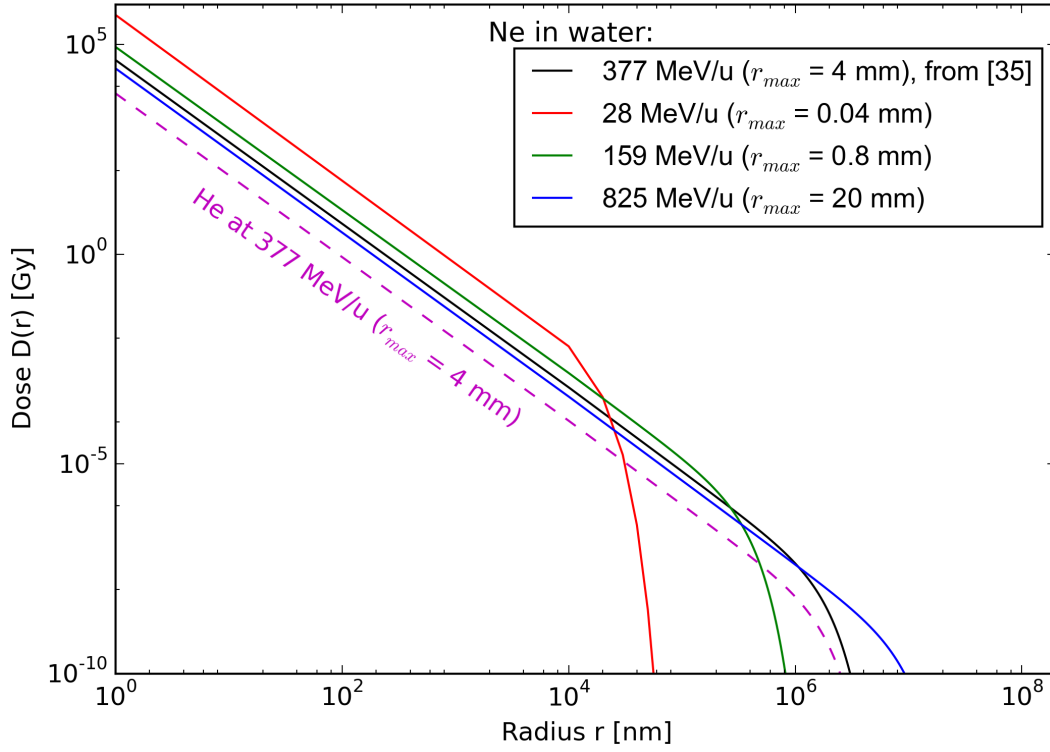
Figure 2.5: Radial dose distribution of a Ne ion in water. The black line was calculated in reference [39], while the red, the green and blue line were calculated for comparison with the conditions given in the legend.

2.4.2 Quenching due to Maximal Energy Density

A similar model like presented in 2.4.1 was developed by the group around Michaelian and Menchaca-Rocha. They developed a mathematical model to explain the non-linearity of luminescence efficiency of an inorganic scintillator on basis of limits in energy deposition by secondary electron (EDSE) as similar notation for δ-electrons [9–11]. The assumption is, that the quenching radius r_q around the incident ion track is not defined by the (mass-dependent) dose, but by a critical density of energy deposition ρ_q per volume. In contrary to the Katz model, [10] gives a formula to calculate the maximum radius R_{max} the δ electrons can reach in transversal direction to the ion path. For a dissipated energy of maximum W_{max} (see equation (2.9)), R_{max} in cm is given by:

$$R_{max} \approx a W_{max}^{\frac{5}{3}} \tag{2.10}$$

The coefficient a comes from the mass-range, described in [41]. With density ρ_{target} (in $\frac{g}{cm^3}$), averaged mass and charge numbers $\langle A_{target} \rangle$ and $\langle Z_{target} \rangle$ of the target a is approximated with:

$$a = \frac{5.025 \cdot 10^{12} \langle A_{target} \rangle}{0.182 \rho_{target} \langle Z_{target} \rangle^{\frac{8}{9}}} \tag{2.11}$$
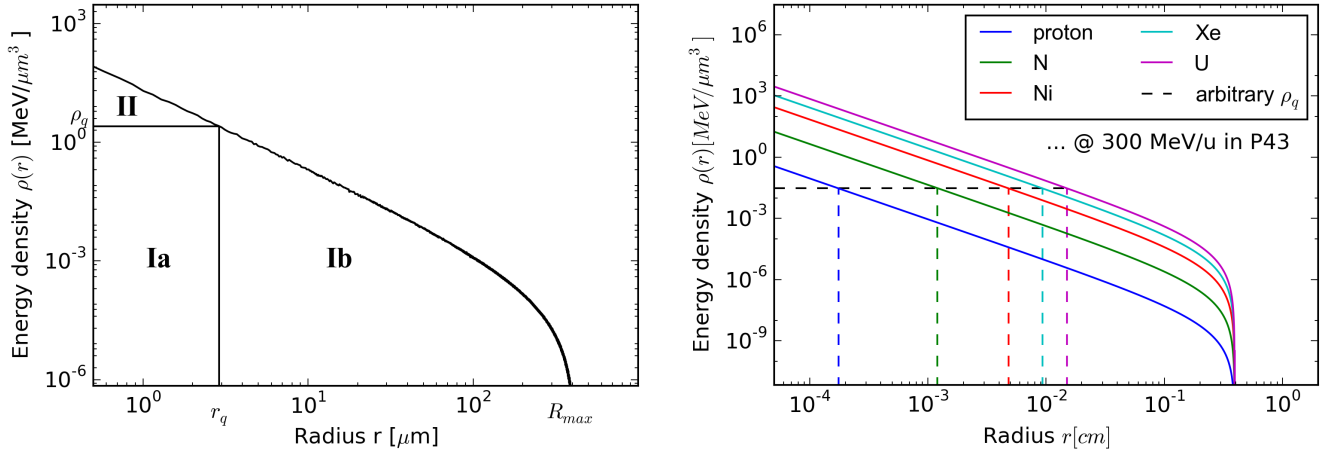
(a) Regions of deposited energy density, calculated for 800 MeV Ne^{20} ions in CsI target, from [10]

(b) Calculated energy density, deposited by different ions at 300 MeV/u in P43 target, the horizontal line marks an arbitrary chosen quenching density ρ_q, to illustrate the different quenching radii $r_{q,ion}$

Figure 2.6: Distribution of energy density as function of radius r around the ion track

The model basically calculates the maximum of δ-electrons as a function of target material properties. Neither mass nor charge of the projectile is taken into account in equations (2.10) and (2.11). The only influence the projectile has on R_{max}, is a change of velocity β and Lorentz factor γ.

Assuming the energy loss of the projectile in a target material D as given, the effective charge of the projectile is squared (compare with equation (2.1)). So D is given in [10] as:

$$D = N_A \rho_{target} \frac{\langle Z_{target} \rangle}{\langle A_{target} \rangle} \frac{e^4}{m_e c^2} \frac{Z_{eff}^2}{\beta^2} \tag{2.12}$$

Then the density of energy deposition $\rho_E(r)$ as function of transversal radius r is calculated with

$$\rho_E(r) = \frac{3D}{5r^2} \left(1 - \frac{r}{R_{max}}\right)^{0.0054 \cdot \langle Z_{target} \rangle + \frac{3}{5}} \tag{2.13}$$

An example for $\rho_E(r)$ was calculated in [10] for Ne ions of approximately 40 MeV/u in a CsI target and is shown on the left hand side of figure 2.6. Here the horizontal line indicates the quenching density ρ_q, which marks for this part the quenching radius r_q (illustrated as vertical line).

The area below the quenching density ($\rho \leq \rho_q$) is separated in **Ia** and **Ib** and marks the region of linear scintillation response. Here, **Ia** corresponds to the region of constant detector response. The scintillation stops, when $r = R_{max}$ is reached. If the deposited or transfered energy per volume exceeds the quenching density ($\rho > \rho_q$), the material fails to convert the abundance of energy into scintillation and the resulting quenching reduces the light emission. This "region of inefficiency" is marked with **II** in figure 2.6a.

The right side of figure 2.6 shows the calculated energy deposition densities $\rho(r)$ for different projectiles at constant specific energy $E_{spec} = 300$ MeV/u. Here, the quenching density ρ_q was chosen
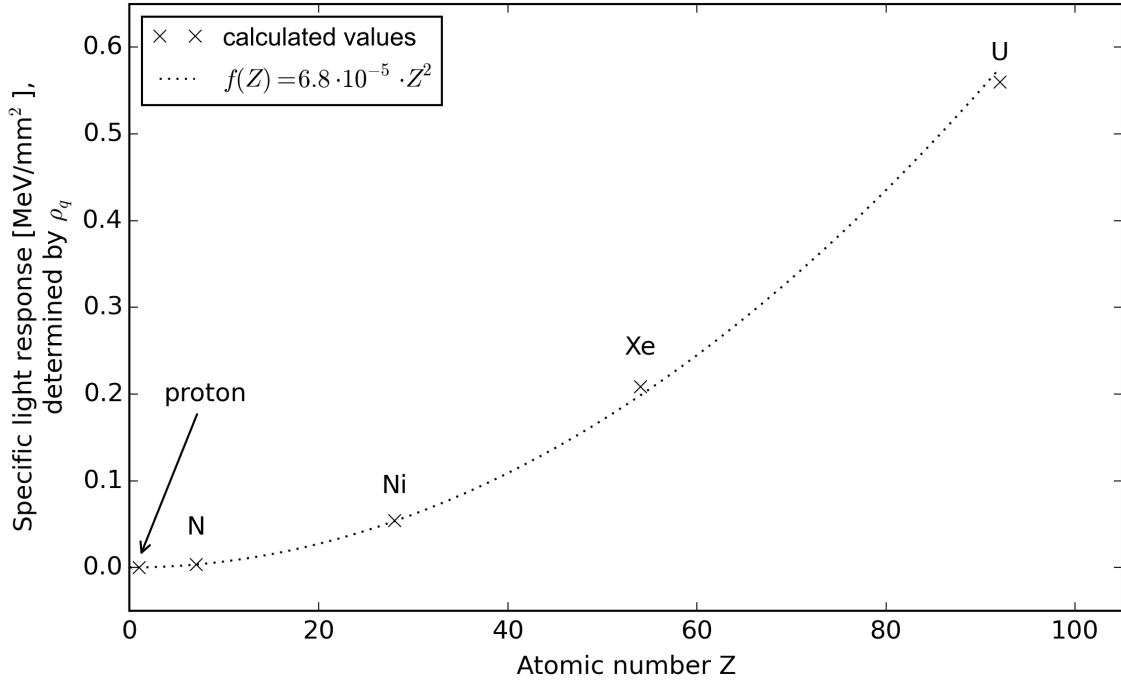
Figure 2.7: Specific light response for different ions, calculated from arbitrary quenching density ρ_q in figure 2.6b. The dotted line shows a manually defined quadratic function and was added to guide the eye.

arbitrarily to illustrate the development of quenching radius. As shown in the figure and already mentioned in [10], r_q has a dependence on the atomic number Z of the projectile, so that r_q increases for increasing Z. The region of constant detector response (**Ia**) is increased with Z as well and so does the light output of the material. Nevertheless, the increase of light response is not increased linearly. An example for specific light response was calculated for the arbitrary chosen quenching densities $\rho_{q,i}$ in figure 2.6b and is plotted in figure 2.7. For the chosen projectiles proton, N, Ni, Xe and U the light response increases quadratically, as indicated by the dotted line. The latter was added exemplary.

Altogether the characteristic of the distributions, presented in figure 2.6 shows a significant similarity to the $D(r)$ in figure 2.5.

2.4.3 Temporal Quenching

Papadopoulos investigated a different limitation of scintillation: He made a fundamental approach by using the energy loss per unit path length (equivalent to equation (2.1)) [16, 17]. With help of the differential approach of the temporal distribution of the luminosity $\frac{dL}{dt} = \frac{dL}{dx} \cdot \frac{dx}{dt}$ he approximated the rise time of a scintillator in dependence of the deposited energy. The scintillation process is here divided into two steps:

I) The first step describes the excitation of the scintillator atoms along the ion track analog to the description of Pédrini [33]. The relaxation of the system can be achieved by photon emission or any non-radiative quenching process.

II) The other possibility is the interaction between two excited atoms or an ion with an excited atom. In this case the target material has to recombine with a foreign electron first, before it can start the relaxation into the ground state, similar to step I).
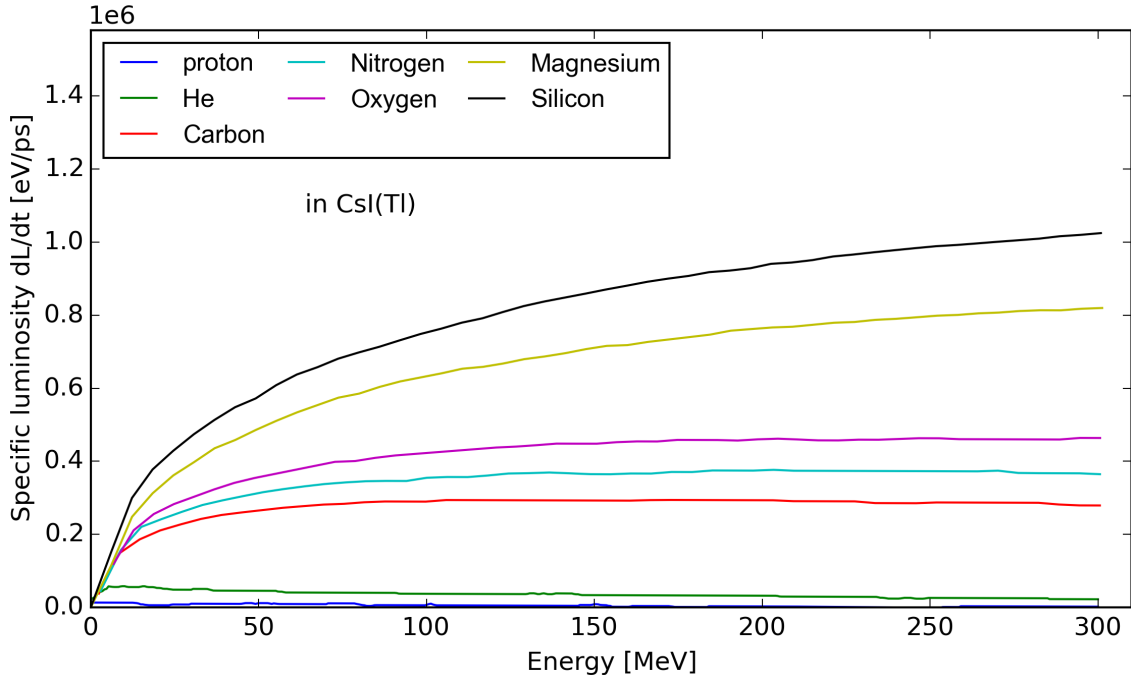
Figure 2.8: Specific luminosity $\frac{dL}{dt}$ of Tl-doped CsI as function of particle energy for different incident ions, adapted from [17]
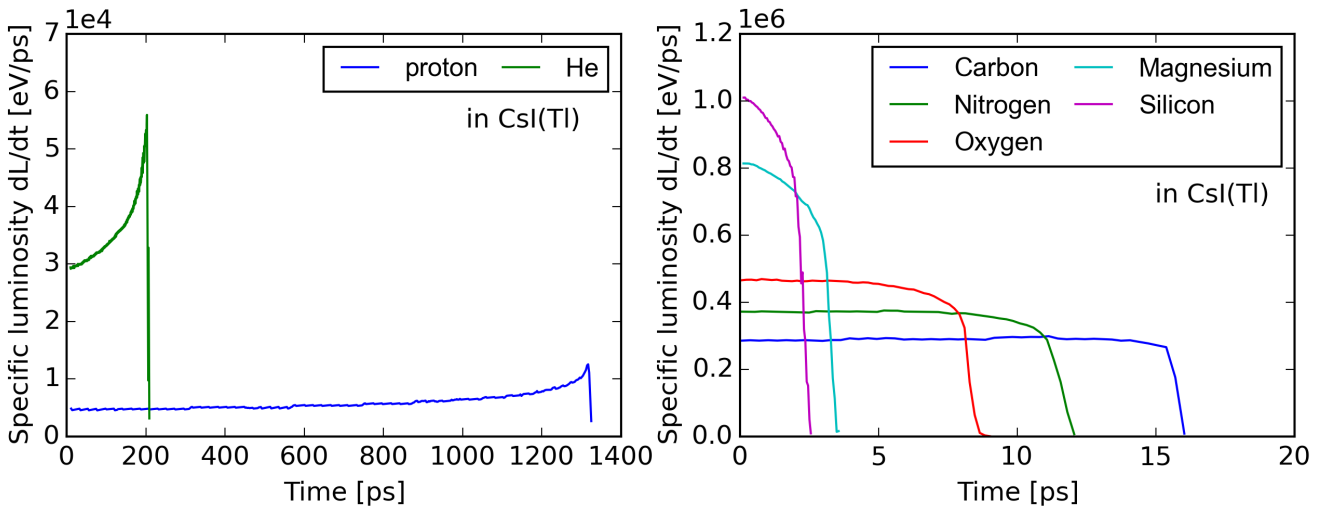
Figure 2.9: Specific luminosity $\frac{dL}{dt}$ of Tl-doped CsI as function of particle time, for different light (left) and heavy incident ions (right), adapted from [17]

Regarding the specific luminosity $\frac{dL}{dt}$ as a function of particle energy E, the two described processes in principle take place consecutively. Up to a specific energy E_{lummax}, where $\frac{dL}{dt}$ has its maximum, ionization is the dominant process, while excitation is dominating the luminosity for $E > E_{lummax}$. Figure 2.8 shows

$\frac{dL}{dt}$ as function of particle energy E for Tl-doped CsI target [17]. As can be seen, E_{lummax} is not a fixed value of the target material, but depends as well on the type of incident ion.

On the other side, the specific luminosity of a material is not a constant in time, as shown in figure 2.9 [17] for Tl-doped CsI. The scintillation stops at a determined time after irradiation, which depends on the choice of the irradiating ion. For protons and He, Papadopoulos shows, that more light output is observed during excitation at the end of scintillation process and that light output induced by ionization is rather suppressed for these light ions. This distribution is shown on the left hand of figure 2.9. On the right hand of the figure, the specific luminosity as function of time is shown for various heavy ions from C to Si. The heavier the incident ion is, the faster the scintillation is taking place.

As explained later in chapter "4 Ion Beam Experiments" the duration of a irradiating ion pulse is minimum 1 μs long. This is in fact of orders higher than the temporal distribution, that Papadopoulos describes. Nevertheless, one of the investigated ion pulses includes at least 10^6 particles, so that in an idealized pulse distribution the time between two impacts is maximum 10^{-12} s = 1 ps, which accords to the presented model in [17].

2.4.4 Model for Many-Particle Irradiation

The previously introduced models about quenching were all based on the irradiation of the scintillation target by only one single particle. This is the most unrealistic case in beam diagnostics in heavy ion accelerators. At GSI fast extracted beam pulses usually contain at least 10^5 particles per pulse at a duration[2] of e.g. 1 μs. This leads to the need of a quenching model for many-particle irradiation. An attempt was made by E. Gütlich and can be found in his PhD thesis [4]. It is based on the limitation of incident dose in a material D_{max} (see section 2.4.1) and offers the following statements:

- From equation (2.10) we learned, that the maximal radius R_{max} of a δ-electron cascade around the ion track is increased the faster a bunch of particles is. At the same time, the probability of the δ-electron cascade of two (or more) simultaneous incoming ions to overlap is increased as well with increasing particle velocity.

- The particle bunch irradiated the target in a measurable area. This creates the dose per area as parameter (analog to the model of Katz and Michaelian, described in section 2.4.1). If the ion beam is focused to smaller areas, the dose per area is increased, so that the probability for overlapping of the ion tracks is increased as well.

- The scintillation process, described in section 2.2, takes place in time windows of finite-measurable duration. Each (secondary) particle, that irradiates a material shortly after the first incident particle, finds an already excited state. The second particles can thus not induce further creation of electron-hole pairs (suppression of the first step in figure 2.3) and the scintillation process can not

---

[2]   More about pulse durations and their dependence on the extraction mode will be described in section "3.1 Heavy Ion Acceleration"

be started here. The fraction of the dose rate, that can not be converted, is inverse proportional to the maximal dose D_{max}:

$$D_{suppress} = \frac{D_1}{D_{max}} \sum_n D_n \qquad (2.14)$$

Here D_1 means the dose, the first irradiated particle deposits in the material, and D_n are the doses that correspond to the secondary particles.

A different approach to explain the decrease or loss of scintillation efficiency is the formation of defects in the materials. Some typically occurring defects are described in the next section 2.5.

2.5 Defect Formations

A crystalline material structure may be regarded as a defined lattice, for simplicity. The lattice is formed by positive ions as cations and negative ions as anions. Possible symmetries are described in various ways in literature and the corresponding symmetries for the investigated materials in the present project will be mentioned in section 3.3.
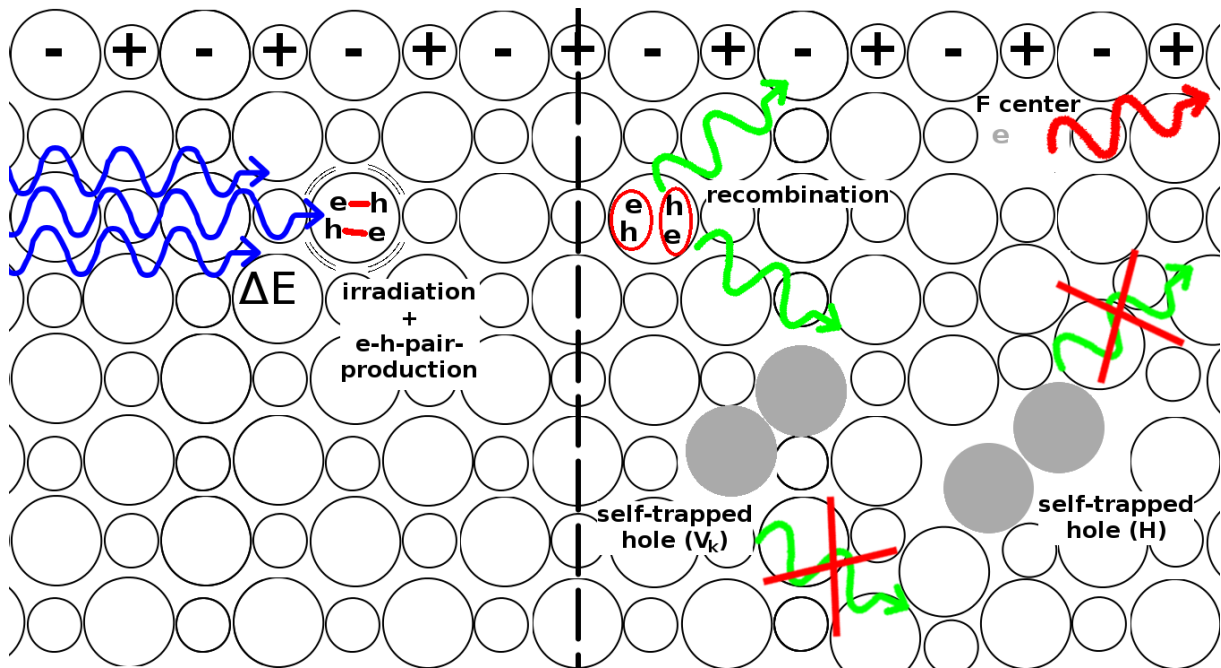
Figure 2.10: Scheme of the scintillation process as result of electron-hole-pair production in a primitive crystal system, according to descriptions in literature [26, 33, 35]

In this section the material should be figured as a primitive square-packed lattice, as shown in figure 2.10. In the figure the big circles, labeled with a minus sign, stand for the anions and the small circles labeled with a plus sign represent the cations of the crystal. The first three steps of the scintillation process, described in section 2.2 is summarized on the left side of the figure, the blue waves correspond to an energy ΔE that is introduced into the material. On the right hand side, the recombination process and the resulting emission of photons (green waves) is illustrated. Furthermore, possible

material defects are shown. Defects can trap the charge carriers and prevent them from recombination. They will be described in the following:

The most simple occurring defect is the elastic collision with lattice participant. The resulting vacancies can be filled by a different atom or an ion of similar charge and are named *antisites* or, if undesired, *impurities*. Antisites induce usually only slight changes in the lattice periodicity. For this reason these traps, that capture the charge carriers, are called *shallow traps* [26].

If specifically an electron is occupying an anion vacancy on a lattice place, the defect is called *F center*[3] or *color center*. The captured electron is prevented from recombination and so from photon emission. Also, the potential well, that a F center represents, can inflect the energy of a transmitted photon and thus change its color (shown in figure 2.10 as red wave). Hence, color centers are usually recognized by a spot of different or dark color on the material surface or by a change of scintillation emission [26].

Especially in alkali halides, where the radii of the lattice participants usually differ significantly, an anion vacancy represents a potential well. If an excited anion is moved to an interstitial position, the defect is called *Frenkel defect* and can lead to the creation of a *H* center: Here the interstitial anion shares an electron with one of the neighbored anions and thus forms an X_2^- conglomeration. In a *H* center the binding electron sits on a lattice place. This kind of center belongs to the category of self-trapped holes [26].

Another case of self-trapped holes is the V_k *center*. Here an anion is trapped by a free hole and becomes apparently positive. In contrary to the previously described *H* center, an electron is placed here on an interstitial place. An agglomeration between two neighbored anions starts and forms a X_2^-. The time to create a V_k center is in order of 1-10 ps, which is shorter than the time for recombination of a free hole with a free electron. For this reason the formation of a V_k center during irradiation is in principle much more probable than the recombination process [26].

If an anion at a lattice place is substituted, charge neutrality can be achieved as well by the replacement of cations with equal charge. This special case is called *Schottky defect*. Alternatively, e.g. in metals, Schottky defects are created by removing a metal atom at the outer edge of a grid. In an ideal case the lattice surrounding the vacancy stays unchanged in periodicity.

---

[3] "F" is from german: *Farbzentrum*

3 Application of Scintillation Screens in Accelerator Facilities

The present thesis focuses on the utilization of inorganic scintillation screens as beam instrumentation tool in accelerator facilities. A selection of four different materials was investigated with respect to their emission properties during irradiation with heavy ions from SIS18. They can be classified into three groups, namely *P43 phosphor*, *Ce-doped $Y_3Al_5O_{12}$* and *Aluminum Oxide ceramics*. Their structural and mechanical properties will be described in section 3.3. Before this an introduction to the principles of heavy ion acceleration and the necessary characteristics of scintillation screens for beam alignment will be given.

3.1 Heavy Ion Acceleration

In the scattering experiment of Rutherford [22], the energy of released α-particles was given by the radioactive decay. This condition motivated the question for improved or alternative acceleration techniques, to perform e.g. material science by atomic research with more than a few MeV particle energy.

The first design of a new accelerator technique was initiated by G. Ising in 1924 [42], using an alternating electrical field[1]. The principle is based on separated sections, applied with alternating radio frequency (short: RF field). The sections are called *drift tubes* and form a LINear ACcelerator or *LINAC*. Two adjacent drift tubes have fields with contrary polarity, so that the particles are accelerated by the space between the drift tubes. This space d between the drifts grows with increasing particle velocity β for a RF wavelength λ with [45]

$$d = \frac{1}{2}\beta\lambda \tag{3.1}$$

The LINAC concept was realized first of all by Wideröe in 1928 [46]. With this, Wideröe succeeded to accelerate potassium ions to 50 keV with an applied alternating voltage of 25 kV and so showed at the same time, that the reachable ion energies of the system can exceed the highest voltage of the setup. However, a Wideröe structure is strongly limited by the necessary distance d: For high particle velocities β eq. (3.1) increases to unreachable values and can thus be used only for ion acceleration to low velocities [45]. A solution to this limitation was presented by Alvarez [47] and applied in an accelerator facility in Berkeley, USA in 1946 [45, 47, 48]. In this structure the polarities between two adjacent drift tubes are the same, while the inside of the tubes is field-free. The velocity, that is necessary to inject particles into an Alvarez structure, starts at 4 % of the speed of light, which is why usually *low-*

---

[1]   First appreciable improvements of dc techniques were made a long time after Rutherford due to research during First World War. New dc accelerator techniques were developed afterwards by Cockcroft and Walton in 1930 [43] and by Van de Graaff in 1931 [44]. Nevertheless, the description of the structures would exceed the content of the thesis.

beta structures such as the Ising-Wideröe accelerator, is mounted in front. On the other hand, particle velocities up to 60 % of the speed of light can be reached [45].

Nowadays, the first stage of linear acceleration is usually a so called *Radio Frequency Quadrupole* (short: RFQ) as proposed by Kapchinskiy and Teplyakov in 1970 [49]. The structure is usually made of 2×2 electrodes, with a sinusoidal shape in beam direction z. The variation of the shape causes an alternating acceleration and focusing of the particles in longitudinal direction, so that an injected beam is separated into particle packages, called *bunches* [45,50]. A typical arrangement of a RFQ is shown in figure 3.1.
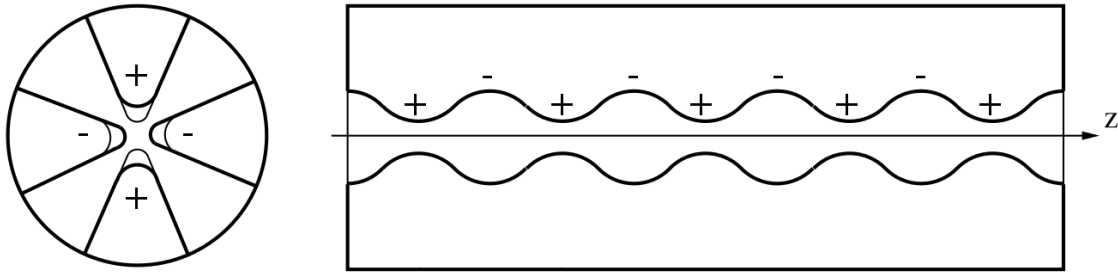
Figure 3.1: Scheme of a RFQ design [45]. The lateral cut on the left side shows the four electrode system, while the right side shows the sinusoidal modulation in beam direction z.

In absence of (another) longitudinal force or under weak alignment of the bunch phase the particles will tend to disperse to a coasting beam. Thus, it is an important part to synchronize the phase, i.e. the velocity of the particles within the bunch during beam alignment. Details about alignment techniques can be found elsewhere [45,50,51].

At GSI both the RFQ and the drift tube LINAC, as well as a number of single resonators were realized as part of the UNIversal Linear ACcelerator *UNILAC*, which makes the system so flexible. Since 1990 the UNILAC serves as pre-accelerator for the heavy ion synchrotron SIS18 [1].
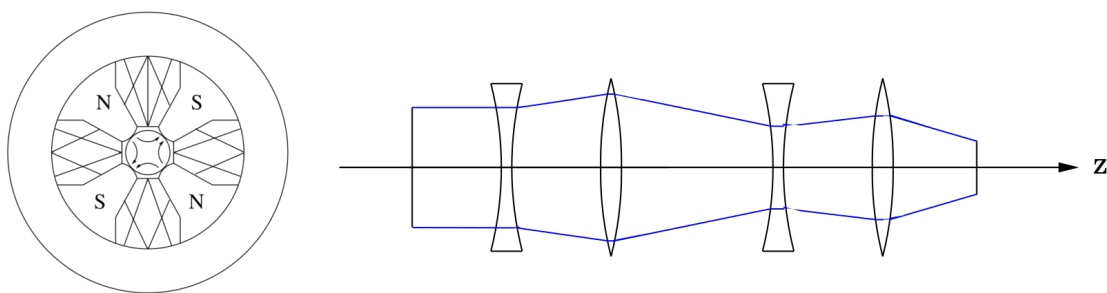
Figure 3.2: Scheme of a Quadropole design in lateral cut (left side) [45]. The right side shows a typical alternating gradient (AG) arrangement of 4 quadrupoles, the blue lines illustrate in principle the focusing of the ion beam in the direction of acceleration z.

The SIS18 (short for *SchwerIonen Synchrotron*, translation: *Heavy Ion Synchrotron*) is a synchrotron ring with 216 m circumference, in which the bunches from the UNILAC are injected. The bunches are bended on the circuit by using the magnetic field of *dipole* magnets. Here, the requested beam energy E (e.g. given in MeV) or specific beam energy E_{spec} (typically given in MeV/u or similar) can be achieved by low power RF cavities by multiple turns in the synchrotron.

Also by magnetic forces, *quadrupoles* are used to focus the ion beam in one plane transversal to the acceleration. The focusing in the other plane is in general performed by another quadropole element with 90° rotation to the previous one. The arrangement is abbreviated with FODO cell (Focusing, drift space, Defocusing, drift space). An example of a FODO arrangement is shown on the right hand side of figure 3.2. The left side of figure 3.2 shows the lateral cut of a single Quadrupole [45].

Small errors on the installed magnets can lead to deviations of the beam from the ideal axis or even to beam loss. Therefore, it is essential to control the machine parameters simultaneously with the beam alignment. The use of scintillation screens as diagnostic tool in in this field will be explained in section 3.2.

3.1.1 Extraction from Storage Ring
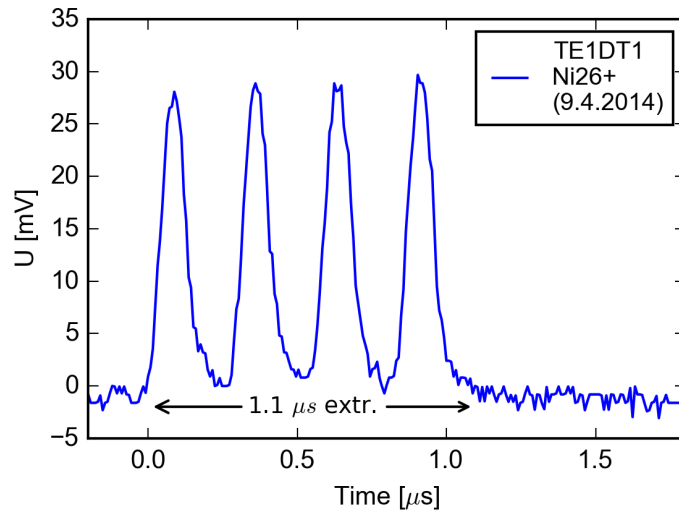
Figure 3.3: Measurement of a Ni beam pulse right after extraction from SIS18. The pulse was separated into 4 bunches during fast extraction, and a pulse duration of approximately 1 μs is observed.

There are two different techniques commonly used for extraction of a particle beam from a storage ring. The so called *fast extraction* makes use of a fast-switching magnet, here called *kicker magnet*. The duration of the extracted ion pulse is determined by the rise time of the maximum field value of the kicker magnet and lies typically between micro- and nanoseconds [52]. The typical duration of a fast extracted pulse from SIS18 is around 1 μs. Figure 3.3 shows the measured signal, that a fast extracted Ni^{26+} beam induced in the diagnostic current transformer in the extraction line of SIS18. The complete pulse duration was 1.1 μs and exceeded the described scintillation rise time by orders of magnitude (see section 2.4.3). Nevertheless, the occurring of temporal quenching will be investigated in this thesis.

Slow extraction at SIS18 is performed by controlled excitation of the horizontal betatron amplitudes. By extracting the particles over multiple turns, the extracted pulse gets a smooth and uniform spill with a duration of a couple of seconds [53,54]. At GSI slow extracted pulses from SIS18 can be set to durations between 300 ms and a couple of seconds. Figure 3.4 shows the measurement of the ion beam current during a beam time in slow extraction mode: The small flat top on the left corresponds to the injection from UNILAC into SIS18, followed by the acceleration (increasing slope). The beam is generally stored

in the ring (illustrated by the flat top after acceleration) until the extraction is induced, here within 300 ms. More details about the requested extraction times will be given in the experimental chapters.
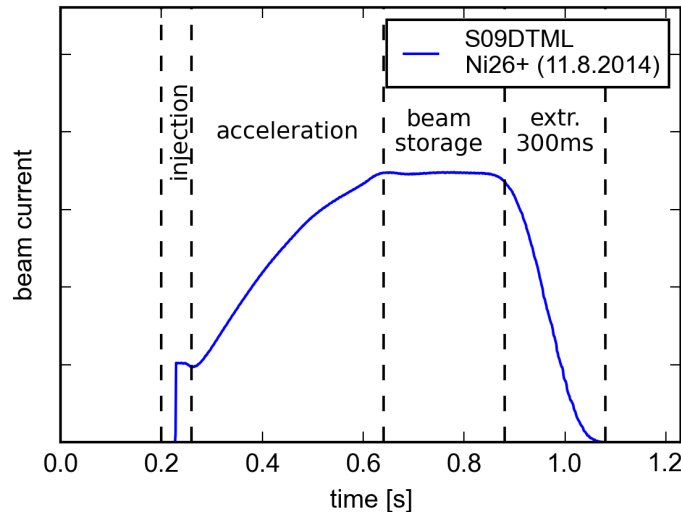

Figure 3.4: Measurement of beam current in SIS18, visible is the injection, the acceleration, the beam storage and the extraction of the beam, the extraction time was here 300 ms

We know from the description of the general scintillation process (section 2.2), that the rise time of scintillation in inorganic materials can be approximately 10 ps with variation of a factor 100. However, it is expected that the behavior of the scintillation screens can be used independent of the extraction mode for beam alignment. To investigate the general differences between both modes as well as any occurrence of quenching the measurements in slow and fast extraction mode will be performed and compared for the thesis.

3.2 Scintillators as Diagnostic Tool for Beam Alignment

Due to their capability of absorbing radiative energy and transform it into visible light, scintillators are a common and simple tool to detect radiation of various kinds. In the following the characteristics, that define the applicability of a certain scintillation screen, are listed on hand of [35]:

- To gain a high energy deposition according to Bethe-Bloch equation (2.1), the target material should provide a high density ρ. Typical densities can lie between $2.4 < \rho < 8.4 \, \frac{\text{g}}{\text{cm}^3}$.

- As explained in section "2.5 Defect Formations" the point of quenching is a material specific characteristic. A scintillator should thus be chosen such, that the amount of deposited energy from the radiation source results in a constant or at least linear response of the scintillation.

- The light yield Y as defined in equation (2.6) should be as high as possible. Y is usually given in photons per MeV and reach orders of e.g. $51000 \, \frac{\text{photons}}{\text{MeV}}$ for Thallium-doped Natrium Iodide crystal [35]. In general the light yield of a medium can be increased by doping with an activator [34, 35, 55].

- For practical use of a scintillation screen as diagnostic tool, a fast luminescence decay time should be provided. As already mentioned, defects can influence the decay and can induce an afterglow.

The decay times of commercially available scintillation materials span over a wide range from ns to ms.

- Independent from a high emission efficiency / light yield, a scintillator should have a good stability under irradiation, in the best case even in strong radiation conditions. The properties of a scintillation screen should be ideally constant, even under long time irradiation, to provide reliable responses at each point of a measurement.

- Last but not least the production of a scintillation screen should be feasible and cost-effective and provide an adequate surface area. Also the handling of the screen, i.e. the mechanical stability and transportability are important challenges when choosing a scintillator material.
  Only mentioned rarely in literature, even though important for a use as diagnostic tool, is a benefit to provide minimal outgasing under vacuum conditions. This criterion is limiting e.g. the choice of glue during production of a phosphor screen.
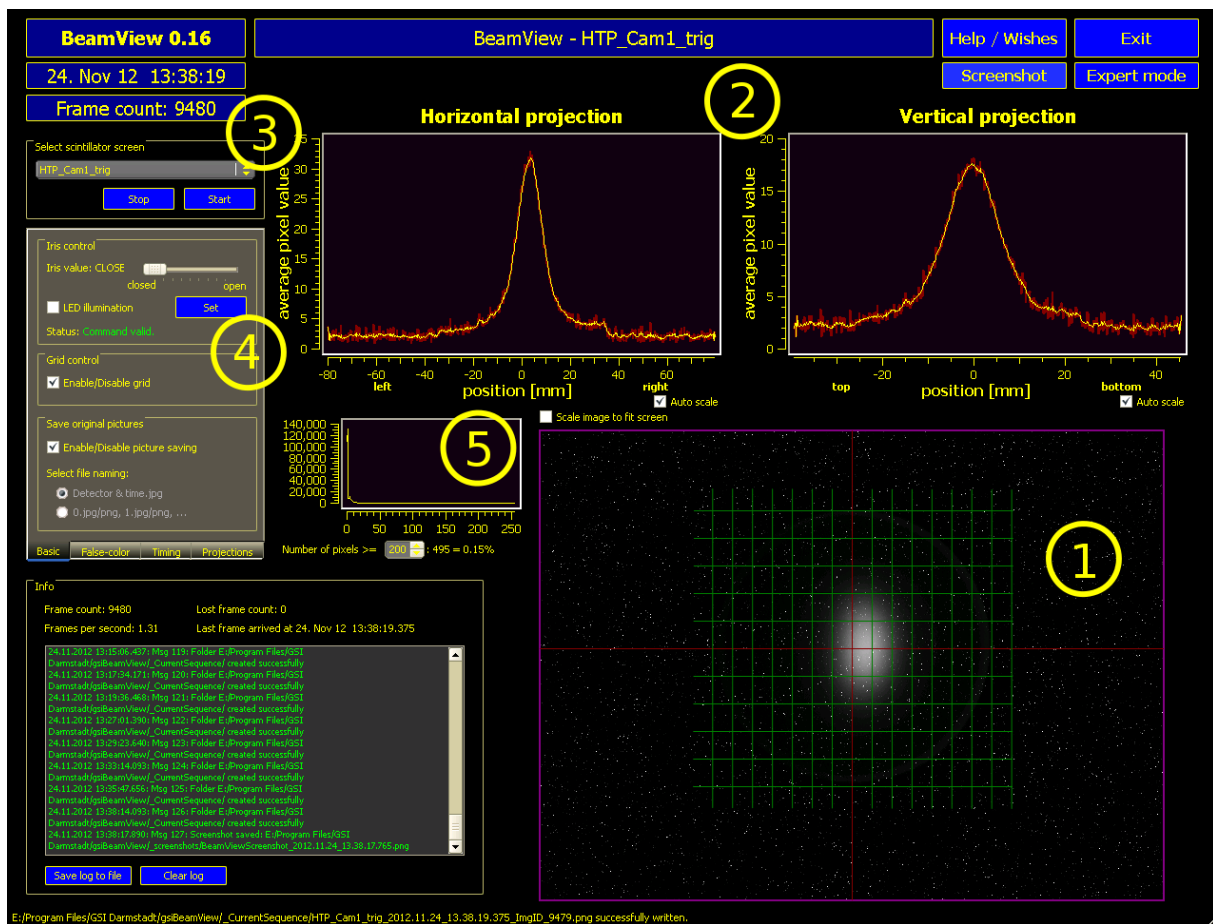
Figure 3.5: Screenshot of scintillation recorded with *BeamView* software [56] induced by an U beam as example for beam alignment in accelerator facilities. (1) record (preview), (2) horizontal and vertical projection, (3) camera selection, (4) iris setting, (5) gray scale value control

In accelerator facilities scintillation screens are nowadays a common tool in beam alignment [56–59]. They are usually installed in an intercepting way in the beam line and the induced scintillation supply immediate informations about the position and size of the irradiating particle beam. By recording single

triggered pictures or a video stream with a common CCD camera, an on-line alignment of the beam is easily possible.

An example of beam record is given in figure 3.5, measured with the GSI software *BeamView* [56] during alignment of an uranium beam. The recorded scintillation is shown in the magenta framed window (1) and overlaid with a grid as tool for centering. The red cross marks the center of the target and/or beam line. The projections of the beam spot are shown beyond that in horizontal and vertical direction (2). On the upper left side the camera can be chosen (3) and the iris opening can be set (4). It is recommended to open or close the iris such that an over-exposure of the camera is avoided. This feature is controlled in the small window in the middle (5).

Advantages of the applied method lie clearly in the direct and fast[2] imaging of the beam. In general, they can be installed in air or in vacuum without the risk of evaporation, and the emission can be recorded through a viewport, without the need of an electrical feedthrough. In combination with a *pepper-pot* mask, i.e. a plate of radiation hard material (e.g. tungsten) having a matrix of holes, the angular deviation and the two-dimensional size of the beam can be measured and thus offers a tool for emittance measurement [58]. In contrary to the similar working profile grids, scintillation screens do offer a higher transversal resolution, usually limited by the recording camera system. The image of a homogeneous beam spot, as shown in figure 3.5, can even lead to the impression, that the real beam is recorded by the camera, instead of the scintillation response. Nevertheless, the screens do not offer a complete diagnostic solution, since they destroy the recorded beam without providing informations about the beam intensity. Different devices exist to measure the beam intensity and the used techniques will be explained in section 4.1.2. In order to develop non-intercepting complete-diagnostics for beam alignment different research projects exist, as e.g. Beam Induced Flourescence (BIF), Beam Position Monitors (BPM), Ionization Profile Monitoring (IPM) and Optical Transition Radiation (OTR) [58,60,61]

3.3 Classifications of Inorganic Scintillator Materials

Altogether seven inorganic scintillation targets were investigated. In order to support the design of beam alignment diagnostics for FAIR, the collection contained phosphor powders as well as single crystals and two ceramics. They can be classified by three chemical compositions that will be described in the following sections. The targets are present in the phases *phosphor powder*, *single crystal* and *polycrystalline ceramic*. Due to the necessary dimensions[3] of each target, they were installed at the end of the beam branch in air. For this reason neither the material stability nor the emission characteristics under vacuum conditions were tested.

3.3.1 P43 Phosphor - Gd_2O_2S:Tb

The scintillation screens, made of phosphor powder Terbium-doped Gd_2O_2S, are commonly abbreviated with *P43 phosphor* [62]. First distinguished studies about this material were performed in the frame of

---

[2] The necessary camera exposure times are in the region of some hundred ms for typical beam alignment.
[3] The natural repulsion of the ions leads to an increasing of beam emittance. However, the last focusing magnet before the experimental area has a distance of nearly 11 m to the targets. To guarantee the measure of the full beam dimension, the diameters of the targets screens were chosen in the range of 5 to 8 cm per screen.

X-ray studies for medical and industrial applications [63,64], where it is still a favored choice as detector material. Since then research on the luminescence properties with different irradiating projectiles led to an increasing interest in P43 phosphor screens as detector for radiation [65–67]. Since 1949 the fabrication process has been improved. In general, the material is mixed with water-binder-solution and the liquid is decanted and dried out after a settling time. Grain sizes of 25 μm down to 1 μm are achievable [68].

Due to the promising high scintillation efficiency and the conventional use of P43 phosphor in medical imaging devices, one of the investigated targets was a P43 phosphor screen, provided by ProxiVision [69]. In the present proceeding, this target will be labeled with the number "#1". As key parameters the supplier gives a coating thickness of 50 μm, built by multiple layers. Standard grain size is 2-3 μm. The decay time down to 1 % of the initial luminescence is given with 2.6 ms and the photon yield induced by electronic irradiation is 60000 photons/MeV. The material density is given with 7.21 $\frac{g}{cm^3}$ [69]. Such a relatively high density results in a high energy deposition, regarding equation (2.1), and thus in a generation of high light output. Therefore the selection of P43 phosphor as material in a scintillation diagnostic tool is already favored in accelerator facilities [6–8].
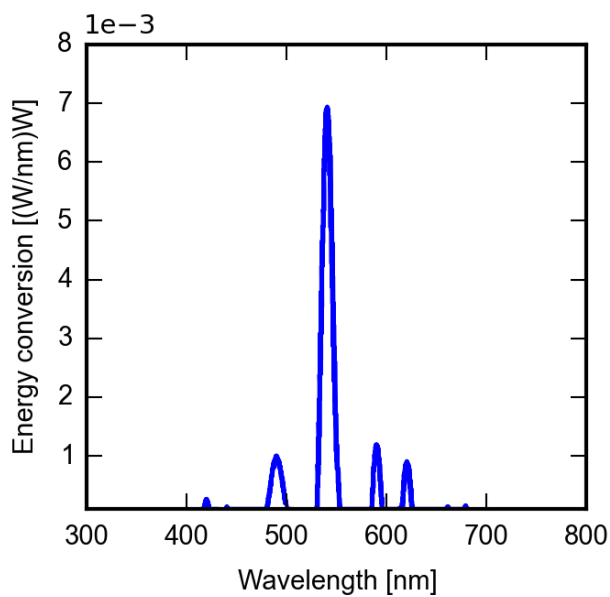
(a) Emission spectra of P43 phosphor given by supplier [69]

(b) Photo of P43 phosphor screen

Figure 3.6: P43 phosphor target #1

Figure 3.6a shows the emission spectrum of P43 phosphor under Radioluminescence, given by the supplier [69]. It shows a discrete distribution with a clear emission maximum at 545 nm (green region). This is due to the transition of the Tb dopant from $^5D_4$ to $^7F_5$. Other transitions are induced from $^5D_4$ to $^7F_6$ (485 nm), from $^5D_4$ to $^7F_4$ (590 nm) and from $^5D_4$ to $^7F_3$ (620 nm) [65,70]. Possible transitions induced by the matrix element Gd^{3+} are documented by Mares et al. [71], but this luminescence occurs in UV region and is therefore not recorded by the used experimental setup. Other publications show similar spectra of P43 phosphor under X-ray [65] and proton stimulation [66].

The decay time of P43 phosphor lies in the range of $\approx$ ms, which is comparatively high for a scintillation screen in accelerator application. Da Silva et al. [72] excited different Tb^{3+} transitions and measured the corresponding lifetimes of the scintillation output. Their results show that mainly the green emission at $\lambda_{em} = 544.5$ nm is responsible for luminescence times of approximately $\tau \approx 1.5$ ms and as reason a competition between the $^5D_4$ to $^7F_5$ and the non-radiative $^5D_3$ to $^5D_4$ transition is given. A shorter transition is observed close to the UV region at $\lambda_{em} = 417.5$ nm with a luminescence time in the range of $\tau \approx 0.3$ ms. Here, the responsible transition happens from $^5D_3$ to $^7F_5$ [72]. But as shown in the emission spectra in figure 3.6a, this transition has a low scintillation efficiency and is therefore rarely observed in parallel to the rest of the emission of P43 phosphor.

3.3.2 Cerium-doped Yttrium Aluminum Garnets - $Y_3Al_5O_{12}$:Ce

Historically the non-silica garnet $Y_3Al_5O_{12}$:Ce was developed as host material for LASER industries [73]. It cannot be found in nature and has to be synthesized by a Czochralski process [74]. For this purpose, iridium is used as crucible container and from a seed grain of Yttrium-aluminum garnet the crystal is growing in mono-crystal formation. Rod wafers can be cut from this crystal and are used in polished form in various applications. First commercial use of Czochralski process was performed in 1960s by Paladino and Roiter [75] as well as by Rubin and Van Uitert et al. for Linde company [76]. A screen, made of the phosphor powder of Cerium-doped YAG, is called *P46 phosphor* [62].

The group around Koningstein et al. investigated the crystal structure of different Aluminum Garnets, including Yttrium Aluminum Garnet in undoped form (YAG) [77, 78]. By Raman and Infrared spectroscopy they found that the undoped YAG structure is built as a distorted body-centered cubic system. Eight units of $Y_3Al_2(AlO_4)_3$ group forming a D_2 symmetry around the yttrium ions in the center. The (AlO_4) units are placed around the D_2 and build a tetrahedron with S_4 symmetry, while the Aluminum ions (Al or Al_2) form a C_{3i} symmetry at $\frac{2}{3}$ of the surrounding place of the D_2 group. The structure offers a good stability with respect to its mechanical, thermal and chemical properties and presents a great ability to include rare-earth dopants [79].

(a) P46 phosphor #2   **(b)** P46 phosphor #3   **(c)** YAG:Ce single cr. #4   **(d)** YAG:Ce s. cr. #5
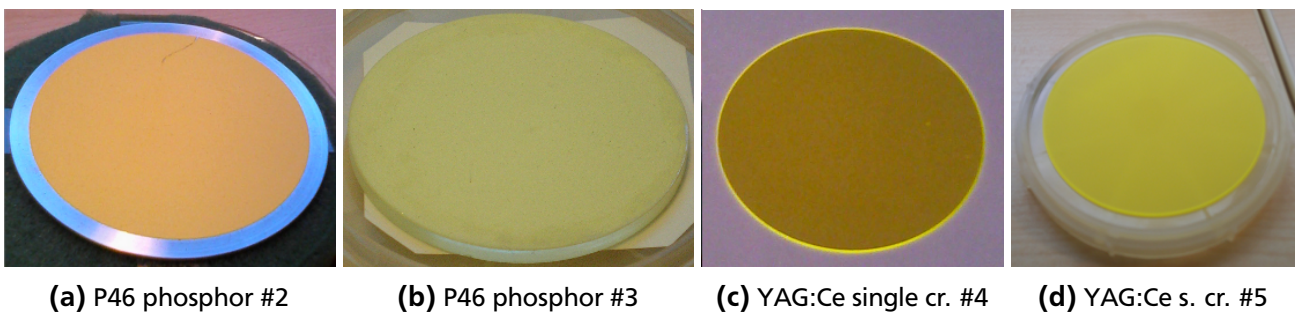
Figure 3.7: Photos of $Y_3Al_5O_{12}$:Ce targets

Since YAG:Ce single crystal represents one of a typical target material, recommended for the detection of various imaging systems [69,80,81], and after experience of previous beam alignment research [5,6], altogether 4 target screens made of Cerium-doped Yttrium Aluminum Garnet were chosen for investigations. One half of the targets were available as conventional single crystal. The other half was present

as P46 phosphor and supplied on appropriate sample holders. P46 target #3 was manufactured by using the waste of the cut process of YAG:Ce single crystal #4 and has thus identical chemical composition [80]. In table 3.1 the key parameters the four investigated $Y_3Al_5O_{12}$:Ce targets are summarized. For target #4 from SaintGobain the thickness was measured using a caliper to 1.095 mm. Photographies of the targets are shown in figure 3.7

Table 3.1: Key parameters of investigated P46 phosphor and YAG:Ce single crystal targets given by corresponding suppliers [69, 80, 81]

Sample	P46 #2	P46 #3	YAG:Ce #4	YAG:Ce #5
Supplier	ProxiVision [69]	Crytur [80]	Crytur [80]	SaintGobain [81]
Phase	powder crystal	powder crystal	single crystal	single crystal
Density $\left[\frac{g}{cm^3}\right]$	—	4.55	4.57	4.55
Thickness	50 μm	100 μm	250 μm	1.095 mm*
Decay Time	300.09 ns	60 ns	70 ns	70 ns
Photon Yield $\left[\frac{10^3\gamma}{MeV}\right]$	—	—	35	8

The values of photon yield in table 3.1 were given by the suppliers, if available, and offer a great dynamic range. Many investigations in the light output were performed within the last decades due to the wide use of this crystal in LASER technology. In general a light yield around 20000 ± 3000 γ/MeV for Ce-doped YAG is given in publications [82–84].
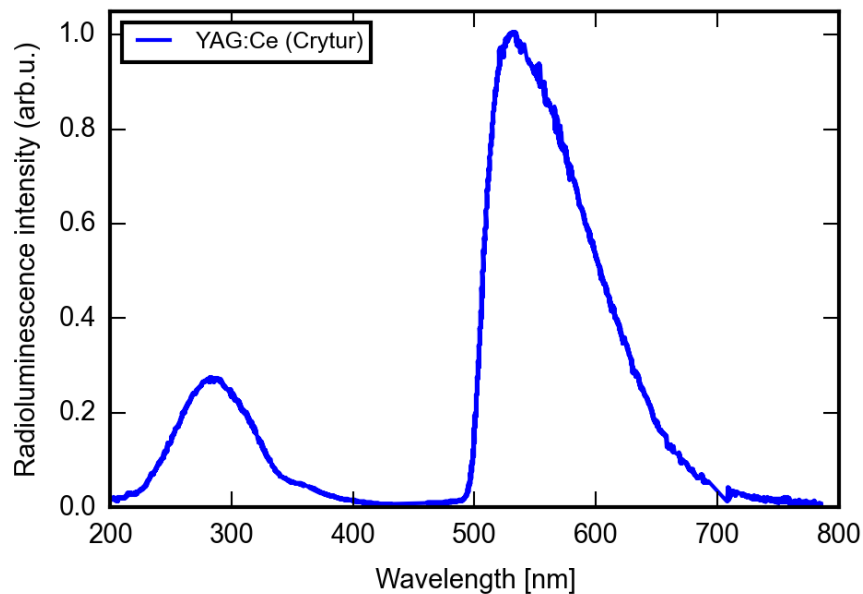
Figure 3.8: Emission spectra of Ce-doped YAG single crystal, data from Crytur [80]. For a P46 phosphor a similar spectra is expected.

Figure 3.8 shows the emission spectra of a Ce-doped YAG single crystal as given by Crytur [80]. It was measured under radioluminescence and shows two emission bands: the main emission has a peak at 530 nm. From investigations of Zych et al. it is known, that this emission band is characterized by the grain size of the material and that this part of the distribution is tending to higher wavelengths and lower

intensity with decreasing grain size [85, 86]. Nevertheless, the emitted color corresponds to the Ce^{3+} dopant and is broadened to a band, due to spin-orbit interactions of the ground state 4f: The excited Ce^{3+} dopant falls from the 5d state into the 4f ground state either into $^2F_{5/2}$ or into $^2F_{7/2}$ state [79, 87]. A smaller emission band of the spectrum has its maximum in the UV region at 285 nm and is originating from the matrix material. In literature this emission band is usually mentioned to be suppressed or is not observed, as e.g. in the publication of Mihóková et al. [87].

3.3.3 Aluminum Oxide Ceramics - Al_2O_3 and Al_2O_3:Cr

Since 1969 ceramics, made of chromium-doped aluminum oxide, are nowadays a conventionally used material in beam diagnostics of accelerator facilities, due to their high efficiency and the stability in emission and material characteristics, even under vacuum conditions [88]. However, the material needs to be extracted from mining and so the production of screens reached its limits in the 90s. Since than, the quest for materials with comparable scintillation efficiencies and radiation hardness are a subject of recent research. Although offering less efficiency, pure aluminum oxide is a promising candidate as diagnostic tool due to it's high stability against ion irradiation [89].

The structural space group of Aluminum Oxide is rhombohedral with a triagonal $R\bar{3}c$ symmetry. The point symmetry is of type C_3 for Al atoms and of C_2 for O atoms. It contains two Al_2O_3 groups per unit cell. In the unit cells the Al atoms are placed octahedrally with respect to two O atom layers [90, 91].

Two targets made from polycrystalline Aluminum Oxide ceramic were ordered from ceramics manufacturer BCE [92] for investigations. While one target is an undoped material with a given purity of 99.99 % (called: *A999*), the other ceramic screen is doped with Chromium (called: Al_2O_3:Cr). For the latter BCE gives an amount of 0.04 weight-percent Cr doping [93]. Each target has a thickness of 0.8 mm, a diameter of 80 mm and the densities were calculated on the basis of measured weight[4] to:

- $\rho_{A999} = 3.94 \frac{g}{cm^3}$

- $\rho_{Al_2O_3:Cr} = 3.73 \frac{g}{cm^3}$

The spectral emission of A999 was investigated by Evans [94] and the luminescence spectra, recorded by photon excitation, are shown in figure 3.9a. The energies, that were used for excitation, are listed in the legend. The luminescence is a superposition of emissions, resulting from F and F^+ centers in the material and lie mainly in the UV region. This makes it very difficult to investigate the emission spectra with common optics, and it is supposed that the emission band is recorded only in suppressed form (see section 4.2.3).

The emission spectrum of Chromium-doped Aluminum Oxide during irradiation with U beam is shown in figure 3.9b [5]. It is dominated by the red Cr line at $\lambda = 695$ nm. This emission comes from the transition from ^2E (lowest excited state) to the ground state $^4A_2$ of the dopant Cr^{3+} and is unfortunately relatively long with $\tau \approx 3.4$ ms [95]. A competing emission is visible at $\lambda = 674$ nm. It vanishes during irradiation due to material degradation [4]. In principle the UV emission of the matrix material (see figure 3.9a) also happens, but this is of orders lower than the red emission and thus not visible.

---

[4]   Thanks to GSI target laboratory
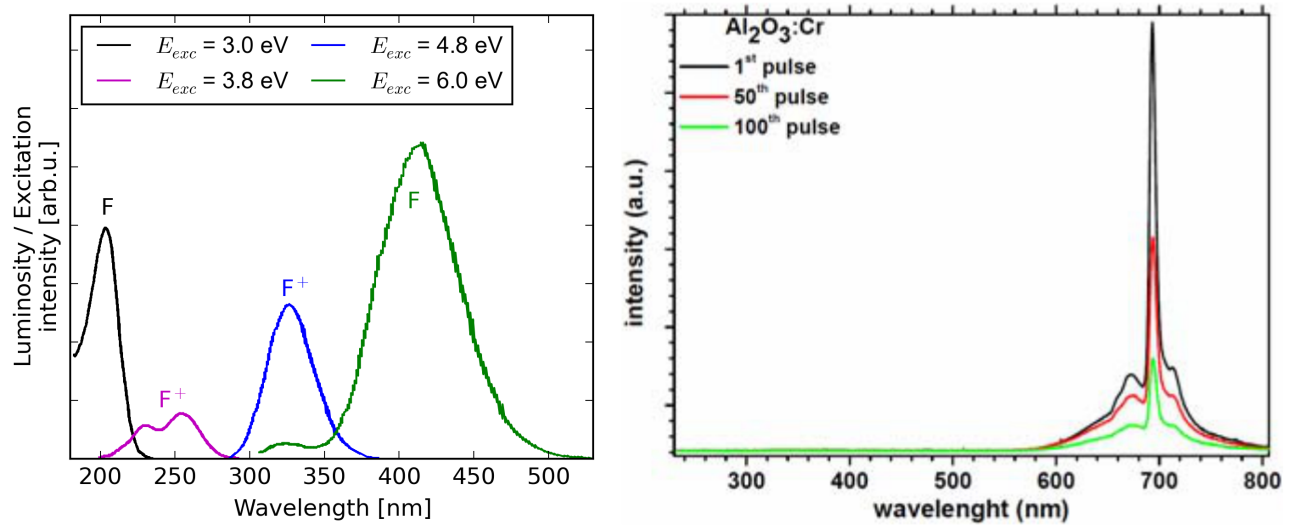
(a) Excitation spectra of Aluminum Oxide, from [94]. (b) Luminescence spectra of Al_2O_3:Cr irradiated with Uranium pulses with 4.8 MeV/u [5], the luminescence decrease is a result of material degradation.

Figure 3.9: Emission spectra of pure and Cr-doped Aluminum Oxide, as given in literature

4 Ion Beam Experiments

The extracted ions from SIS18 are aligned through the 170 m long High Energy Beam Transfer line (HEBT) to the experimental area, called HTP. An overview of HTP is shown in figure 4.1b. Various diagnostics devices are used in the HTP branch to measure the characteristics of the beam in front of the scintillation targets. The setup at HTP is described in this chapter. The description is divided in two parts.

In the first part the parameters of the irradiating beam are presented as well as the devices for measurement of the different beam characteristics will be explained. In the second part the optical system, that was used to record the scintillation response on the targets is described.

4.1 Beam Parameters and Experimental Setup

For the present work possible quenching effects, caused by increased number of irradiating particles or shorter pulse lengths were of major interest. At the same time the irradiating ion type was varied, looking at the response and stability of the different screen materials. Therefore two types of measurements were basically performed, namely the variation of beam intensity and pulse length at different screens on one hand and on the other hand the variation of beam ion species on all screen materials. Unless explicitly mentioned, the energy of requested ion beams were kept fixed for both methods and the ion bunches were requested in slow and fast extraction mode.

4.1.1 Beam Intensity Variation

In total five different ion types from *proton* to Uranium (U) were requested from SIS18 with a beam energy of 300 MeV/u. The beam intensity were varied between 10^6 and 10^{10} particles per pulse (short: *ppp*) and irradiated the scintillation targets successively. Depending on the recorded luminosity a number of pulses between 30 and 120 were used for each beam intensity and target combination. An overview of the performed beam times with varying intensity is given in table 4.1. The numbers given in the first column will serve as reference for similar tables in the following.

Table 4.1: Overview of requested projectiles at varying beam intensities

	projectile	Atomic Mass A	Atomic Number Z	appr. range of requested ppp
#1	proton	1.0	1	$5 \cdot 10^7$-$1.5 \cdot 10^9$
#2	Nitrogen (N)	14.0	7	10^7-10^{10}
#3	Nickel (Ni)	58.69	28	10^7-10^9
#4	Xenon (Xe)	131.29	54	$7 \cdot 10^7$-10^9
#5	Uranium (U)	238.03	92	$2 \cdot 10^7$-10^8
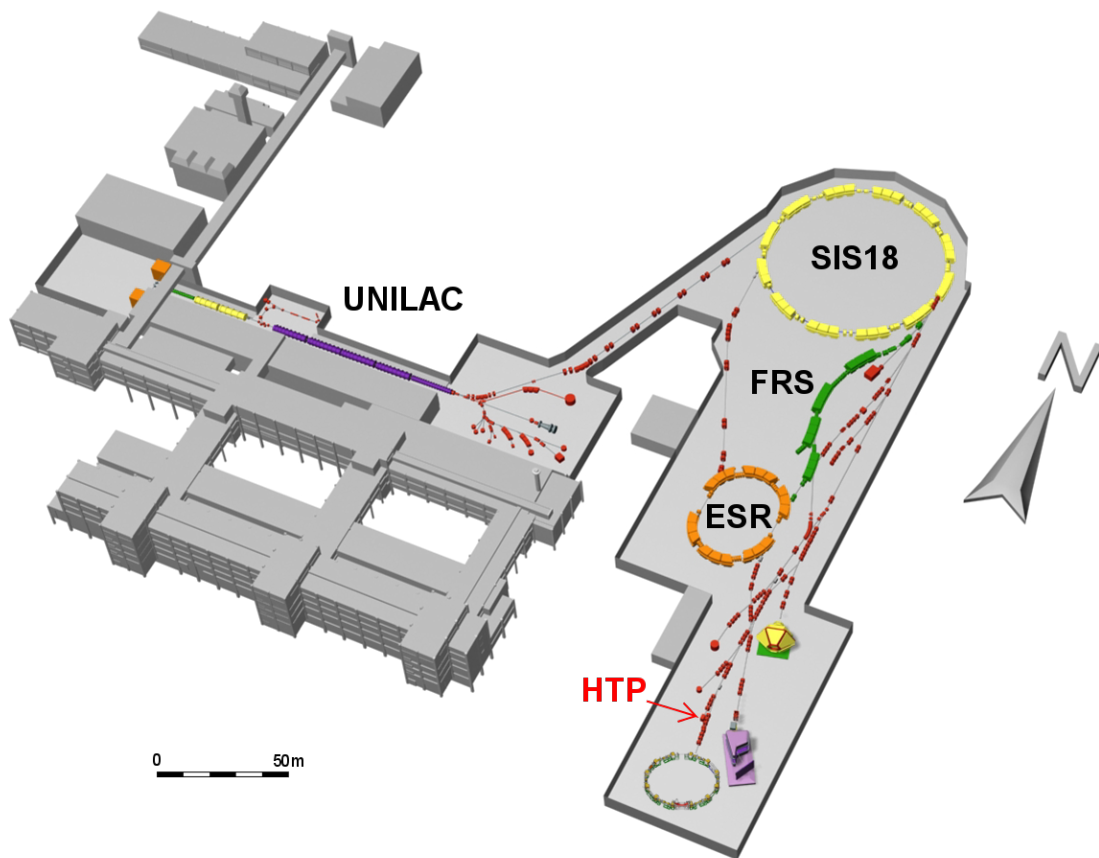
(a) GSI facility with location of HTP [96]
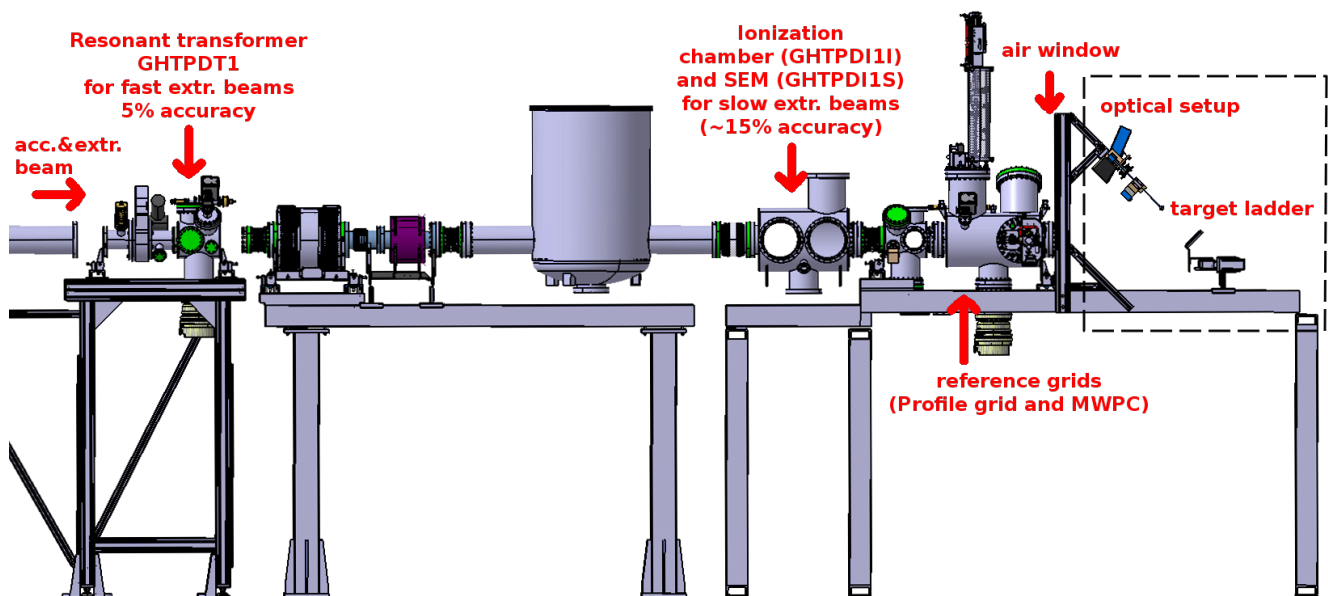
(b) HTP setup in detail, the box marks the dedicated setup for the thesis

Figure 4.1: GSI facility and HTP beam line

The upper limit of requested beam intensity is defined by radiation protection authorities. At the area, where the measurements were performed, a maximum number of 10^9 particles per **second** is allowed to be requested. An exception of that rule was the Nitrogen beamtime, at which it was decided to change the pulse frequency, so that beam intensities of 10^{10} ppp were available for the measurements.

To investigate the stability of the scintillation materials during longtime irradiation, radiation hardness tests were performed in slow and fast extraction mode. For this purpose a *Ni* beam was requested with 300 MeV/u and a beam intensity of $2 \cdot 10^{10}$ ppp. The targets were irradiated with approximately 1000 pulses each before a controlled beam break was performed. Another 100-150 pulses were applied to the targets after the break to check for any permanent modifications of the materials.

Within the present proceeding, the radiation hardness test will be labeled with "#3R".

4.1.2 Supporting Diagnostics Components

The beam intensity of a fast extracted beam pulse can be measured with help of a resonant transformer (short: RT; name of device: HTPDT1). It is built of a ferrite toroid with a winding on two sides and works similar to a resonant $L - C$ circuit [57]: A passing beam pulse induces a damped oscillation with an amplitude, proportional to the charge Q_{acc} of the pulse. The amplitude of the oscillation can be measured on a second winding. The number of particles I_{pulse} can then be calculated by dividing Q_{acc} over the atomic charge of the ions Z and the elementary charge e. I_{pulse} is given generally in ppp.

$$I_{pulse} = \frac{Q_{acc}}{e \cdot Z} \tag{4.1}$$

In a simple RT the maximum measurable intensity is limited by the electric strength, in the case of the installed transformer to $I_{RT,max} = 1$ A. To overcome the limitation a series of resistors is installed in the HTPDT1 system beam intensity and the measurement ranges Q_{ranges} are chosen automatically by the control system [97]. The measurement range was logged together with the measured charge Q_{acc} and the measurement resolution was 10 % of the set measurement range, i.e.

$$\Delta I_{pulse} = \frac{0.1 \cdot Q_{range}}{e \cdot Z} \tag{4.2}$$

The available RT was designed for intensity measurements of fast extracted pulses from SIS18. Thus, it has a large damping period $T >> 1\,\mu$s, resulting in a high resonance frequency $\omega \propto \frac{1}{T}$ of the damped oscillation [57]. A slow extracted pulse can thus not be measured correctly by this device. For these measurements, a diagnostic chamber with altogether three different devices is available at HTP. Two of the devices were used during measurement campaigns and are described shortly in the following:

- An Ionisation Chamber (short: IC; name of device: HTPDI1I) of 6.5 mm depth and filled with a gas mixture (80 % Argon, 20 % CO_2) at atmospheric conditions. The chamber is separated on each side with 100 μm stainless steel foil from the vacuum. During ionization by the beam, the

gas releases electrons, that are collected by two electrodes, made of Mylar® and coated with silver. The measured current is proportional to the beam intensity with an accuracy of 10 % [98].

- A Secondary Electron Emission Monitor (short: SEM; name of device: HTPDI1S) is built here of three 100 μm thick stainless steel foils. By particle impact electrons are released from the middle foil and collected by the two outer foils on positive potential. The resulting current is proportional to the beam intensity [99]. The device has an accuracy of 20 % [98].
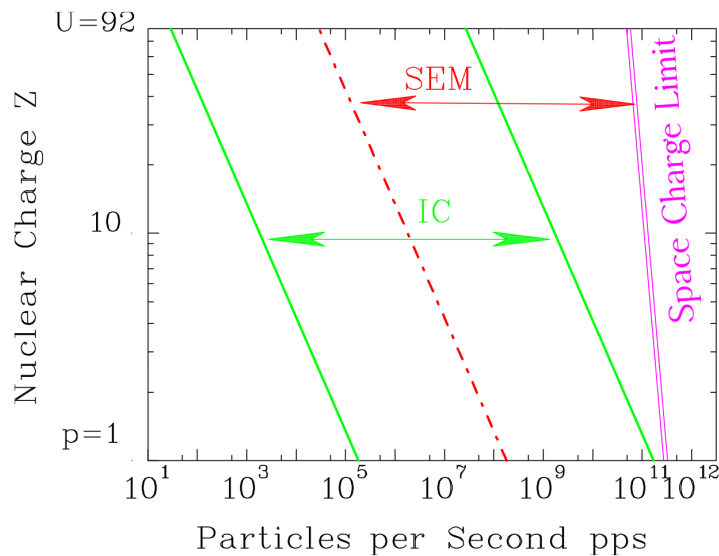

Figure 4.2: Limits of the Ionization Chamber (IC) and the SEM in the diagnostic chamber at HTP in dependence of the atomic number Z of the irradiated ion, calculated for different ions at 1 GeV/u with 1 s extraction time, adapted from [58].

While the IC saturates for heavy ions at beam intensities around 10^9 particles per pulse the SEM can measure up to 10^{11} particles per second [98]. Thus the number of measurable particles per pulse is strongly limited for the devices and is dependent on the pulse duration, the energy and the atomic number Z of the incident ion beam. The operation region of IC and SEM are shown in figure 4.2.

Separated measurements at GSI showed, that parts of the read-out system behind the diagnostic chamber were calibrated imprecisely. Thus, the IC was overestimating the real beam intensity by 6 %, while the SEM underestimated the beam intensity by 8 % [100]. During the performed beam times for this thesis, the particle measurements from both diagnostic devices were recorded and corrected during analysis. For further minimization of the systematic error only the beam intensities from the SEM were used, if possible in the matter of measurement sensitivity.

4.1.3 Target ladder

All investigated scintillation screens were mounted on a target ladder in air, as shown in figure 4.3, with a bias angle of 45° to the beam direction. Appropriate aluminum adapters were used to mount all targets onto the same surface plane, even if different thickness and diameters were available.

On the seventh position of the ladder a dedicated alignment screen was mounted, made of Chromium-doped Aluminum Oxide and with grid lines on the surface. The screen was provided by the GSI beam instrumentation group and similar targets are installed all over the accelerator facility. The sixth position of the target ladder was used by another PhD student and is unimportant for the present thesis. No material was set into the fifth position of the ladder to keep the way free to the beam dump.

Figure 4.3: Target ladder

The scintillation screens had a target diameter between 5 and 8 cm (for details see section 3.3), even though a smaller diameter would have been sufficient, in terms of material science. However, the last focusing diameter in the beam line was installed more than 11 m before the target ladder, so that a strong focusing to less than a few cm or even less than 1 cm was not guaranteed. Additionally, the chosen diameters offered the possibility to intentionally defocus the beam and so increase the diameter of the recorded scintillation spot. In turn, the resolution of the recorded images was used in a larger dynamic range.

The ladder was mounted on a motor drive and the horizontal position was remote-controlled with IclA easy software from Berger Lahr [101]. A scheme of the used cabling is shown in figure 4.4. The system offered more than 280000 increments as number of possible positions, so that a centering of the targets to the recording camera system was guaranteed. The vertical centering of the targets was carried out before beam times with help of the designed construction scheme and the resulting distances. The alignment was controlled after mounting with help of BeamView and a centered grid, superimposed over the camera record.

4.2 Optical Setup

The scintillation response of the targets was recorded with a complex optical system, as illustrated in figure 4.5. It was installed in backwards direction with a topview on the target surface. The tilting
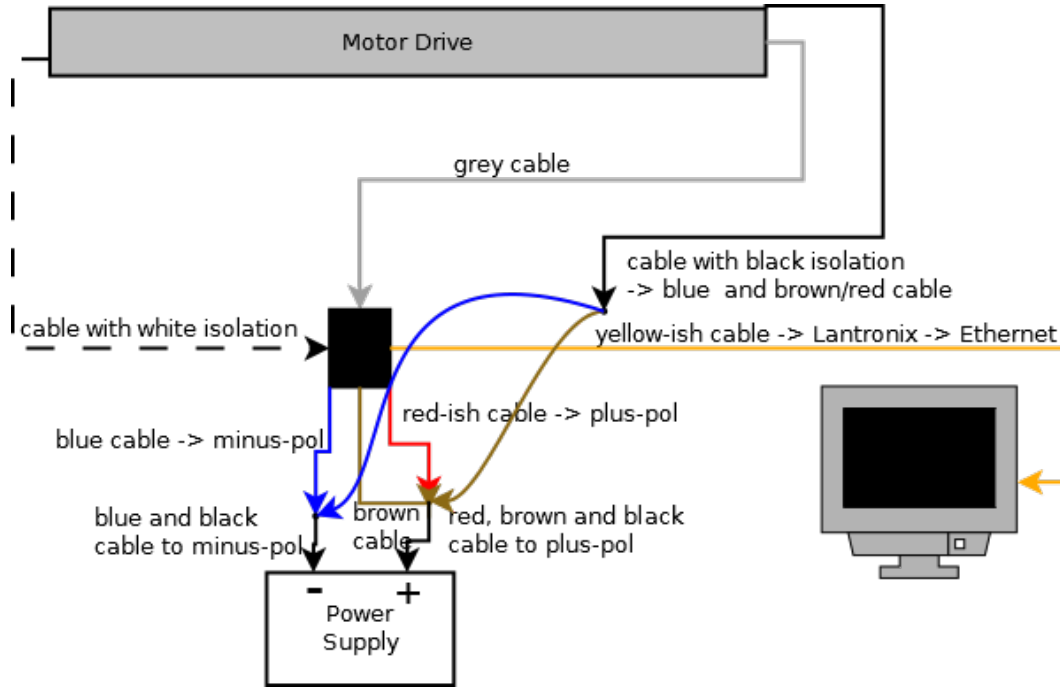
Figure 4.4: Cable scheme of motor drive, used for investigations

angle of the target ladder results in a stretched projection of the beam pulse on the targets. The vertical dimension h_{org} of the original beam pulse is stretched into h_{rec} with:

$$h_{org} = h_{rec} \cdot \sin(\alpha) \stackrel{\alpha=45°}{=} \frac{h_{rec}}{\sqrt{2}} \tag{4.3}$$

The recording system contained one camera with a direct two-dimensional view on the target surface and a spectrometry setup, to investigate the spectral emission. Since both optical setups used cameras with a CCD chip for image recording, a short introduction to the principle of CCD is given, before the setups are described.

4.2.1 CCD components

A CCD-chip is a plate made from a semi-conducting material. The plate is usually split in rectangular regions, the pixels. The typical size for one pixel is $\approx 10\,\mu$m. For every incident photon or charge, electrons are released in the struck pixel. The number of released electrons per photon at a specific wavelength sets the quantum efficiency η [102].

$$\eta = \left(\frac{\text{number of produced electrons}}{\text{number of incident photons}} \right)_{\text{per pixel}} \tag{4.4}$$

There are three common ways to read out the resulting current from the CCD, all working with a configuration of a semi-conducting and a non-light-sensitive material (*read-out area*) [103].
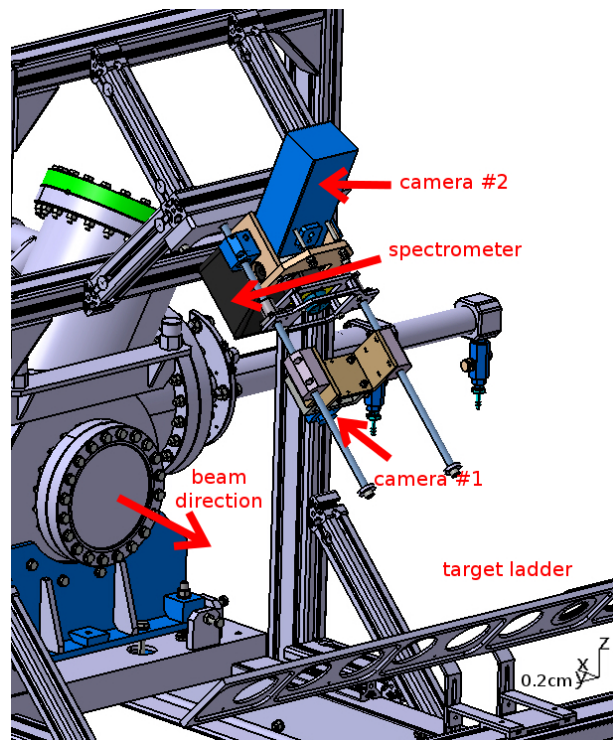
Figure 4.5: Mechanical construction of Optical Setup, drafted by employee of the GSI departement for beam instrumentation (LOBI)

Interline-Transfer (ILT) Next to each semi-conducting row a secondary read-out row is placed. The current of the first row is transported to the nearby register-area and from there in a chain-process to the edge of the CCD chip. This process can lead to *interlacing* between two promptly recorded images. Since the register-area is covered or produced by non-light-sensitive material, the effect of photons that arrive on the chip shortly delayed is minimized (see *smearing* effect in next point).

The time delay that is needed before start of record for one image is called *jitter*. For the used CCD chips of the AVT cameras ("camera #1") the jitter lies typically between 20 and 100 μs [104, 105]. As another disadvantage, this kind of sensor enlarges the non-effective area that the chip covers in a camera housing.

Frame-Transfer In contrary to the ILT process, the register area occupies a space, that is as big as the semi-conducting area. So, the occupied space of the CCD system is indeed doubled, but the effective area of the light-converting chip is maximal.

In chips that use the Frame Transfer method the registering area is not covered and so sensitive to incident photons. If a photon arrives at the chip during current transfer, the original signal is over-exposed and leaves a white stripe on the recorded image. This effect is called *smearing* and depends on the transfer velocity.

Full-Frame-Transfer The register area is kept minimal here: The released electrons from the semi-conducting material are transported over the light-sensitive area to the edge of the CCD chip. Here one register pixel per row collects the current to transport it to the image processing system at the output.

The main advantage lies in the minimum sensor size at maximum effective area. Since the Full-Frame-Transfer usually works of every column at once, also the read out time can be minimized. A clear disadvantage is the high possibility to show smearing.

The read out-process in digital cameras is influenced by noise, which again is caused by the camera electronic, mainly the signal-amplifier [106], the current-to-voltage-converter [107] and the read-out-frequency [103]. This type of noise is called *read noise* or also *readout noise*. In principle it has an absolute level and can thus dominate a record especially in image records with low illumination [102, 107]. The readout noise level of a CCD can be measured as minimum recorded signal, when the CCD is not illuminated [106]. During the beam experiments the measurement of read-out noise was performed by the record of background images shortly before irradiation of the scintillation screens. The background images were subtracted later during data analysis in section "5.2 Offline Analysis of Scintillation Response".

During chip production the creation of *defect pixels* can occur by material imperfections, even though the manufacturers take huge efforts to keep defects at minimum. A distinction is made for defect pixel in three types [102]:

dead pixel: These pixels are not longer able to release electrons, the induced signal is here in general zero or at least minimal.

warm pixel: At irradiation more than the standard amount of electrons is released, the signal is thus shown increased

hot pixel: Independent if irradiated or not, these pixel show a saturated signal

Due to the high-energetic radiation and the short distance of HTP to a beam dump, fast neutrons can generate defect pixels or intensify their degradation. Nevertheless the record of background images without controlled irradiation of the scintillation targets by the ion beam offers the advantage to gain a map of defect pixel for the used CCD camera [108].

Another form of noise per pixel is given by so called "shot noise". It is caused by the natural randomly distribution of an illuminating light and the temporal arrival is dominated by Poisson statistics. Thus, the shot noise is proportional to the square-root of incident signal [106, 107]:

$$\sigma_{shot} \propto \sqrt{\text{number of photons}} \; or \propto \sqrt{\text{incident photon-signal}} \tag{4.5}$$

4.2.2 Camera system to record 2D light output

At position "camera #1" in figure 4.5 a camera either of type *AVT Marlin* or *AVT Stingray* was mounted perpendicular to the target surface. Both contain a 1/2" CCD chip with 8-bit depth and record in monochrome mode. While *AVT Marlin* CCD chip provides a maximum image resolution of 656x494 pixel, the *AVT Stingray* CCD chip has two pixel rows less and thus a maximum image resolution of 656x492 pixel. These resolutions can be achieved in single image mode. When running the camera in "video mode" an image resolution of maximum 640x480 px can be achieved with a video at 60 frames

per second. The integrated CCD chips offer a spectral sensitivity, that covers the visual region. The distribution of the spectral sensitivity is equivalent for both camera types and has its maximum around 500 nm, as shown in figure 4.6a. The data in the figure gives the spectral range from $400 - 1000$ nm, but looking at the distribution one can assume that the CCD records the photons down to a wavelength of $\lambda \approx 350$ nm.
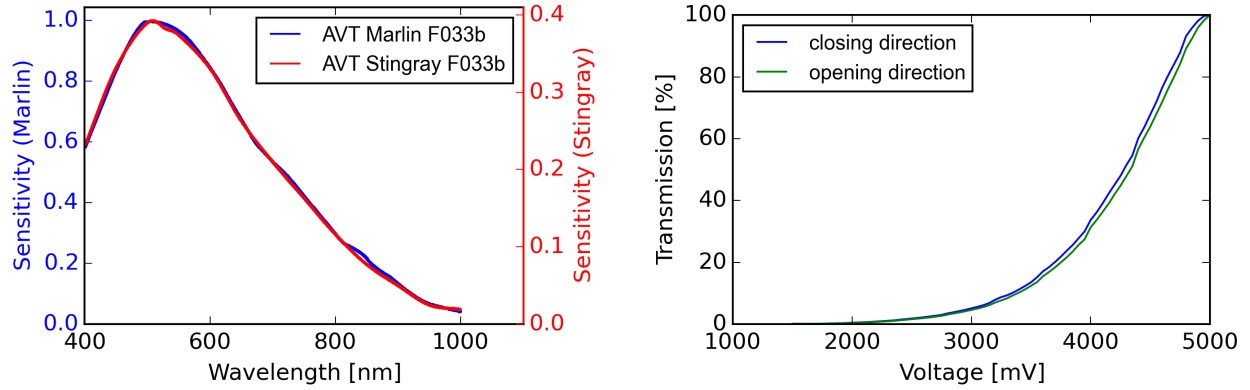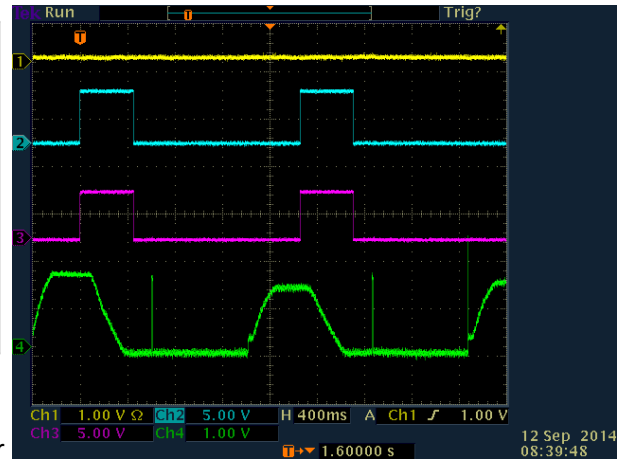
(a) Spectral sensivity of used AVT cameras, as taken from technical manuals [104, 105]

(b) Measurement of transmission through used Pentax Iris
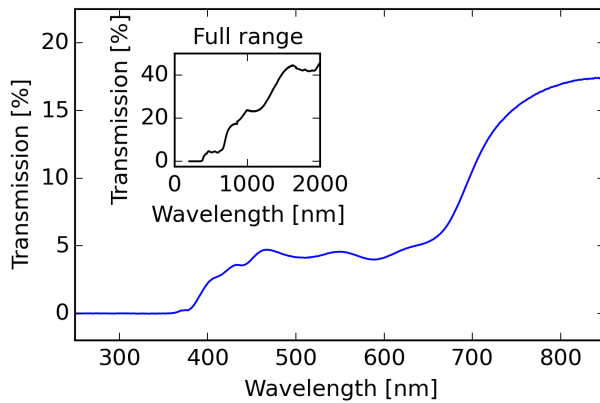
(c) Transmission through used Neutral Density filter *Hoya ND03* within the region that was mainly recorded by the camera system, in the inset the full measurement up to 2000 nm is given

(d) Record of trigger for exposure time of camera #1 (blue line) and camera #2 (magenta line) during slow extraction (green line)

Figure 4.6: Characteristics and triggers of the AVT cameras and optical system

"Camera #1" recorded the two dimensional image, induced on the targets by beam irradiation. The camera was mounted with an angle of $\alpha_{cam1} \approx 3.0°$, i.e. an angle of $\alpha_{cam1\,to\,beam} \approx 48.0°$ to the incident ion beam[1]. The distance from the lens to the target surface was approximately 40 cm. The camera exposure time was kept fixed at 400-500 ms during slow and fast extraction mode to record the full scintillation and eventually occurring afterglow phenomena. To control the camera trigger an oscilloscope was used, that recorded the exposure time of the optical system together with the beam current from the main control system. An example from the trigger is shown in figure 4.6d. With the same exposure time background images were recorded shortly before ($\approx 0.5 - 1$ s) the ion beam arrived at the target. An overview of exposure and extraction times for the performed beam times is given in table 4.2.

---

[1] Equation 4.3 was accordingly changed during analysis.

A *Pentax C1614ER* lens with 16 mm focal length was mounted to the camera. The shot noise σ_{shot} (equation 4.5) was kept minimal with the help of a remote controlled iris. The opening or closing of the iris, respectively, was controlled by a power supply between 1.5 and 5 V and the resulting transmission factor was measured with increments of 50 mV. As a light source a white LED was used and mounted on an Ulbricht sphere to ensure a homogeneous illumination. The result is shown in figure 4.6a It shows a slight hysteresis, depending if the voltage variation is causing a closing or opening of the iris. Between the measurements a difference of up to 4-5 % in transmission was observed at a supplied voltage of 4.6 V.

Table 4.2: Extraction times t_{extr} and exposure times t_{cam1} and t_{cam2} during the measurements

(a) slow extraction

	projectile	t_{extr} [ms]	t_{cam1} [ms]	t_{cam2} [ms]
#1	proton	304	400	400
#2	Nitrogen	400	400	450
#3	Nickel	400 & 450[a]	400	450
#3R	Nickel	300	400	400[b]
#4	Xenon	304	400	400
#5	Uranium	304	400	400

[a] 450 ms for A999 target #6
[b] 400 ms during radiation hardness test

(b) fast extraction

	projectile	t_{extr} [μs]	t_{cam1} [ms]	t_{cam2} [ms]
#1	proton	1.105	400	300
#2	Nitrogen	1.105	400	400
#3	Nickel	1.105	400	400
#3R	Nickel	1.105	400	450
#4	Xenon	1.105	400	400
#5	Uranium	1.105	400	400

Preliminary experiments under similar conditions as given (like shown in table 4.1) offered a wide range of luminescence output for the investigated targets. Furthermore it was observed, that the output range is increased by the variation of ion species [7]. To avoid overexposing of the CCD chip with minor variation of the camera settings and without loss of two-dimensional resolution at the same time a neutral density filter *Hoya ND03* (1.4 mm thick) was mounted in front of the lens. The supplier gives a transmission value of 5 % for this filter averaged over a wavelength region between 400 and 700 nm [109]. Nevertheless, the transmission was measured with help of an Perkin Elmer Lambda 900 UV/Vis spectrometer[2] in the wavelength range between 200 and 2000 nm. The result is shown in figure 4.6c for 250 to 850 nm (blue line) and for the full measurement in the inset. Obviously the transmission shows a huge dynamic in dependence of the wavelength. Especially with beginning IR region ($700 < \lambda < 800$ nm) the transmission starts to rise up to a level of 20 %. Up to 2000 nm the transmission rises even to 40 %, while below 400 nm it is cut off completely.

The measurement displayed in figure 4.6c was used during offline analysis together with recorded emission spectra to calculate a realistic value of transmission through the neutral density filter for each

[2] A detailed description of the spectrometer will be given in section 7.1

scintillation target. A summary of the image processing is given in section 5.2 and details are given in the appendix.

The recorded images of "camera #1" were used for investigations in the light output L, describing a number equivalent to the number of emitted photons. From L the light yield Y was calculated. Furthermore the profiles distribution in horizontal and vertical direction (*beam profiles*) were calculated. The second statistical moments σ_{horz} and σ_{vert} from these distributions served as factor for the calculation of the horizontal and vertical beam width. The calculations are described closer in section 5.2.

4.2.3 Spectrometric system

With a distance of approximately 55 cm from the targets the second optical setup was installed, in figure 4.5 labeled with "camera #2". Here a *Horiba CP140-202* spectrometer [110] was installed with its optical axis perpendicular to the target screens ($\alpha_{cam2} = 45.0°$).

(a) Principle of diffraction of incident light (dotted grey lines) by a spectrograph, template from [111], edited by A. Lieberwirth
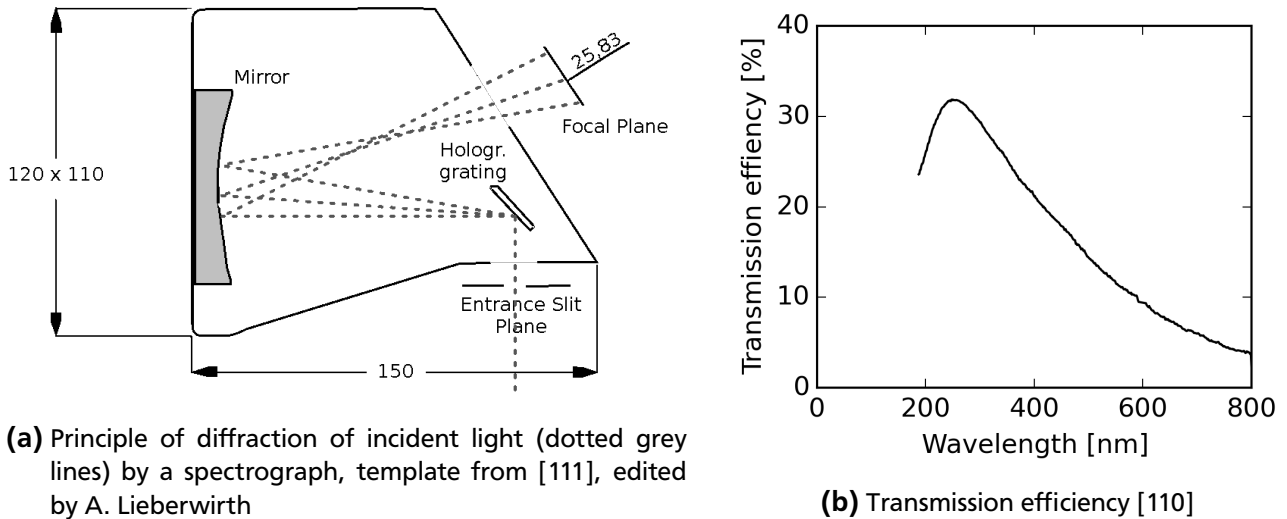
(b) Transmission efficiency [110]

Figure 4.7: Horiba CP140-202 spectrometer

A systematic scheme of the spectrometer principle is shown in figure 4.7a. Photons that enter the spectrometer (in the figure: dotted gray line) are reflected by a mirror onto a diffraction grating (also: *holographic grating*) with aberration correction. The grating is equipped with a high number of equidistant grooves. At the grooves the light waves are reflected with an angle that depends on the wavelength of incident light and the distance of the grooves. This is the formulation of the diffraction law and it's written as [112]:

$$d \cdot (\sin \theta_{incident} \pm \sin \theta_{emitted}) = n \cdot \lambda \qquad (4.6)$$

Here, d is the distance between two single grooves, $\theta_{incident}, \theta_{emitted}$ are the angle of the incident and the emitted light, respectively, λ is the specific wavelength of the diffracted light and n is an integer. So, all light rays with a wavelength, that is not a multiple unit n of the incident wavelength, are destroyed by

destructive interference. The remaining rays are dispersed with a resolution, that corresponds minimum to the number of grooves per mm [112].

The diffraction within the spectrometer leads to a loss of light intensity, that is not linear over the spectral range. The transmission efficiency of the used spectrometer is shown in figure 4.7b. It has a maximum around 280 nm with 32 % transmission.

The spectral range of the system was calibrated with an *OceanOptics CAL2000* Mercury-Argon lamp, that offers a discrete spectrum in the range of 250 till 920 nm. To avoid blurring by overexposure a covering slit was mounted at the entrance of the spectrometer. This slit was opened with help of a micrometer screw during calibration until a line resolution of 8.5 nm (FWHM) was reached. To ensure, that all photons were emitted from a target region with adequate focus, the slit was mounted in horizontal direction. In vertical direction on the other hand, small variations in the bias of the target ladder could have resulted in recorded regions out of the optical focus, so that such an alignment was refused.

On the output of the spectrometer ("Focal Plane" in figure 4.7a) a *PCO 1600* camera (12.2 mm × 9.0 mm CCD sensor size, 14 bit resolution, monochrome mode) was mounted with help of a C-mount adapter plate. The plate reduces the wavelength range to 600 nm and the visible range starts at 217 or 230 nm, depending on the orientation of the plate during mounting. The camera alignment on the output was chosen such, that the recorded emission spectrum was projected on the longer axis of the recorded images. The beam profile was meanwhile projected on the smaller axis of the recorded images.

In front of the spectrometer two lenses were used during beam times:

- Linos MeVis Inspec with 50 mm focal length

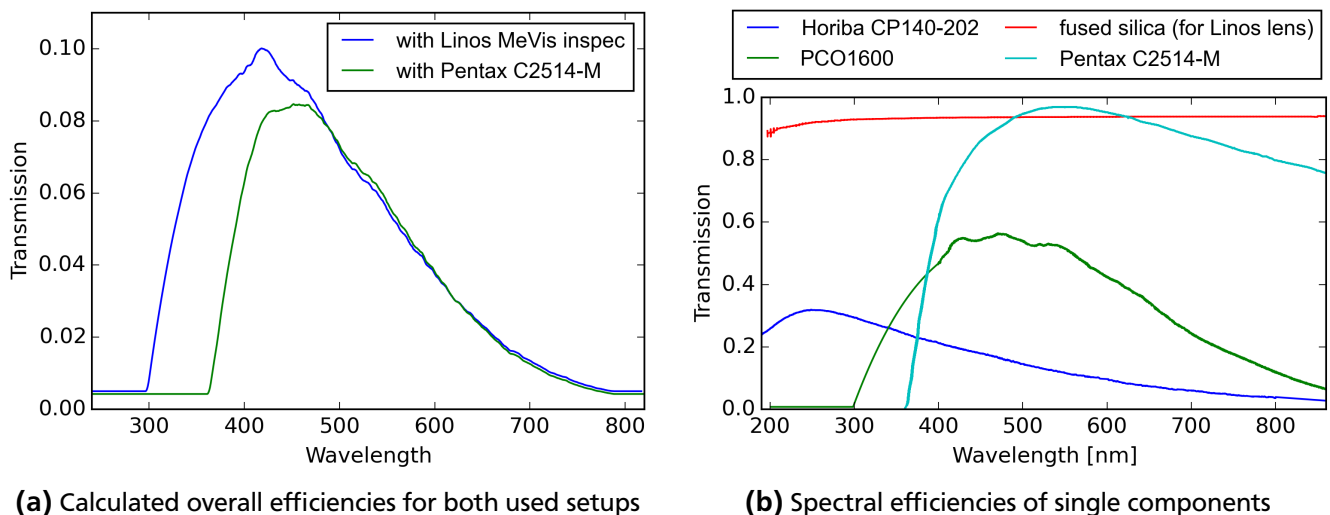- Pentax C2514-M with 25 mm focal length

(a) Calculated overall efficiencies for both used setups

(b) Spectral efficiencies of single components

Figure 4.8: Transmission efficiencies as function of wavelength for the spectrometric setup.

The glass materials of the used lenses have different transmission coefficients as a function of wavelength. For both setups the spectral efficiency of the complete system, including lens, spectrometer and camera, was calculated and the functions are plotted for the Linos and Pentax setup in figure 4.8a. The

transmission efficiencies of the single components that were used for calculations are plotted in figure 4.8b). For the PCO1600, the spectral efficiency was taken from the datasheet of the supplier and extrapolated[3] for the range of $\lambda < 400$ nm.

The camera system for spectrometry ("camera #2") was triggered with the same timing signals for scintillation and background record as the system "camera #1". The values for set exposure times are given in tables 4.2a and 4.2b.

4.3 Data Acquisition

With both cameras of the described optical setup the ion induced scintillation of each target screen was recorded. During each of the beam times, listed in table 4.1, the targets were moved consecutively into the beam. If the necessary voltage for the iris of camera #1 was not known from previous measurements, a few pulses were used for calibration. Afterwards records of approximately 30-40 pulses were taken, triggered by the GSI Timing System. Another trigger signal, that was sent during beam storage in SIS18, was used to take a background image before each scintillation record. This procedure was repeated for each target screen under irradiation with different beam intensities. The beam intensities were requested in dedicated values, generating a well-arranged representation in a logarithmic plot.

The trigger system of camera #1 was used for camera #2 as well, so that both cameras recorded simultaneously (see figure 4.6d). Only the possible start of record was different between both cameras: Since the iris of both lenses on camera #2 could only be changed manually, it was kept on a fixed value during beam times. Thus, the measurements of spectral emission could start with the first beam pulse. Due to the explained high transmission loss in the spectrometer system and the high bit-size of the chip, an overexposure during measurement was in principle observed. Moreover, the recorded emission was rather low and hardly to observe at all for the irradiation with low-Z projectiles or if the scintillation screen offered a low light output anyways. For these reasons many emission spectra were recorded with high noise level and the emission of the A999 target #6 could not be investigated at all.

The described acquisition method was performed during measurements in fast and slow extraction mode, respectively. For the radiation hardness tests, the trigger system was used as described above, with the difference, that the irradiation of each target was performed for a time span of 45 minutes. In general this duration corresponded to a number of approximately 1000 pulses. After an irradiation break of 15 minutes, the investigated target was moved into the beam for another 5 minutes to check for any permanent variations of the observed emission behavior.

---

[3] find more details in the appendix in listing L.12

5 Data Analysis and Experimental Results

The seven inorganic scintillation screens were irradiated with altogether five different ion types, extracted from SIS18 in fast and slow mode (see chapter 3). The particles experience a stripping at the and of the HTP beam line. Therefore this chapter starts with the presentation of the real particle energies, as determined for the performed beam times by numerical calculation. In the following the data analysis performed after target irradiation (*offline*) is described. The recorded images were normalized to the settings of the optical system and the scintillation response was determined with respect to the light output L, the light yield Y and the induced emission spectra. The horizontal and vertical beam profiles were determined and their statistical moments were calculated. Especially the second statistical moment σ was analyzed as representative factor for horizontal and vertical beam width. Details about selection criteria and the usability of the materials in the FAIR diagnostics system are given in the end.

5.1 Irradiation Parameters after Beam Stripping

At the end of the beam line the ions left the vacuum through a 50 μm thick steel foil, traveling through atmosphere for 72 cm before they reach the scintillation targets. This vacuum window caused a stripping of the beam charge and a loss of beam energy, due to Bohr's stripping criterion [27]. During slow extraction mode the diagnostic chamber with HTPDI1I and HTPDI1S caused additional beam stripping, which is why these detectors were not used during measurements in fast extraction mode. During beam time with protons as projectile the diagnostic chamber was not used either, since the stripping caused a beam loss and no scintillation was observed with inserted diagnostics. Here the beam intensity at HTP was recorded for each requested beam intensity either before or after scintillation record and compared with the measurements of a comparable diagnostic tool is SIS section 9 (SIS09DT_ML). After beam time, the beam loss between SIS18 and HTP was calculated by these measurements and used as factor. This factor and the measured beam intensities from SIS09DT_ML were then included in the data analysis.

For each measurement the specific energies and averaged charge state at the target surface were calculated numerically by use of LISE [113] and are given in tab.3le 5.1 on the next page.

On basis of the corrected beam energies per beam times in table 5.1, the total deposited energy per ion was calculated with LISE [113]. The calculations were performed for each single target specifically, since they differ from each other with respect to the chemical composition, material density and/or screen thickness, as explained in section 3.3. The results are listed in tables 5.2 to 5.5 and were used during analysis to calculate the light yield Y, according to equation (2.6).

Table 5.1: Numeric calculation of beam energy and averaged charge state, calculations done with LISE [113]

	projectile	slow extraction Energy [MeV/u]	$\langle Q \rangle$	fast extraction Energy [MeV/u]	$\langle Q \rangle$
#1	proton	299.24	1.0	200.79	1.0
#2	Nitrogen	297.31	7.0	299.26	7.0
#3 & #3R	Nickel	289.33	28.0	297.07	28.0
#4	Xenon	281.12	53.92	294.85	53.92
#5	Uranium	271.74	90.57	292.23	90.63

Table 5.2: Deposited energies per ion in MeV for P43 phosphor target #1 (supplier: ProxiVision [69]) during performed beamtimes

	projectile	Z	Slow Extraction Beam Energy [MeV/u]	ΔE_{dep}	Fast Extraction Beam Energy [MeV/u]	ΔE_{dep} [MeV]
#1	proton	1	299.24	0.10843	299.79	0.10832
#2	Nitrogen	7	297.31	5.3707	299.26	5.3507
#3	Nickel	28	289.33	88.984	297.07	87.785
#4	Xenon	54	281.12	340.24	294.85	332.43
#5	Uranium	92	271.74	985.78	292.23	956.38

Table 5.3: Deposited energies in P46 phosphor targets per ion in MeV for performed beam times

(a) P46 phosphor target #2 (supplier: ProxiVision [69])

	projectile	Z	Slow Extraction Beam Energy [MeV/u]	ΔE_{dep} [MeV]	Fast Extraction Beam Energy [MeV/u]	ΔE_{dep} [MeV]
#1	proton	1	299.24	0.084764	299.79	0.084673
#2	Nitrogen	7	297.31	4.1942	299.26	4.1783
#3	Nickel	28	289.33	69.286	297.07	68.335
#4	Xenon	54	281.12	264.15	294.85	257.92
#5	Uranium	92	271.74	763.61	292.23	740.61

(b) P46 phosphor target #3 (supplier: Crytur [80])

	projectile	Z	Slow Extraction Beam Energy [MeV/u]	ΔE_{dep} [MeV]	Fast Extraction Beam Energy [MeV/u]	ΔE_{dep} [MeV]
#1	proton	1	299.24	0.16954	299.79	0.16936
#2	Nitrogen	7	297.31	8.3909	299.26	8.3590
#3	Nickel	28	289.33	138.74	297.07	136.82
#4	Xenon	54	281.12	529.28	294.85	516.78
#5	Uranium	92	271.74	1531.1	292.23	1483.5

Table 5.4: Deposited energies in $Y_3Al_5O_{12}$:Ce targets per ion in MeV for performed beam times

(a) YAG:Ce single crystal target #4 (supplier: Crytur [80])

	projectile	Z	Slow Extraction		Fast Extraction	
			Beam Energy [MeV/u]	ΔE_{dep} [MeV]	Beam Energy [MeV/u]	ΔE_{dep} [MeV]
#1	proton	1	299.24	0.42583	299.79	0.42537
#2	Nitrogen	7	297.31	21.088	299.26	21.008
#3	Nickel	28	289.33	349.64	297.07	344.72
#4	Xenon	54	281.12	1337.3	294.85	1304.5
#5	Uranium	92	271.74	3876.0	292.23	3751.7

(b) YAG:Ce single crystal target #5 (supplier: SaintGobain [81])

	projectile	Z	Slow Extraction		Fast Extraction	
			Beam Energy [MeV/u]	ΔE_{dep} [MeV]	Beam Energy [MeV/u]	ΔE_{dep} [MeV]
#1	proton	1	299.24	1.698	299.79	1.6961
#2	Nitrogen	7	297.31	84.349	299.26	84.030
#3	Nickel	28	289.33	1417.6	297.07	1396.1
#4	Xenon	54	281.12	5503.3	294.85	5352.3
#5	Uranium	92	271.74	16172.0	292.23	15555.0

Table 5.5: Deposited energies in Aluminum Oxide Ceramic targets (supplier: BCE [92]) per ion in MeV for performed beam times

(a) A999 target #6

	projectile	Z	Slow Extraction		Fast Extraction	
			Beam Energy [MeV/u]	ΔE_{dep} [MeV]	Beam Energy [MeV/u]	ΔE_{dep} [MeV]
#1	proton	1	299.24	1.3006	299.79	1.2992
#2	Nitrogen	7	297.31	64.527	299.26	64.280
#3	Nickel	28	289.33	1078.7	297.07	1062.5
#4	Xenon	54	281.12	4162.5	294.85	4051.2
#5	Uranium	92	271.74	12164.0	292.23	11719.0

(b) Al_2O_3:Cr target #7

	projectile	Z	Slow Extraction		Fast Extraction	
			Beam Energy [MeV/u]	ΔE_{dep} [MeV]	Beam Energy [MeV/u]	ΔE_{dep} [MeV]
#1	proton	1	299.24	1.2312	299.79	1.2298
#2	Nitrogen	7	297.31	61.073	299.26	60.839
#3	Nickel	28	289.33	1020.2	297.07	1004.9
#4	Xenon	54	281.12	3933.4	294.85	3828.8
#5	Uranium	92	271.74	11485.0	292.23	11068.0

5.2 Offline Analysis of Scintillation Response

The images from camera #1 were used to determine the magnitude of ion induced scintillation. The image processing started with background subtraction and the normalization of the images to the recorded beam intensity (in ppp). For correct correlation between beam intensity and scintillation image the timestamps from both records were compared and synchronized by hand. For the following analysis two quantities were distinguished:

First of all the *light output L* was calculated. As explained by equation (2.4) (section 2.2), L corresponds to the number of emitted or recorded photons, respectively, per irradiating pulse. Within the present proceeding L is calculated as the sum of gray scale values λ_i within a defined *ROI* (*Region Of Interest*):

$$L = \sum_i \lambda_i = \sum_{i \in ROI} \lambda_i \qquad (5.1)$$

The calculation of equation (5.1) determines L in arbitrary units. Thus, all values that are derived from L are given in arbitrary units as well. In figure 5.1a an example is given of a recorded and processed image. The red line shows the defined ROI and in the outer plots the horizontal (upper plot) and the vertical projection (right plot) are shown. The projections were calculated as sum of gray scale values perpendicular to the corresponding dimension. This means that the horizontal projection was calculated as sum of gray scale values for each single column, while the vertical projection was calculated as sum of gray scale values for each single row.

During analysis the error ΔL was derived from the noise level and the general degree of damage of the CCD chip in "camera #1", i.e. the number of hot pixels in the background records.

Except for beam time #1 (*protons*) a neutral-density-filter was used to avoid overexposure of the CCD chip. Thus the calculated light output L was divided by the transmission value. Since the filter has a great dynamic with respect to the transmission, as shown in figure 4.6c, the values were recalculated by the recorded emission spectra (see below).

For measurements with varying beam intensities the light output was calculated with (5.1) and then plotted as a function of number of particles per pulse. Generally a linear dependence of the data was observed, so that a linear fit algorithm was used to determine the slope m_L and the error Δm_L, that results from the covariance matrix of the fit algorithm (see explanations in appendix "A.1 Parts of Developed Python 2.7 Source Code"). At the same time the algorithm forced the condition for the data points to intercept the abscissa at zero, so that the influence of readout noise for low beam intensities was minimized (see section "4.2.1 CCD components").

As factor for goodness the *coefficient of determination* R^2 was calculated with help of the means of residuals RSS and the total sum of squares TSS. In common literature R^2 is defined as [114, 115]

$$R^2 = 1 - \frac{RSS}{TSS} \qquad (5.2)$$

For the analysis of each data set an accuracy of minimum $R^2 \geq 95\ \%$ was achieved.
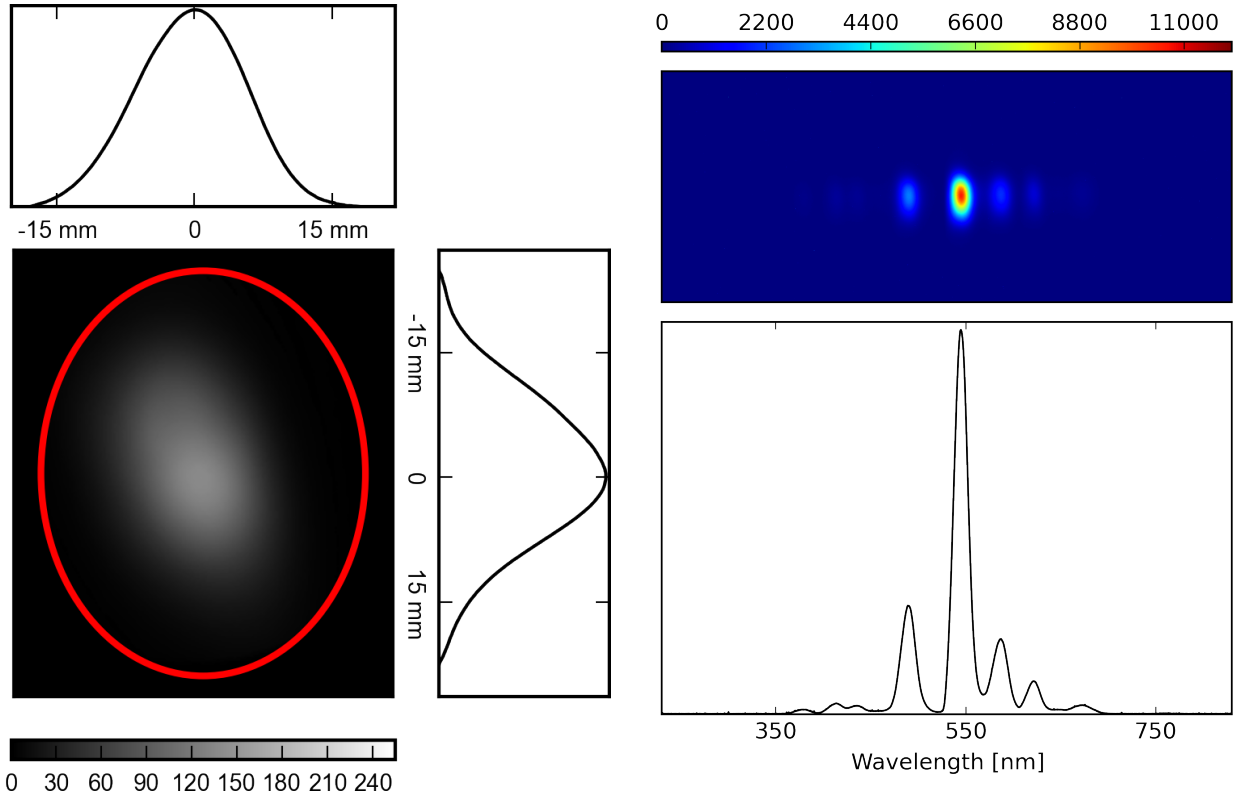
(a) Example of recorded image of "camera #1". The red line represents the ROI, the horizontal and vertical profile distributions are shown in the upper and right plot.

(b) Example of recorded image of "camera #2". The upper picture shows the recorded scintillation (in false color, for better visibility), the lower plot shows the corresponding horizontal projection.

Figure 5.1: Example of scintillation records during image processing, background was already subtracted. Both images were recorded during irradiation of P43 phosphor #1 with slow extracted Uranium (beam time #5).

As second quantity of scintillation response the *light yield Y* was derived. It serves as general quantity to describe the efficiency of a scintillator and is defined as light output L per deposited energy (see equation (2.6)). For the measurement of scintillation caused by a single pulse, Y can be calculated with help of the pulse intensity I_{pulse} in ppp and the previously determined deposited energies $\Delta E \cdot I_{pulse}$ in tables 5.2 to 5.5a:

$$Y = \frac{L}{\Delta E \cdot I_{pulse}[ppp]} \tag{5.3}$$

Equation (5.3) was used during data analysis for the performed radiation hardness tests. Here the error ΔY was calculated by error propagation of ΔL and the appropriate error of the measurement system for particle counting. For the measurements with varying beam intensities, the calculated slope of light output m_L as factor for light output per particle was used to determine Y with:

$$Y = \frac{m_L}{\Delta E_{ion}} \tag{5.4}$$

By using the slope of light output m_L for further calculations, instead of using the light output L itself, the influence of outliers in the data is minimized.

The background subtraction of at camera #2 worked similar to the procedure at camera #1. As explained before, the recorded emission spectra were plotted on the horizontal axis of the CCD chip (see section "4.2.3 Spectrometric system"). To evaluate the wavelength dependent intensity, the horizontal projection was calculated from the image. This projection was folded with the transmission efficiency of the spectral system, as shown in figures 4.8a. An example for recorded and calculated emission spectra is shown in figure 5.1b.

Since the used neutral-density-filter *Hoya ND03* of camera #1 offers a huge transmission dynamic as function of wavelength (see figure 4.6c) deviations from the given standard transmission value of 5 % are supposed, regarding the emission record of each target. Thus, the recorded spectral emission was used to determine the transmission value through the neutral-density-filter *Hoya ND03* of camera #1 for each target after ion beam experiments. For this, the spectral emission of each target was folded with the transmission of the neutral-density-filter (see figure 4.6c) to evaluate the original emission in front of the filter. The transmission values through the *Hoya ND03* were then calculated on hand of the ratio of scintillation (i.e. sum of area under the spectral emission) and are listed in table 5.6. The values were integrated into the analysis of camera #1.

Table 5.6: Transmission values through neutral-density-filter *Hoya ND03* for investigated targets

	target	calculated transmission
#1	P43 (ProxiVision)	4.42442816272 %
#2	P46 (ProxiVision)	2.75168906029 %
#3	P46 (Crytur)	4.90802395757 %
#4	YAG:Ce (Crytur)	4.40539168273 %
#5	YAG:Ce (SaintGobain)	4.41627262443 %
#6	A999 (BCE)	7.76548282107 %
#7	Al_2O_3:Cr (BCE)	10.3383994063 %

A summary of the source code for data analysis is given and explained in the appendix.

5.2.1 Statistical Moments of Profile Distributions

Like in figure 5.1a the two-dimensional response of a target to an irradiating beam can be projected in horizontal (x axis) and vertical direction (y axis). The corresponding profile distributions can be characterized by their location (here: *mean value*) and width (here: *standard deviation*). Additionally the symmetry (also: *skewness*) and curvature (also: *kurtosis*) of the distribution can be investigated. Nevertheless, the two latter factors did not show significant variations during the measurements presented here, which is why they were not investigated closer. In general, all four values are summarized by the definition of *statistical moments*. For any continuous profile distribution they are calculated as reference to a Gaussian distribution (see figure 5.2) [114].

In the following the mathematical description of the first two statistical moments, as used in this thesis, will be described. For completeness the third and forth statistical moment will be given in general form

as well. If not stated otherwise the content was summarized from references [114, 116] and [115]. The equations will be given in form of sum of discrete data points $i = 1, \ldots, N$, as needed for calculations during offline analysis.

The *mean value* can be calculated simply as the average, i.e. the sum over all values x_i divided by the total number of data points N:
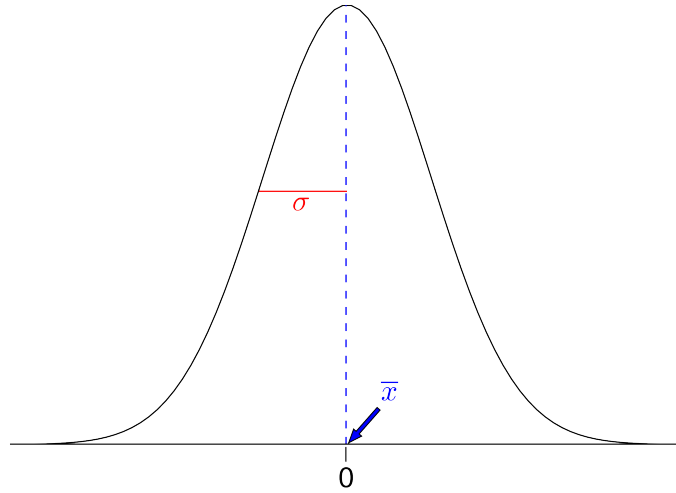
$$\overline{x} = \frac{1}{N} \sum_{i=1}^{N} x_i \qquad (5.5)$$

Figure 5.2: Example of a general Gaussian distribution and the position of the first two statistical moments mean value $\overline{x}$ and standard deviation σ

If the distribution deviates from a constant function and accords for example to a Gaussian distribution, equation (5.5) is expanded by a weighting factor w_i. By this each data point is weighted to its function value with:

$$\overline{x} = \frac{1}{\sum\limits_{i=1}^{N} w_i} \sum_{i=1}^{N} w_i \cdot x_i \qquad (5.6)$$

For a standard Gaussian distribution, as shown in figure 5.2, the mean value coincides with zero ($\overline{x}_{Gauss} = 0.0$).

With the knowledge of (5.6) the *variance* σ^2 is calculated with:

$$\sigma^2 = \frac{1}{N-1} \sum_{i=1}^{N} (x_i - \overline{x})^2 \qquad (5.7)$$

and from this the *standard deviation* as square root of equation (5.7):

$$\sigma = \sqrt{\frac{1}{N-1} \sum_{i=1}^{N} (x_i - \overline{x})^2} \qquad (5.8)$$

In this thesis σ is calculated as a measure for the profile width. Similar to the considerations for equation (5.6) σ needs to be weighted for non-constant distributions and is thus described by:

$$\sigma = \sqrt{\frac{1}{\sum\limits_{i=1}^{N} w_i} \cdot \frac{1}{N-1} \sum\limits_{i=1}^{N} w_i \cdot (x_i - \overline{x})^2} \tag{5.9}$$

The first statistical moment (*mean value $\overline{x}$*) gives the position of the center of mass of the recorded beam. This parameter was kept constant during beam times. In general, variations of the operational alignment were kept as minimal as possible during beam times and due to previous experiments at UNILAC [4–6] focus was set on the second statistical moment σ. For the data analysis, the weighting factor w_i in equation (5.9) corresponds to the profile intensity ψ_i of the position x_i of ith pixel. The sum has to be normalized by the sum of profile intensities and the number of points of the profile distribution N, so that the normalizing factor in the denominator is than $\sum\limits_{i=1}^{N} w_i \cdot (N-1) = \sum\limits_{i=1}^{N} \psi_i \cdot \sum\limits_{i=1}^{N} x_i = L$ and so is equivalent to the light output L. The standard deviation is thus calculated (in horizontal and vertical direction separately) with:

$$\sigma = \frac{1}{L} \cdot \sqrt{\sum\limits_{i=1}^{N} \psi_i \cdot (x_i - \overline{x})^2} \tag{5.10}$$

For completeness the general calculation formula for the *skewness γ* is given with:

$$\gamma = \frac{1}{N} \sum\limits_{i=1}^{N} \left(\frac{x_i - \overline{x}}{\sigma} \right)^3 \tag{5.11}$$

For standard Gaussian distribution the skewness is calculated to $\gamma = 0.0$. The *kurtosis κ* is calculated with:

$$\kappa = \frac{1}{N} \sum\limits_{i=1}^{N} \left(\frac{x_i - \overline{x}}{\sigma} \right)^4 - 3.0 \tag{5.12}$$

The subtraction of factor 3.0 in equation (5.12) is necessary by definition to result in a kurtosis of $\kappa = 0.0$ for a standard Gaussian distribution.

The recorded images from camera #1 were used for calculation of statistical moments. As described in section 4.2.2 the tilting of the screens and the camera resulted in a deformation of the recorded scintillation image. Thus, the vertical axis of the images was compressed by the appropriate angle and the resulting beam profiles were compared with reference grids in the beam line[1]. From these profile distributions the statistical moments were calculated as given in equations (5.6) to (5.12).

As a reference, two MWPCs were used to measure the beam profiles of fast and slow extracted beam pulses, respectively. Both are built of a number of wires (range of 100 ± 50) in horizontal and ver-

---

[1]   The position of the grid is marked in figure 4.1b

tical direction. The spacing is in the range of $0.5 - 5.0$ mm and is increasing from the middle to the periphery [57, 58].

5.3 Variation of the Beam Intensity

The images that were recorded during beam times with different beam intensities in fast and in slow extraction mode (see table 4.1, page 39) were analyzed as described in the previous section. The calculated results are presented in the next sections with respect to the light output L and the light yield Y. The calculation of statistical moments did not offer significant variations during beam times, which is why the calculated profiles of the target response to the irradiating beam (Beam Profile) are discussed in section 5.3.3. Last but not least, the emitted optical spectra are presented for the phosphor and single crystal targets qualitatively in 5.3.4. Here as well, no fundamental changes were observed, neither during variation of beam intensity nor compared to references from literature.

5.3.1 Light Output L

Figure 5.3 shows the integrated light output L of all investigated target screens as function of number of particles per pulse. The scintillation was induced by the fast extracted Uranium beam #5 and the beam intensity was varied between $3 \cdot 10^6$ and 10^8 ppp (see table 4.1). The error bars for L are in the range of 5-20 %. For the beam intensities the error bars correspond to 15 %. The bars seem to increase nonuniformly, but this observation has two origins: On the one hand the error ΔL was estimated on basis of the degree of overexposure during measurement. During fixed iris setting this factor was indeed increasing in dependence of number of particles since the mean signal of the recorded images fluctuated with the real beam intensity of the requested pulses. This leads to an increased light exposure on the chip for pulses above the averaged beam intensity and thus to an increase of the error ΔL.

On the other hand the logarithmic scaling on both axes leads to an asymmetric illustration of the errors. This falsification can irritate the reader, but was accepted for the benefit of a clear data representation.

Under the given measurement conditions all target materials respond linear to the number of particles per pulse. A saturation effect as predicted for ionization by single particle (see sections 2.4.1 and 2.4.2) or by multiple particles (section 2.4.4) could not be observed.

The measurements offer different slopes m_L of the investigated targets for equal beam conditions. The highest slope is observed for the Ce-doped YAG single crystal #5 (supplied from SaintGobain). This screen has a thickness of approximately 1 mm so that a large energy deposition ΔE_{ion} per ion is resulting, which is declared as reason for the observed high light output. Nevertheless, the large energy deposition ΔE_{ion} should lead to an increased material damage and so to a higher propability for quenching as well. This observation failed to appear and the target reacted linearly to the ion irradiation during each beam setting. Another explanation for the high light output is given by the transparency ot target #5, which is higher than the phosphor targets with same chemical composition. The general transparency should facilitate the transmission of photons, generated at the bottom of the target, up to the target surface, so that they are recorded by the system as well.

In the group of the phosphor screens the P43 phosphor shows the highest light output. Regarding the Bethe-Bloch equation (2.1) the high material density of $\rho_{P43} = 7.21 \frac{\text{g}}{\text{cm}^3}$ is responsible for a high value
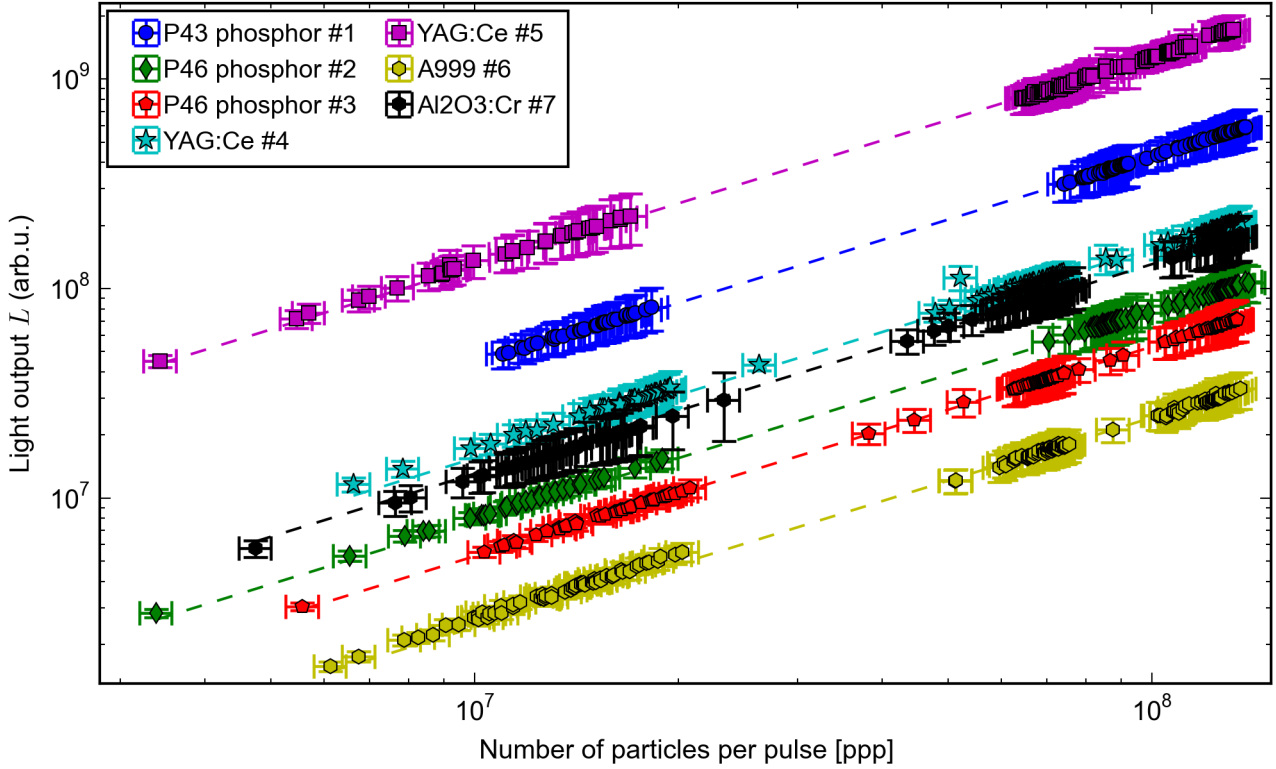
Figure 5.3: Light output L of investigated targets induced by fast extracted Uranium beam

of deposited energy E_{dep}. The high light ouput already gives an evidence, that Gd_2O_2S:Tb inherits a high scintillation efficiency T (see equation (2.3), page 16) or low energy gap E_g or both. A high scintillation efficiency of P43 phosphor, compared to other phosphor screens like e.g. P46, was already observed for X-ray imaging in [117, 118].

Furthermore, figure 5.3 gives a comparison between the light output of A999 #6 and Cr-doped Aluminum Oxide ceramic #7: The pure Aluminum Oxide shows the lowest light output while Chromium-doping induces a factor of ≈ 5 more light. This factor was observed in all beam times. As explained in section 2.2, the dopant makes the scintillation process more efficient due to the possibility of 4f transitions.

The calculated slopes m_L for investigations with fast Uranium beam #5 are listed in table 5.7. The error Δm_L was determined with help of a python module the covariance matrix. R^2 denotes the coefficient of determination as defined by equation (5.2).

Table 5.7: Calculated slopes m_L for measurements with fast extracted Uranium beam (see figure 5.3)

	target	$m_L \pm \Delta m_L$	R^2
#1	P43	4.27 ± 0.093 (2.18 %)	84.20 %
#2	P46	0.778 ± 0.021 (2.65 %)	85.17 %
#3	P46	0.532 ± 0.013 (2.45 %)	86.20 %
#4	YAG:Ce	1.55 ± 0.032 (2.08 %)	90.00 %
#5	YAG:Ce	12.7 ± 0.21 (1.69 %)	89.74 %
#6	A999	0.241 ± 0.0053 (2.20 %)	90.77 %
#7	Al2O3:Cr	1.31 ± 0.038 (2.90 %)	85.71 %
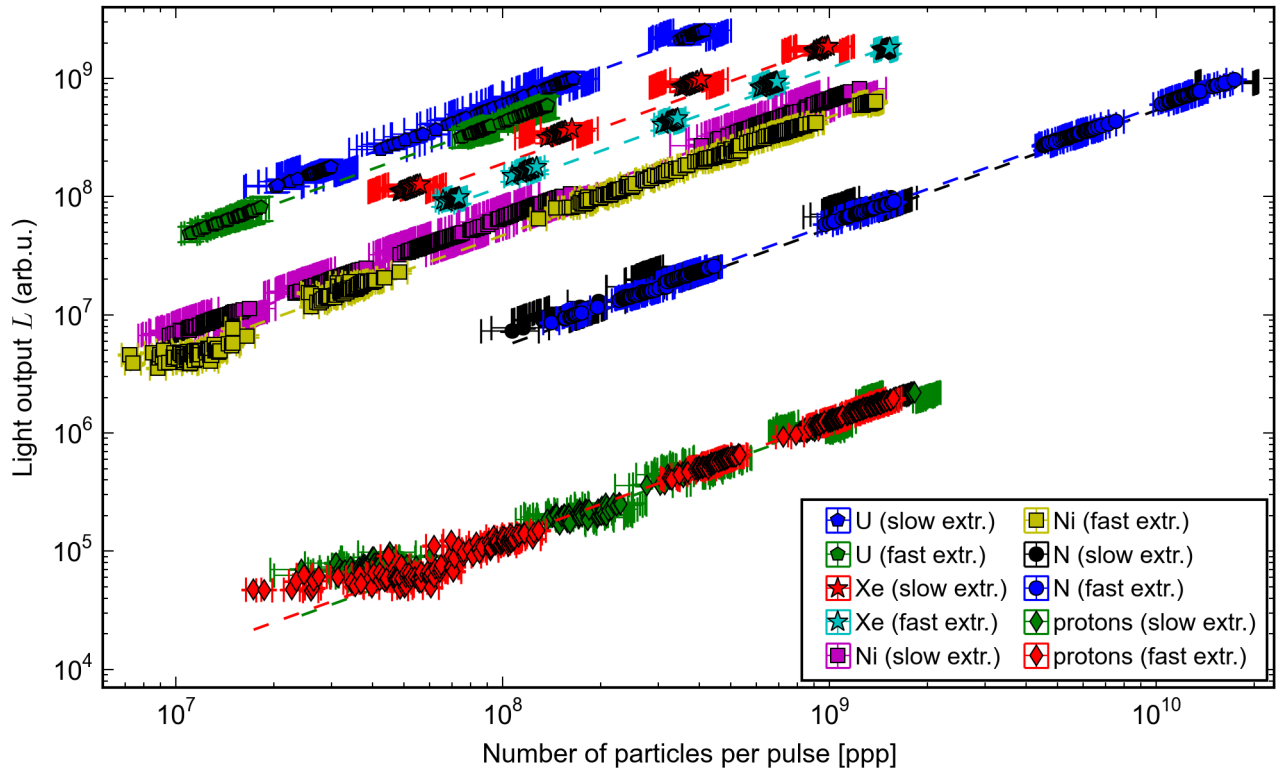
Figure 5.4: Light output L of P43 phosphor screen #1 induced by all investigated projectiles in slow and fast extraction mode

Regarding all investigated projectiles, the irradiation of the investigated materials show similar behavior to the one, shown in figure 5.3. A linear response of scintillation light was observed for all targets and for the irradiation with each investigated projectile, independent if extracted in fast or slow mode. The results of beam times with other projectiles differ from the results in figure 5.3 by the absolute amplitude of light output, but show a similar characteristic as function of particles per pulse.

To check the different behavior of light output between irradiation with slow and fast extracted beams, figure 5.4 shows the light output L for P43 phosphor #1 under irradiation with all investigated projectiles in slow and fast extraction mode. Here the error bars for the beam intensities correspond to 15 % while the errors ΔL are in the range of 5 and 25 %. As result from the camera exchange the errors for uranium and xenon beam time appear smaller. The other beam times were recorded with an old camera, that had already a high number of defect pixels and thus a higher recording error.

All projectiles were requested with the same energy per nucleon under slow and fast extraction mode, respectively. As explained in section 5.1 the beam is stripped differently during slow and fast extraction measurements. The beam energy at target surface and the deposited energy in the P43 phosphor target were calculated numerically with help of LISE [113] and are listed in table 5.2 (page 54). Table 5.8 shows the calculated slopes for figure 5.4.

As observed additionally in figure 5.4 protons induce the lowest light output, so that displacement of the neutral density filter was necessary to observe the luminescence at an adequate signal-to-noise ratio. No significant difference was measured between the light outputs, induced by irradiation with slow and fast extracted beams. However, with increasing atomic number Z of the irradiating projectile more

Table 5.8: Calculated slopes m_L of light output as a function of the ppp for P43 phosphor #1. Δm was calculated by help of covariance matrix. The coefficient of determination R^2 (eq. (5.2)) is given in brackets.

projectile	$m_{L,slow} \pm \Delta m_{L,slow}$ (R^2)	$m_{L,fast} \pm \Delta m_{L,fast}$ (R^2)	ratio $\frac{m_{L,slow}}{m_{L,fast}}$
proton ($Z = 1$)	$(1.2 \pm 0.3) \cdot 10^{-3}$ (91.29 %)	$(1.3 \pm 0.1) \cdot 10^{-3}$ (99.26 %)	0.92
Nitrogen ($Z = 7$)	$(5.3 \pm 0.02) \cdot 10^{-2}$ (94.99 %)	$(5.8 \pm 0.04) \cdot 10^{-2}$ (99.44 %)	0.91
Nickel ($Z = 28$)	0.637 ± 0.012 (94.05 %)	0.469 ± 0.0027 (99.25 %)	1.36
Xenon ($Z = 54$)	1.89 ± 0.069 (88.20 %)	1.21 ± 0.023 (96.60 %)	1.56
Uranium ($Z = 92$)	5.91 ± 0.23 (89.34 %)	4.28 ± 0.12 (84.51 %)	1.38

light output is induced and the differences of emission characteristics between slow and fast extracted irradiation becomes more obvious.

The observations show that slow extracted beams induce either the same or more scintillation than fast extracted beams of the same beam intensity. However, the difference of the slopes is smaller than one would expect due to the difference of extraction times (ratio of pulse durations: $\sim 10^5$). One seperate measurement series with slow extracted N ions at 500 MeV/u was performed to investigate further in possible quenching effects. These measurements are described in section 6.2.

5.3.2 Light Yield Y

As explained in section 5.2 the light yield Y was calculated by hand of the slopes m_L of light output per beam intensity (equation (5.4)). Since a change of the optical setup was necessary during proton beam time (removal of grey filter, see section 4.2.2), the values were normalized to that calculated light yield induced by Nitrogen. These values showed the highest light yield Y for all investigated targets, so that the other data values can be regarded as fraction of Y_N. The normalized data were used to investigate the dependence of Y on the electronic energy loss $\frac{dE}{dx}$, which was calculated numerically with LISE [113] and is listed in tables 5.9, 5.10 and 5.11. The results are shown in figure 5.5. The values for the light yield of YAG:Ce single crystal #4 during by Nickel beam time could not be analyzed, due to occurring problems during measurements.

Table 5.9: Electronic energy loss $\frac{dE}{dx}$ and relative light yield Y_{rel} for P43 phosphor target #1 (supplier: ProxiVision [69])

	projectile	Z	Slow Extraction		Fast Extraction	
			$\frac{dE}{dx}_{el}$ [MeV/μm]	Y (relative)	$\frac{dE}{dx}_{el}$ [MeV/μm]	Y (relative)
#1	proton	1	1.560e-3	$1.084 \pm 23.4\%$	1.560e-3	$1.069 \pm 16.7\%$
#2	Nitrogen	7	0.0767	$1.0 \pm 23.9\%$	0.0765	$1.0 \pm 16.5\%$
#3	Nickel	28	1.2438	$0.714 \pm 24.4\%$	1.2282	$0.495 \pm 17.4\%$
#4	Xenon	54	4.6702	$0.556 \pm 32.8\%$	4.5661	$0.338 \pm 27.4\%$
#5	Uranium	92	13.4787	$0.598 \pm 35.9\%$	13.0485	$0.414 \pm 37.1\%$

Table 5.10: Electronic energy loss $\frac{dE}{dx}$ and relative light yield Y_{rel} for $Y_3Al_5O_{12}$:Ce targets

(a) P46 phosphor target #2 (supplier: ProxiVision [69])

	projectile	Z	Slow Extraction $\frac{dE}{dx}_{el}$ [MeV/μm]	Y (relative)	Fast Extraction $\frac{dE}{dx}_{el}$ [MeV/μm]	Y (relative)
#1	proton	1	1.218e-3	0.814 ± 23.1%	1.218e-3	0.976 ± 16.5%
#2	Nitrogen	7	0.0599	1.0 ± 23.1%	0.0598	1.0 ± 16.5%
#3	Nickel	28	0.9721	0.883 ± 23.5%	0.9594	0.617 ± 17.1%
#4	Xenon	54	3.6519	0.912 ± 34.6%	3.5674	0.490 ± 29.3%
#5	Uranium	92	10.5462	0.729 ± 35.6%	10.1960	0.506 ± 23.6%

(b) P46 phosphor target #3 (supplier: Crytur [80])

	projectile	Z	Slow Extraction $\frac{dE}{dx}_{el}$ [MeV/μm]	Y (relative)	Fast Extraction $\frac{dE}{dx}_{el}$ [MeV/μm]	Y (relative)
#1	proton	1	1.218e-3	1.491 ± 23.0%	1.218e-3	2.118 ± 16.5%
#2	Nitrogen	7	0.0599	1.0 ± 23.2%	0.0598	1.0 ± 16.6%
#3	Nickel	28	0.9721	0.753 ± 23.5%	0.9594	0.689 ± 17.0%
#4	Xenon	54	3.6519	0.876 ± 33.3%	3.5674	0.581 ± 29.3%
#5	Uranium	92	10.5462	0.572 ± 36.1%	10.1960	0.527 ± 33.5%

(c) YAG:Ce single crystal target #4 (supplier: Crytur [80])

	projectile	Z	Slow Extraction $\frac{dE}{dx}_{el}$ [MeV/μm]	Y (relative)	Fast Extraction $\frac{dE}{dx}_{el}$ [MeV/μm]	Y (relative)
#1	proton	1	1.224e-3	1.243 ± 23.3%	1.224e-3	1.758 ± 16.5%
#2	Nitrogen	7	0.0602	1.0 ± 23.0%	0.0602	1.0 ± 16.5%
#3	Nickel	28	0.9764	12.390 ± 23.1%	0.9636	10.883 ± 16.8%
#4	Xenon	54	3.6679	1.013 ± 28.4%	3.5830	0.553 ± 24.2%
#5	Uranium	92	10.5926	0.746 ± 35.1%	10.2408	0.652 ± 32.0%

(d) YAG:Ce single crystal target #5 (supplier: SaintGobain [81])

	projectile	Z	Slow Extraction $\frac{dE}{dx}_{el}$ [MeV/μm]	Y (relative)	Fast Extraction $\frac{dE}{dx}_{el}$ [MeV/μm]	Y (relative)
#1	proton	1	1.218e-3	1.389 ± 23.7%	1.218e-3	1.715 ± 16.5%
#2	Nitrogen	7	0.0599	1.0 ± 23.5%	0.0598	1.0 ± 16.6%
#3	Nickel	28	0.9721	0.795 ± 23.7%	0.9594	0.358 ± 16.8%
#4	Xenon	54	3.6519	0.726 ± 29.3%	3.5674	0.246 ± 22.8%
#5	Uranium	92	10.5462	0.757 ± 36.0%	10.1960	0.724 ± 33.6%

In the plots the following correlations can be identified:

- Fast extraction mode induces similar or lower light yield Y than slow extraction mode.

- The light yield of the phosphor targets shows a decreasing dependence with increasing electronic energy loss $\frac{dE}{dx}$. The decrease becomes larger for fast extraction mode, starting with measurements with Nitrogen beam. Nevertheless, not all values for proton induced light yield confirm this observation. However, the values were recorded with changes in the optical setup, as explained above, so that deviations from the observed dependence are not regarded as reliable.
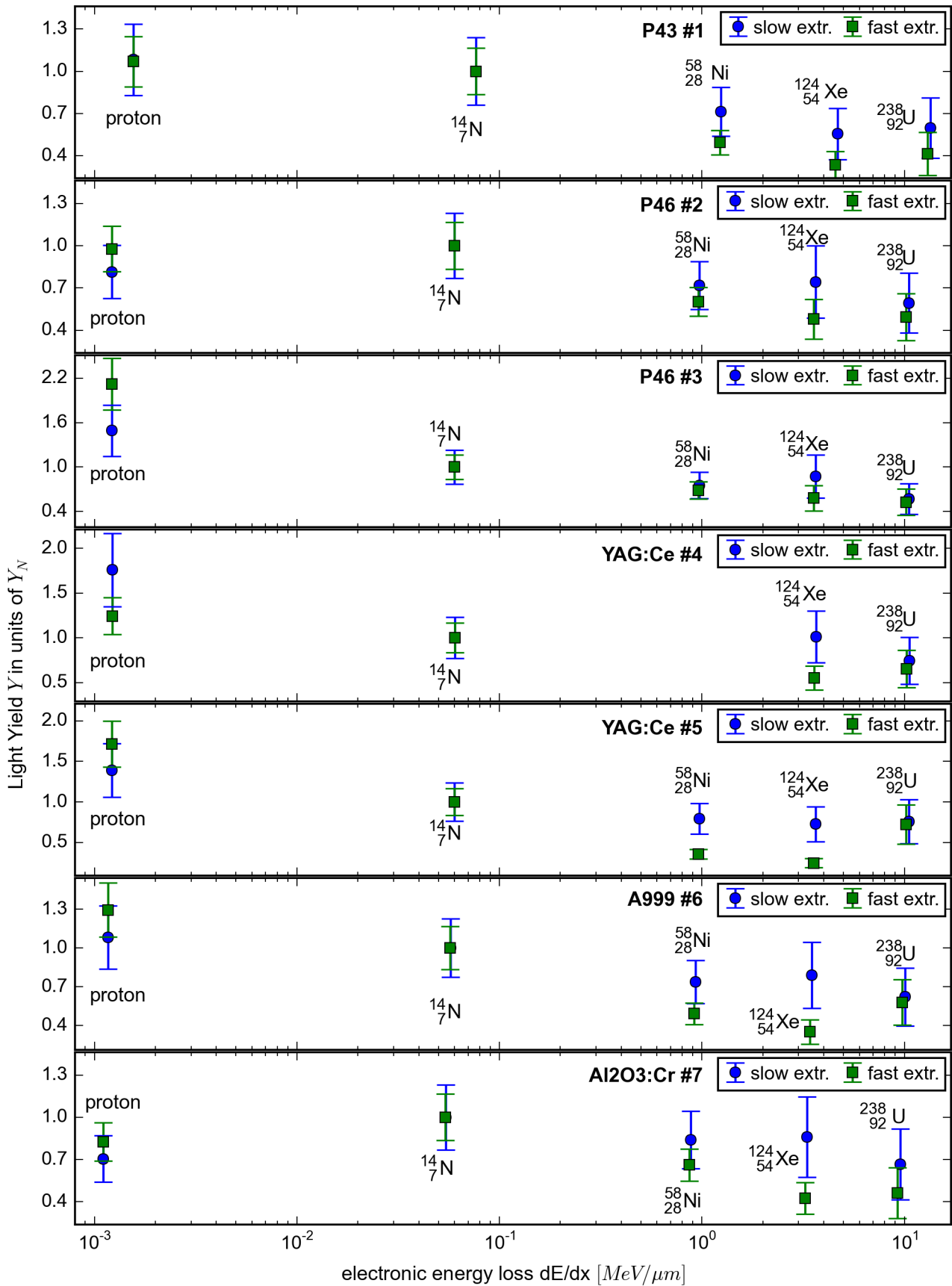
Figure 5.5: Light yield Y of all targets plotted in dependence of the electronic energy loss $\frac{dE}{dx}$ of the investigated projectiles in slow (blue dots) and fast (green squares) extraction mode

Table 5.11: Electronic energy loss $\frac{dE}{dx}$ and relative light yield Y_{rel} for ceramic targets (supplier: BCE [92])

(a) A999 target #6

	projectile	Z	$\frac{dE}{dx}_{el}$ [MeV/μm]	Y (relative)	$\frac{dE}{dx}_{el}$ [MeV/μm]	Y (relative)
			Slow Extraction		**Fast Extraction**	
#1	proton	1	1.165e-3	$1.081 \pm 22.2\%$	1.165e-3	$1.295 \pm 16.2\%$
#2	Nitrogen	7	0.0573	$1.0 \pm 22.5\%$	0.0571	$1.0 \pm 16.5\%$
#3	Nickel	28	0.9295	$0.738 \pm 22.7\%$	0.9172	$0.492 \pm 17.0\%$
#4	Xenon	54	3.4925	$0.790 \pm 33.4\%$	3.4104	$0.350 \pm 27.3\%$
#5	Uranium	92	10.0889	$0.622 \pm 36.1\%$	9.7482	$0.579 \pm 30.3\%$

(b) Al_2O_3:Cr target #7

	projectile	Z	$\frac{dE}{dx}_{el}$ [MeV/μm]	Y (relative)	$\frac{dE}{dx}_{el}$ [MeV/μm]	Y (relative)
			Slow Extraction		**Fast Extraction**	
#1	proton	1	1.103e-3	$0.705 \pm 23.4\%$	1.10e-3	$0.826 \pm 16.6\%$
#2	Nitrogen	7	0.0543	$1.0 \pm 23.1\%$	0.0541	$1.0 \pm 16.4\%$
#3	Nickel	28	0.880	$0.839 \pm 24.2\%$	0.8683	$0.662 \pm 17.2\%$
#4	Xenon	54	3.3064	$0.859 \pm 33.2\%$	3.2287	$0.426 \pm 27.0\%$
#5	Uranium	92	9.5511	$0.666 \pm 37.6\%$	9.2286	$0.464 \pm 39.0\%$

The data in figure 5.5 does not show a constant dependence as function of electronic energy loss. The observed behavior of Y is assigned to the non-proportionality of scintillators (see section 2.4), since the characteristic was already observed: In [10] Menchaca-Rocha compared light yield[2] values of an organic and an inorganic scintillator, respectively, under irradiation with different heavy ions. They developed a numerical model (EDSE mode, see section 2.4.2) and applied it to the data of a plastic scintillator and a Thallium-doped CsI target. The data of the inorganic scintillator was measured by Pârlog et al. [119] under irradiation with different ions from $Z = 5 - 40$ with total kinetic energies up to 1.5 GeV. For this data Menchaca-Rocha was able to calculate a parameter $C(Z)$ as characteristic factor for the amplitude of the light yield. The dependence of C on the atomic number Z showed a decreasing behavior for irradiation with projectiles of $Z \leq 15$, followed by a constant behavior. A similar dependence is observed for the light yield on the electronic energy loss in figure 5.5.

An explanation for the non-proportionality of $C(Z)$ was not formulated by the authors explicitly. Additionally, they gave cause for concern about the accuracy of the mathematical model, by explaining the following: The fit algorithm, applied on the $C(Z)$ data in [10] is weighted much more by the values from irradiation with high-Z projectiles ($Z >> 1$), which corresponds to the region of linear scintillation response. The calculation for lower-Z projectiles and thus the calculated curvature is less accurate, so that the characteristic of $C(Z)$ is compareable with the light yield behaviour in figure 5.5.

---

[2] In [10] the authors use the term *light output*, but their description corresponds to the term *light yield* that is used in this thesis.

5.3.3 Beam Profile

The horizontal and vertical projections of the beam images were analyzed with respect to the second statistical moment σ (see equation (5.9)) to investigate the reproducibility of similar beam images by different materials.

(a) Irradiation with fast extracted Xenon beam with 1×10^9 ppp.

(b) Irradiation with fast extracted Nitrogen beam with 1×10^9 ppp.
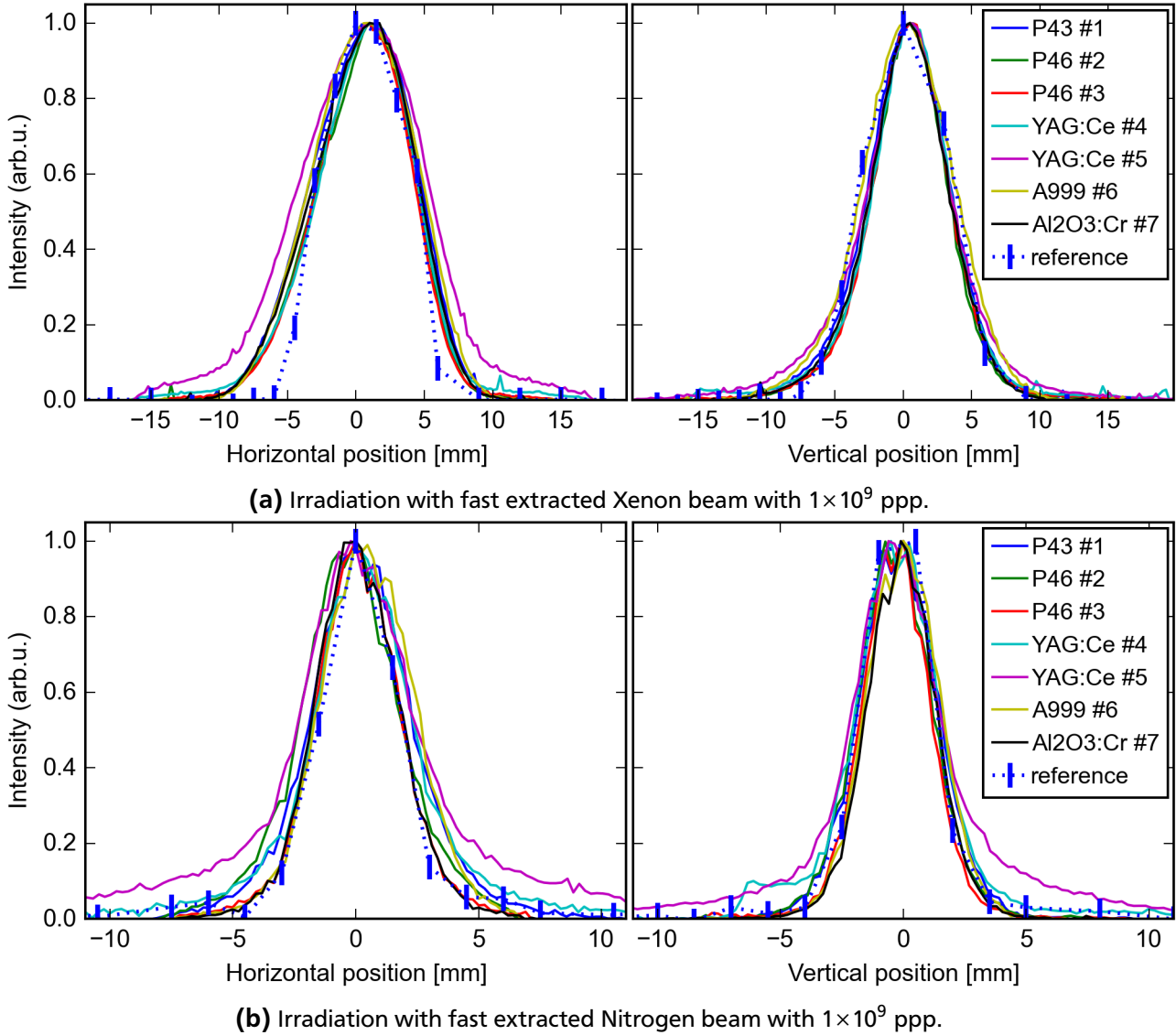
Figure 5.6: Projections of beam profile in horizontal (left) and vertical (right) direction of all investigated scintillation screens, compared with a reference grid.

Figure 5.6 shows a comparison of beam profiles in horizontal (left) and vertical direction (right). The beam profiles during irradiation with a fast extracted Xenon beam with $1 \cdot 10^9$ ppp are shown in figure 5.6a. The dotted blue line shows the measurement with a reference grid, the bars indicate the positions of the grids. In vertical direction, all investigated targets show a good accordance to the reference and lead to a standard deviation of approximately $\sigma_{vert} \approx 3.5 \pm 0.6$ mm. In horizontal direction the profile of YAG:Ce single crystal #5 shows a significant broadening at the basis. This broadening is a general observation for YAG:Ce single crystal #5 and is assigned to the comparatively high screen thickness (≈ 1 mm, see table 3.1) of the target and its transparency. Here induced photons that scatter

transversal through the target are detected by the optics and lead to a deformation of the beam image. The other targets show a calculated standard deviation in the range of $\sigma_{horz} \approx 3.6 \pm 0.4$ mm. In comparison, the measurement with the reference grid results in a more or less mathematical value or the standard deviations of $\sigma_{vert,grid} = 12.7$ mm and $\sigma_{horz,grid} = 9.2$ mm. The reason for the overestimation is assumed by the observed high noise level on the outer wire grids. Since the standard variation is calculated proportional to the position x_i of a value ψ (see equation 5.10), the values from the outer grid wires are weighted stronger and result in an overestimated standard variation. Additionally, some wires around horizontal position $x_i = 10$ mm were defect during measurement, which is why the beam profile was shown highly distorted.

For P43 phosphor #1 the calculated standard deviations σ_{horz} and σ_{vert} are plotted as function of numbers of particles per pulse in figure 5.7 for measurements with fast extracted Xenon beam. As shown in the plot, the variation with increasing beam intensity is negligible. Any changes in the calculated beam widths are assigned to fluctuations in operational beam conditions.
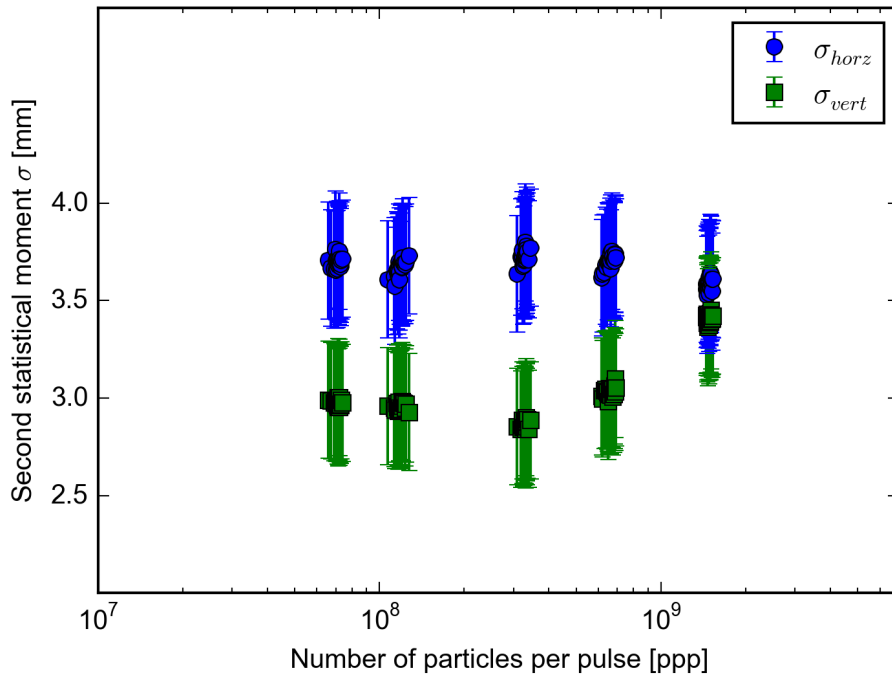
Figure 5.7: Horizontal (σ_{horz}) and vertical (σ_{vert}) beam width as a function of number of particles per pulse, calculated for measurements with P43 phosphor screen irradiated by fast extracted Xenon beam.

Figure 5.6b shows the beam profiles, induced by a fast extracted Nitrogen beam pulse with $1 \cdot 10^9$ particles. The profile increase at the basis of YAG:Ce single crystal #5 is observed here in both, in horizontal and vertical direction, with calculated standard deviations of $\sigma_{horz} \approx 4.4$ mm and $\sigma_{vert} \approx 4.0$ mm. Also the beam profile of YAG:Ce single crystal #4 is expanded, compared to the phosphor and ceramic targets, and shows standard deviations of $\sigma_{horz} \approx 3.0$ mm and $\sigma_{vert} \approx 3.0$ mm. However, the other 5 targets show a good accordance to the measurement with the reference grid in the range of measurement accuracy. The calculated standard deviations here are in the range of $\sigma_{horz} \approx 2.0 \pm 0.4$ mm and $\sigma_{vert} \approx 1.6 \pm 0.2$ mm.

5.3.4 Emission Spectra

The emission spectrum of each irradiated target was recorded during the beam time, using the equipment described in 4.2. Figure 5.8 shows a comparison of the emission spectra of targets #2 - #5, which were all produced of Cerium-doped $Y_3Al_5O_{12}$. The emissions were recorded during irradiation with a slow extracted Uranium beam and averaged over beam intensities between 10^8 and 10^9 ppp. The characteristic emission band in the yellow-green region ($\lambda = 500 - 700$ nm) was clearly recorded. As explained in section 3.3 this emission band is resulting from the 5d to 4f transition. In comparison the emission of the four targets shows no major difference.
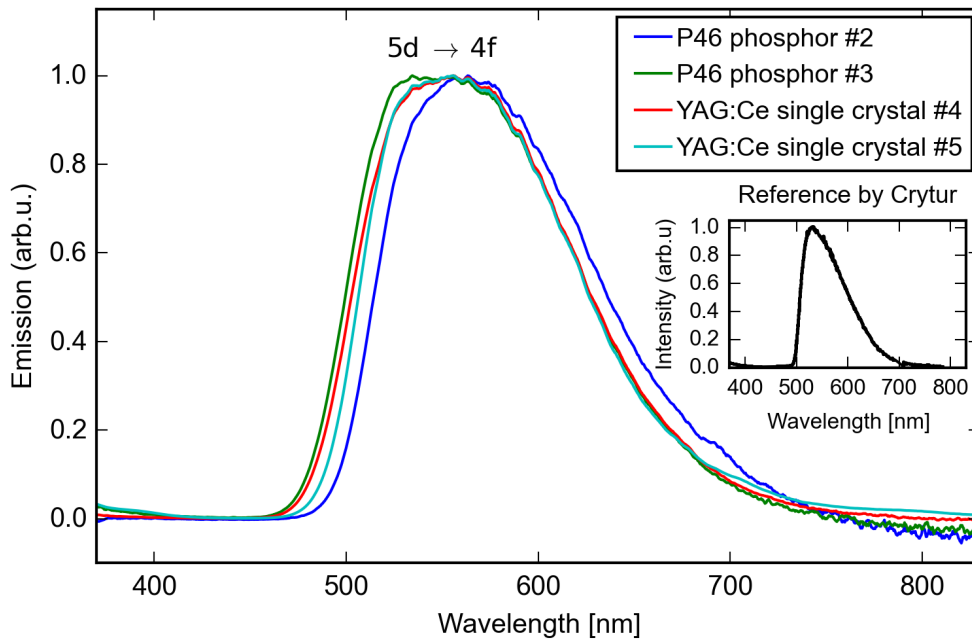
Figure 5.8: Comparison of spectral emission of $Y_3Al_5O_{12}$:Ce materials during irradiation with slow extracted Uranium

Only a slight red-shift is observed in figure 5.8 for the emission spectrum of P46 phosphor #2. This happened similarly during all performed beam times. The red-shift of P46 phosphor #2 is visible in the recorded emission spectra of all beam times. Figure 5.9 serves as prove for the observation. In order to prove that the record was equal for both extraction modes the figure shows the recorded spectra of the target under irradiation with all fast extracted ion beams. The measurements in slow extraction mode showed the same spectra. A possible reason for the red-shift is that the doping of this specific target has a higher amount of Ce^{4+} ions in comparison to Ce^{3+} ions. While Ce^{3+} usually does not change the color of the matrix material, it was observed already in liquid solutions that Ce^{4+} ions can change the color to orange-yellow (wavelength region $\approx$590 nm) [120]. This difference in the color is already visible by the eye, as can be seen in the photographs of the investigated targets in figure 3.7.

In figure 5.9 the spectral emission induced by Nitrogen shows a deficit in the IR region, following the expectation (see 5.3.1) of a low light output induced by nitrogen. The magenta line was added to show the spectral emission for the target, measured by supplier ProxiVision [69]. The reference in the data sheet of ProxiVision is given with a low signal, so that the spectrum is only visible in the region between

$\lambda \approx 500$ nm and $\lambda \approx 620$ nm. Since the emission of the target decreases generally in the IR direction, the emission up to 700 nm or even 800 nm is not visible in the plot of the supplier. Nevertheless, the reference was scaled to a maximum value of 1.0 for the purpose of comparison. The magenta line shows that the emission peak value differs between the supplier's reference and the measurements induced by ion irradiation by a value of $\lambda \approx 24$ nm. This shift is another evidence for the influence of the Ce^{4+} doping on the red-shift of the recorded emission spectrum.

Due to the limits of the optical setup the emission band in the UV region is in principle not visible in the recorded spectra. Only the YAG:Ce single crystal #5 shows a slight emission here, because the general light output of the target is several times higher than for the other targets.
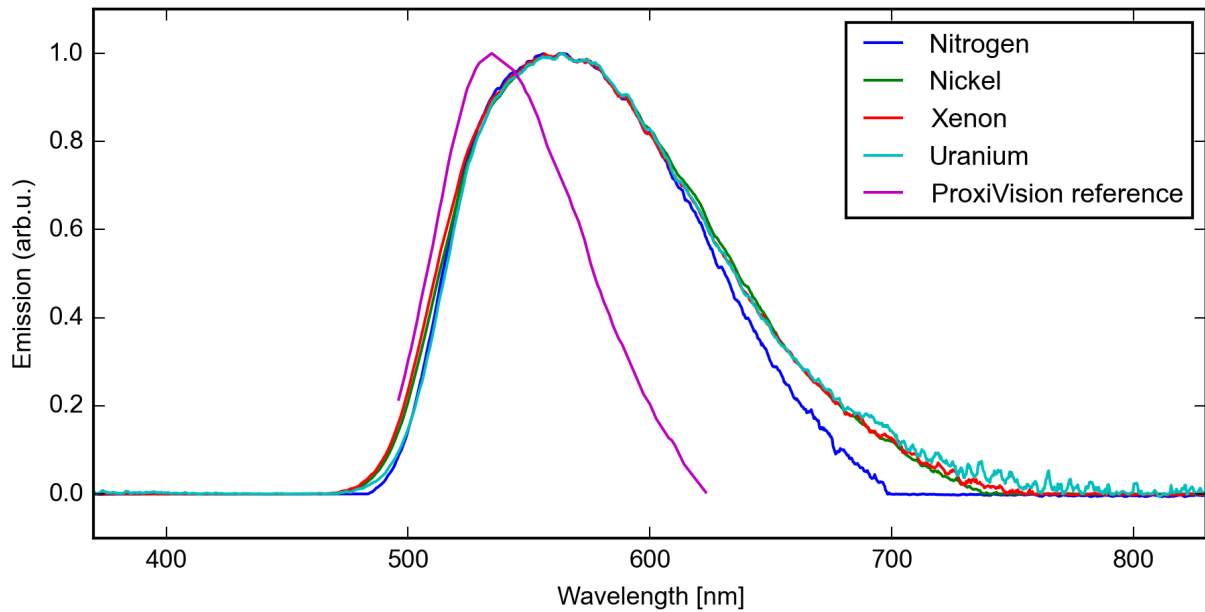
Figure 5.9: Emission spectra of P46 phosphor #2 (from ProxiVision) under irradiation with all investigated projectiles in fast extraction mode. The reference spectra is plotted in pink to show the red-shift of the targets emission.
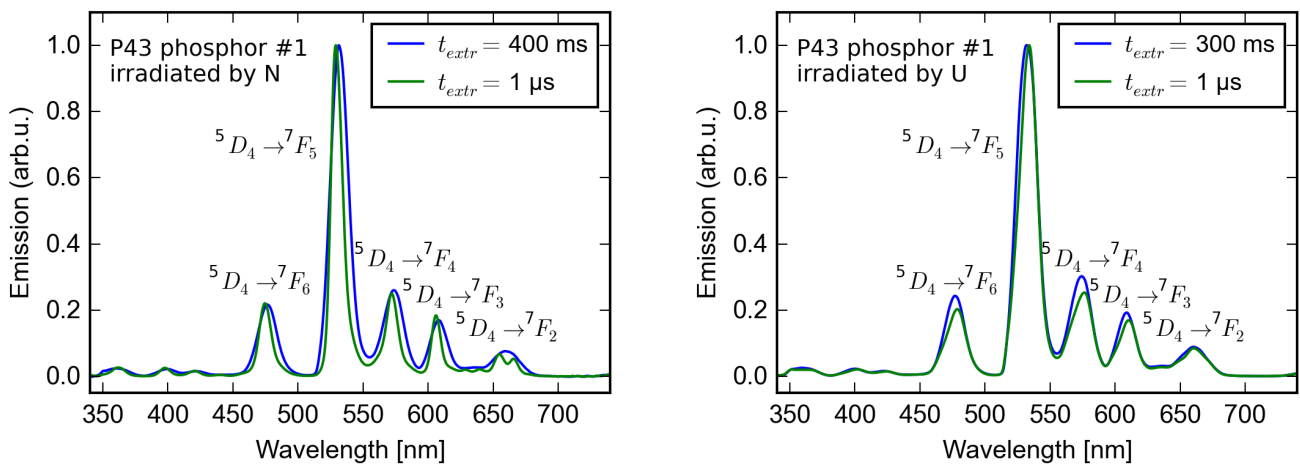
Figure 5.10: Recorded emission spectra of P43 phosphor #1, induced by Nickel (left) and Uranium irradiation (right), pulse extraction times are given by legend.

The emission spectra of P43 phosphor #1, recorded during Nickel beamtime #3 and Uranium beamtime #5, are shown in figure 5.10. For each extraction mode the spectral record was averaged over beam intensities between 10^8 and 10^9 ppp. Differences between the plots are found to be marginal within the accuracy of the given setup. The spectra shown in the figure are almost identical to those presented in literature, e.g. for irradiation with X-rays [65]. In general, the spectral emission of the P43 phosphor #1 did not show any significant variations, so that the references from literature could be verified under the irradiation with heavy ions. A material modification or even a saturation under the given irradiation parameters was not proven.

5.4 Radiation Hardness Tests

The recorded pictures from camera #1 were analyzed as described in section 5.2. Additionally they were divided by the measured number of particles of the incident pulse to give a value of light yield Y per pulse. Figure 5.11 shows the light yield Y in dependence of the accumulated number of particles for the investigated phosphor targets #1 - #3 and the Chromium-doped Aluminum Oxide #7. For the plots the data points were binned to a beam intensity of approximately $5 \cdot 10^{10}$ ppp. The resulting statistic deviations serve as error bars. During the measurement with P46 phosphor #3 fluctuations in the operational alignment occurred after the irradiation break, which led also to a change in beam sizes (see figure 5.12). The deviations from the averaged light yield value led here to significantly increased error bars.

While for both P46 phosphor screens #2 and #3 the light yield is nearly constant or increases only slightly, the measured light yield of P43 phosphor #1 decreases quite linearly down to $\approx$ 96 % of the initial value. Also, the P43 phosphor #1 is the only target, that shows an evidence for target recovery, and starts with the initial value of Y after the beam break. The Chromium-doped Aluminum Oxide shows the largest decrease with $\approx$ 10 % and saturates on this level after an accumulation of 10^{12} ppp. This degree of light yield loss is not observed for the pure Aluminum Oxide target #6, despite of the light yield drop at $2.1 \cdot 10^{12}$ ppp, which was caused by changes in the operational alignment.

In figure 5.12 the calculated second statistical moments σ_{horz} and σ_{vert} are shown. They are presented as function of accumulated particles during radiation hardness test in fast extraction. Similar to the data in figure 5.11 the data were binned to a beam intensity of $5 \cdot 10^{10}$ ppp and the resulting statistic deviations serve as error bars. Here the fluctuations during measurement of P46 phosphor #3 are visible again after irradiation break, resulting in a change of beam size.

Apart from usual fluctuations of beam size during beam operations, σ_{horz} and σ_{vert} do not change significantly for four of the seven targets. For P46 phosphor #3 a significant change of beam size is observed after beam break. This is assigned to fluctuations in operational alignment. The change in beam operations, that was already observed for A999 #6 in 5.11 might coincide with a significant change of emittance. This modification is ignored. As only target, the YAG:Ce single crystal #5 shows a decrease in beam sizes, even though the reference grid did not reveal a change in beam parameters. Here, the high amount of energy deposition in target YAG:Ce #5 is held responsible, as already discussed in the former sections. This means, that number of induced local defects in the material must have been higher than local charge carriers could have healed by a diffusion process. Another evidence for local defects is given by the light yield of the target that showed a slight decrease in contrast to the other $Y_3Al_5O_{12}$:Ce targets (see figure 5.11).

A nearly identical behavior of all screens can be found in the recorded emission spectra as well. Figure 5.13a shows the spectral record for P43 phosphor #1 and YAG:Ce single crystal #4. In order to present a better overview, the spectra of both targets are shown in four dedicated steps of accumulated particles. Both figures originate from measurements in slow extraction mode, because these measurements lead to a better signal-to-noise-ratio. In the figure the blue shaded spectra illustrate three emissions during long time irradiation period, while the red shaded spectra were recorded after beam break. A significant change in the characteristic that would lead to an occurring material modi-

fication can not be proven. Also during measurements with the other investigated targets a change of emission spectrum was not observed. In fast extraction mode, variations in the spectra could not be proven either and the records present almost identical distributions (see also section 5.3.4).
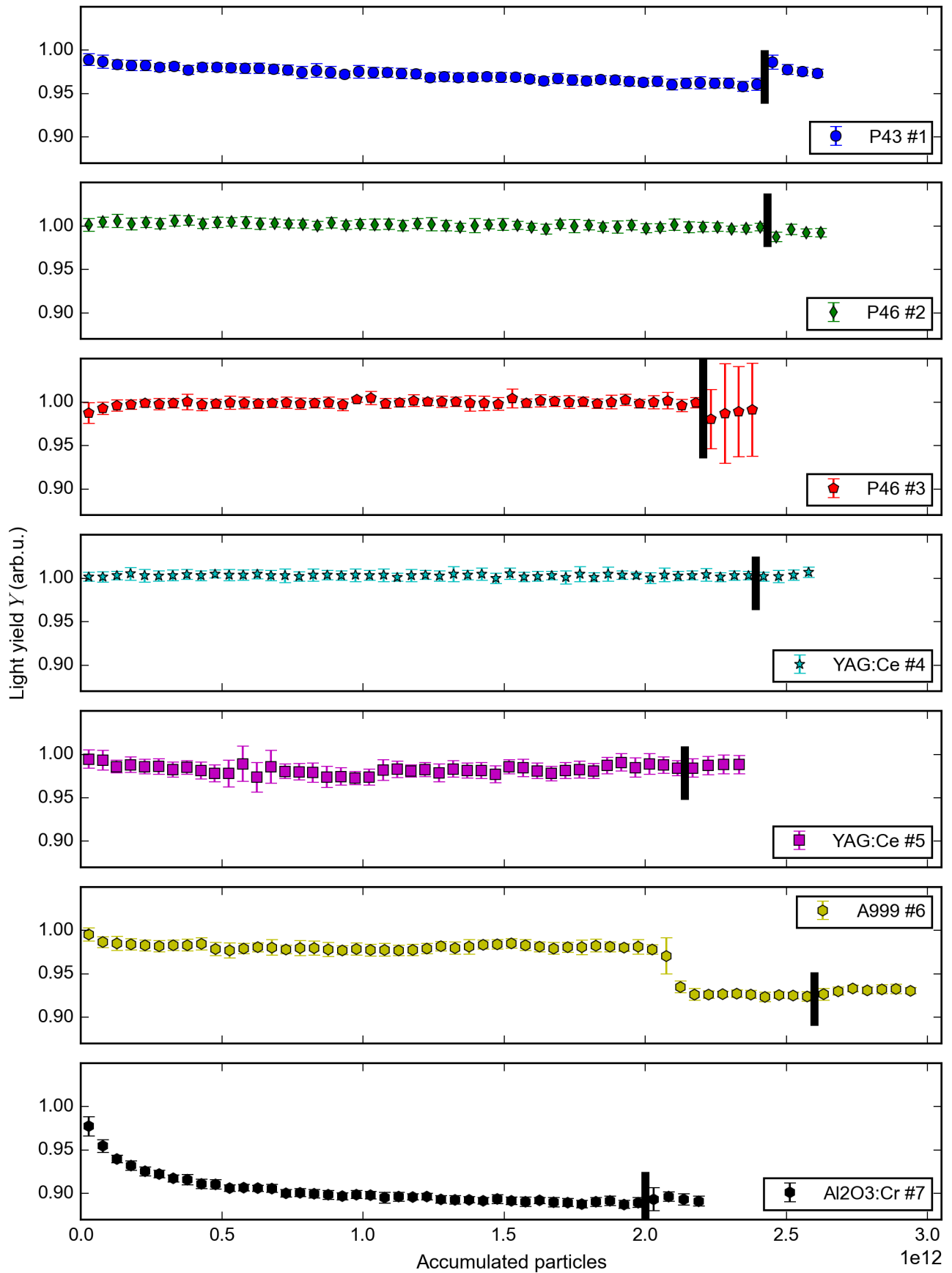
Figure 5.11: Light yield Y during radiation hardness test with fast extracted Nickel beam #3R. The black bar denotes the irradiation break of 15 minutes.
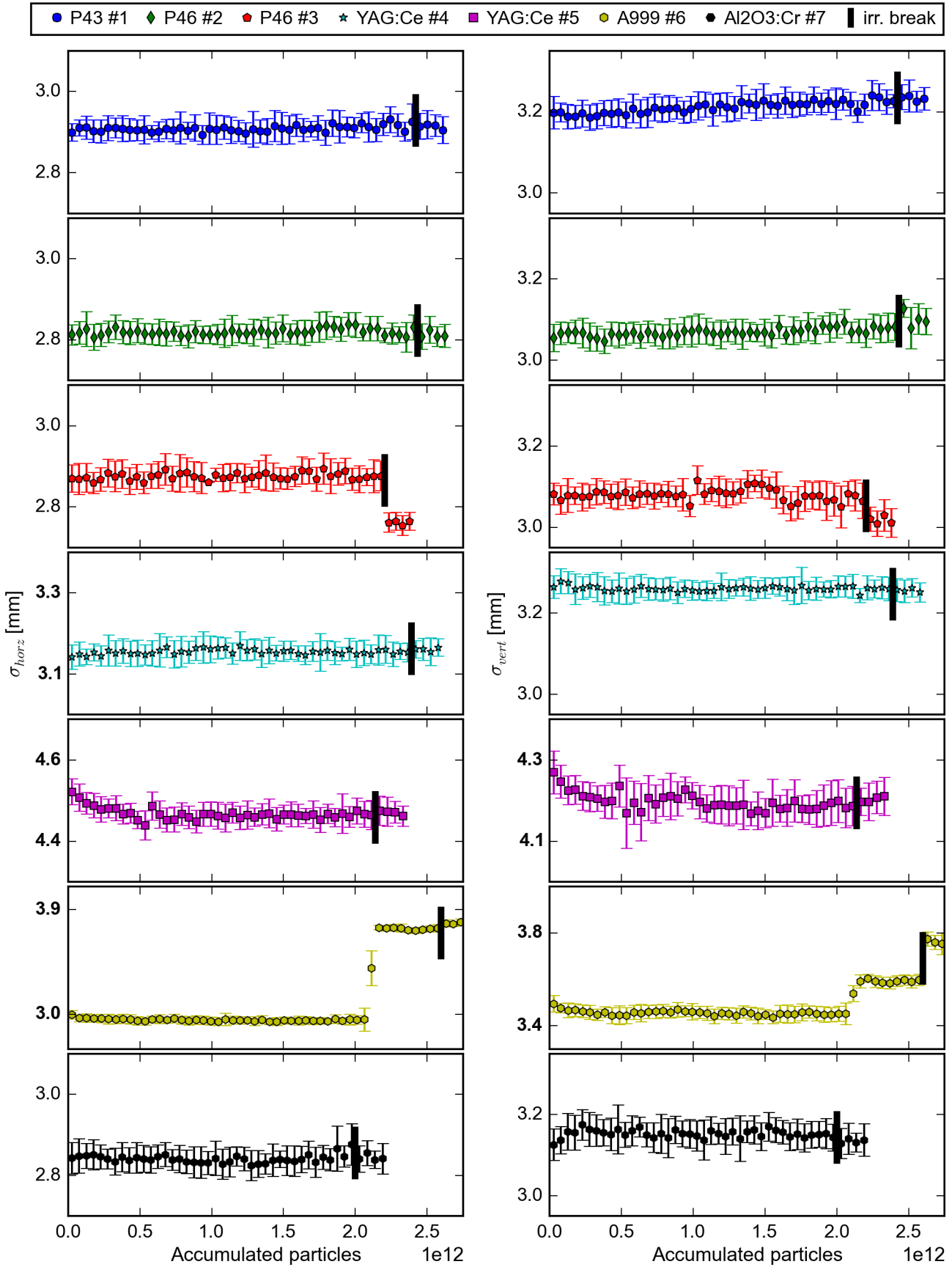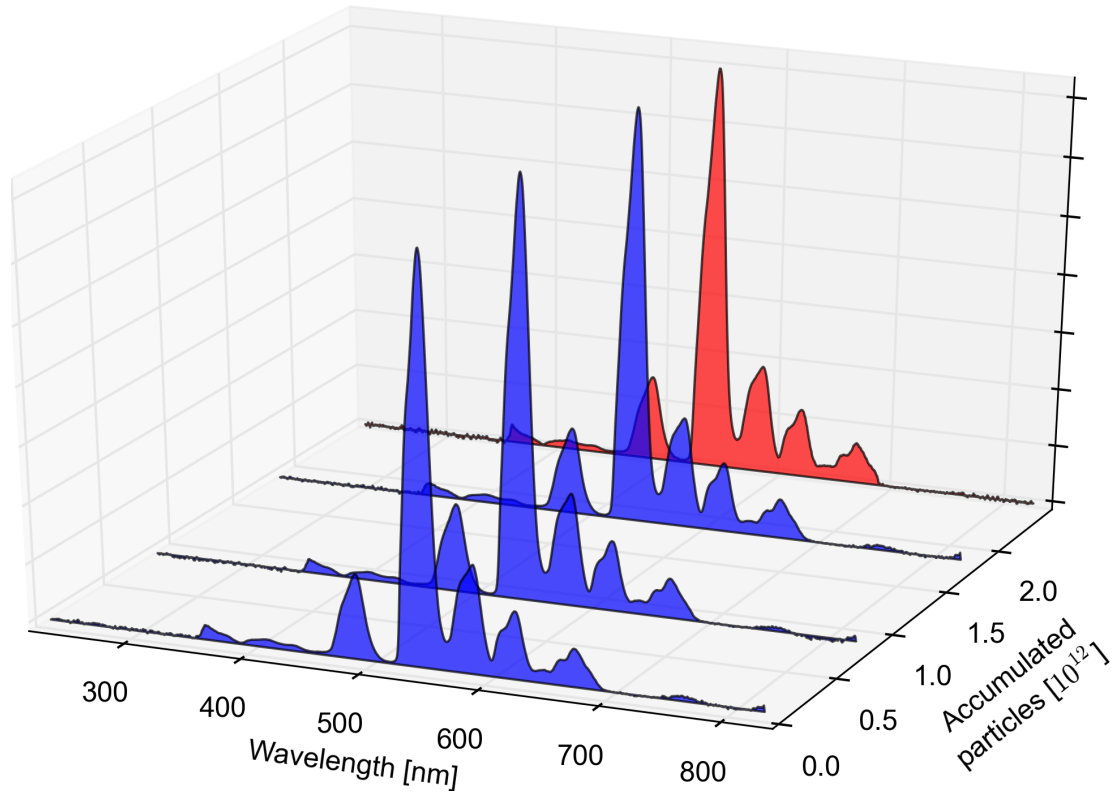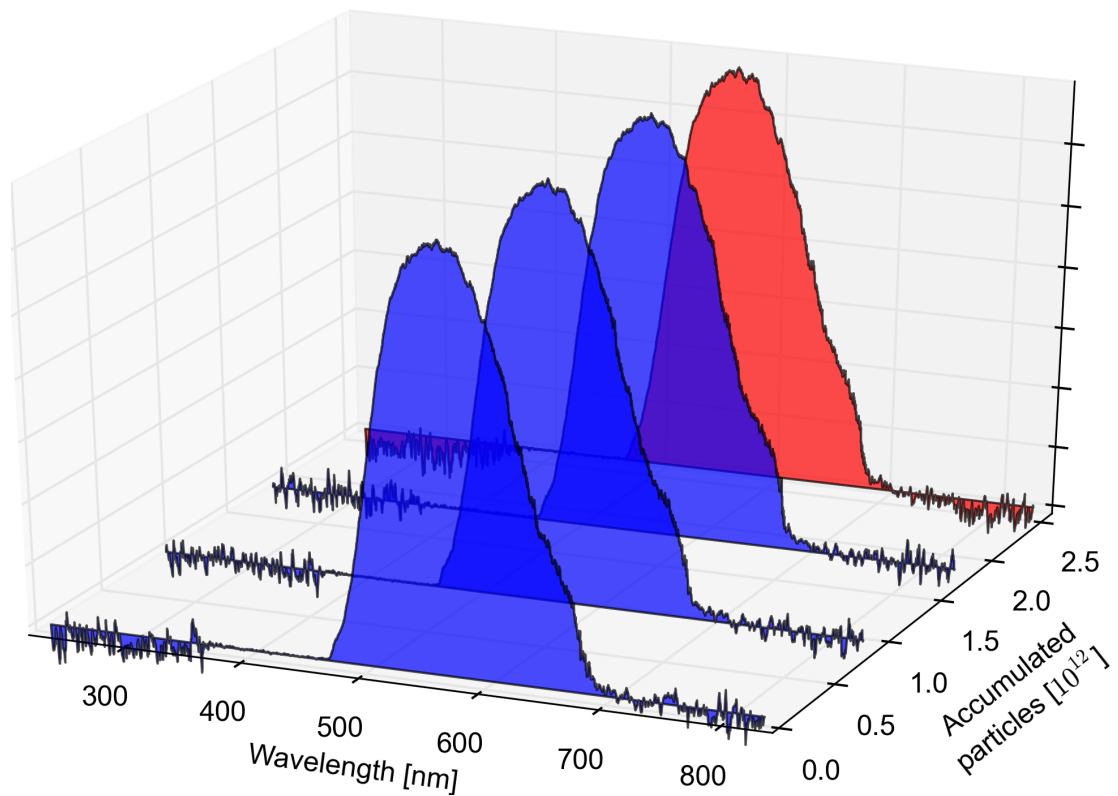
Figure 5.12: Calculated second statistical moments σ_{horz} and σ_{vert} for the accumulated particles in the performed radiation hardness test with fast extracted Nickel beam #3R.

(a) P43 phosphor #1

(b) YAG:Ce single crystal #4

Figure 5.13: Emission spectra during radiation hardness test with slow extracted Nickel #3R at numbers of accumulated particles increasing in four steps.

5.5 Résumé

The seven investigated scintillation targets, containing phosphor screens, single crystals and polycrystalline ceramics, were irradiated by different ions in fast and slow extraction mode, as explained in 4.1.

The offline analysis showed, that all targets answer in a linear light output to all types of irradiated ions at beam intensities between 10^7 and $2 \cdot 10^{10}$ ppp (see fig. 5.3). A small difference in light output of each material was observed between irradiation in fast and slow extraction mode, but the factor is small, compared to the difference in extraction times (see tab. 5.8). No saturation of light output was observed for increasing beam intensity within the range of measurements during the complete project.

In general, the lowest light output was observed for un-doped Aluminum Oxide (A999 #6). A Chromium doping of 0.04 weight percent (Al_2O_3:Cr #7) led to a five times higher light output. Due to the high amount of deposited energy (originated by the target thickness), the highest light output is measured with YAG:Ce single crystal #5. In the group of phosphor targets, the highest light output is observed for P43 phosphor #1 (see tab. 5.7).

The calculated light yield Y is plotted in figure 5.5 as function of electronic energy loss $\frac{dE}{dx}$. The plot shows a decrease of Y for high atomic number Z as well as a small difference between measurements in slow and fast extraction mode, similar to the observations of light output L.

During beam times with all projectiles in fast and slow extraction mode, the emission spectra of the targets were reproduced similar to those in literature and are thus considered as reliable under irradiation by ion beams with the given beam parameters.

During dedicated radiation hardness test with fast and slow extracted Nickel beam, the light yield of the targets was not decreased significantly (see fig. 5.11) . The highest decrease was observed for Chromium-doped Aluminum Oxide #7 with approximately 11 % loss, relative to the initial light yield. Nevertheless, the light yield level of Al_2O_3:Cr after an accumulation of $2 \cdot 10^{12}$ particles is still high, compared to measurements with UNILAC energies (see PhD thesis [89] or publication [121] of S. Lederer).

The second statistical moments were calculated in horizontal and vertical direction for radiation hardness measurements. Only the YAG:Ce single crystal #5 showed a decrease of beam sizes as function of accumulated particles, while the measurements with a reference grid did not reveal a significant change of beam parameters. It is concluded that in this specific target the high amount of deposited energy per ion pulse created more defects than a diffusion process could recover and that this is also the reason, why the light yield remained relatively constant during the tests. During measurements with A999 #6 an accidental change of operational alignment was performed, so that the change in light yield and beam sizes above $2 \cdot 10^{12}$ accumulated particles is not taken into account. All other investigated targets show reliable beam projections even after an accumulation of $2.5 \cdot 10^{12}$ particles, and an irradiation break of 15 minutes did not lead to a changed observation.

Regarding the design of beam diagnostic elements for FAIR, scintillation screens are preferred that offer a good visible beam projection in a wide range of beam intensity. To avoid overexposure of the recording camera, a screen with low slope m_L of light output per irradiated number of particles should be used. This is the case for the YAG:Ce single crystal #4, produced and supplied by Crytur [80]. The screen responds with a light output, similar to that of Al_2O_3:Cr #7 (see tab. 5.7) but has a better

stability in performed radiation hardness tests, as shown in figure 5.14. The projected beam profiles on YAG:Ce single crystal #4 are increased in the range of approximately 10 % and can thus be regarded as reliable. The screen thickness should be less than for the investigated YAG:Ce single crystal #5, i.e. $d_{screen} < 1.0$ mm, to avoid over exposure of the recording camera at high ionizing irradiation on the one hand and falsified beam sized on the other hand.
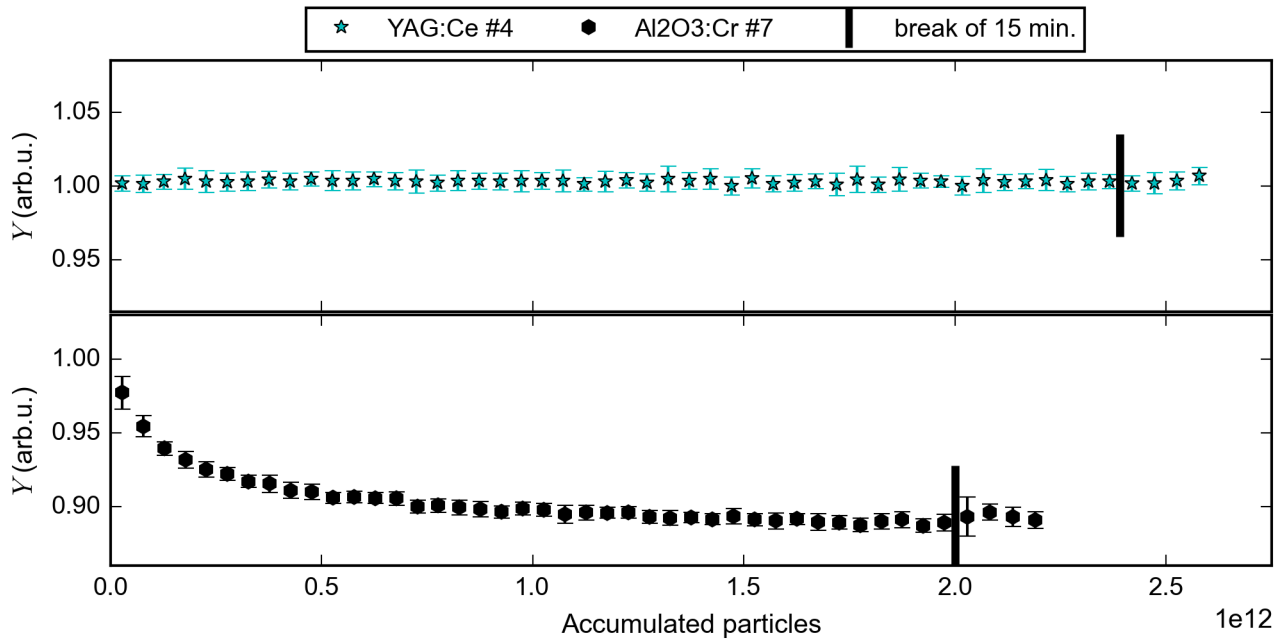

Figure 5.14: Compared view of light yield as function of accumulated particles for YAG:Ce single crystal #4 and Al_2O_3:Cr #7 during performed radiation hardness test with fast extracted Nickel beam #3R.

However, Cerium-doped $Y_3Al_5O_{12}$ single crystals are quite expensive. An installation is recommended in the areas of transition between different FAIR sections, where consecutively high radiation is supposed. The beam alignment to experimental areas is assumed as a straight-forward process, to that here commonly used Al_2O_3:Cr are recommended for installation. If the alignment of low ionization (i.e. low beam intensity or small atomic number Z) is expected, a common P43 phosphor is recommended as scintillation screen.

6 Accelerator Specific Investigations

Additional measurements were performed to investigate two different effects which have been observed during the beam tests. On one hand the commonly used Al_2O_3:Cr screens showed a surprisingly long afterglow characteristic during alignment, especially during beam times with heavy ions with high atomic masses (e.g. uranium). For investigations a few pulses were used from each fast extracted ion beam (see table 4.1). The pulses were analyzed for the light output directly after irradiation and after a specific time span (up to 200 ms).

On the other hand dedicated measurements were performed using a slow extracted Nickel beam at different pulse durations. The scintillation response at constant ion energy and intensity was recorded and analyzed in order to find an explanation for the observed small difference of light output between measurements with fast and slow extracted ion pulses.

6.1 Al_2O_3:Cr Afterglow Measurements

As explained in section 2.5, impurities in a lattice can form traps which increase the phosphorescence in the material [26]. These traps cause the occurrence of afterglow. The afterglow decreases with a simple or even multiple exponential decay, as already observed under irradiation of AF995R[1] with simulated cosmic rays [122, 123].

To check the afterglow characteristics of the Chromium-doped Aluminum Oxide target #7, dedicated measurements with all fast extracted ion beams were performed in addition to the main project. For this the beam spot was recorded with camera #1 (see figure 4.5), using a fixed integration time of 10 ms. Two images were recorded per incident pulse: The first image covered the target response during or directly after ion bombardment. This trigger was kept fixed. The second image recorded the remaining light output at a delayed time after beam extraction from SIS18. The delay was varied between 2 and 200 ms. The integration times of camera #1 were monitored with help of an oscilloscope, as exemplarily shown in figure 6.1.

The background was subtracted by using a median value of the dark area in the scintillation record, while the light output L was calculated similar to the description in chapter 5.2. The light output of the delayed images was divided by the light output of the incident pulse, and the resulting fractions as function of delay time are shown in figure 6.2. A fit algorithm with multiple exponential functions was performed, analog to references from literature [122–124]. The results of the exponential fits are given in the legend of the figure, showing different decay times, i.e. the characteristic time, after which the light output decreased on $\frac{1}{e}$ (≈ 36 %) of the initial value.

First of all an afterglow characteristic was confirmed by observations during irradiation with all investigated projectiles. For measurements with nitrogen, nickel, xenon and uranium, the smallest value

---

[1] Sintered aluminum oxide screen with high density from Desmarquest Co., 99.5 % Al_2O_3, doped with 0.5 % chromium oxide (ruby)
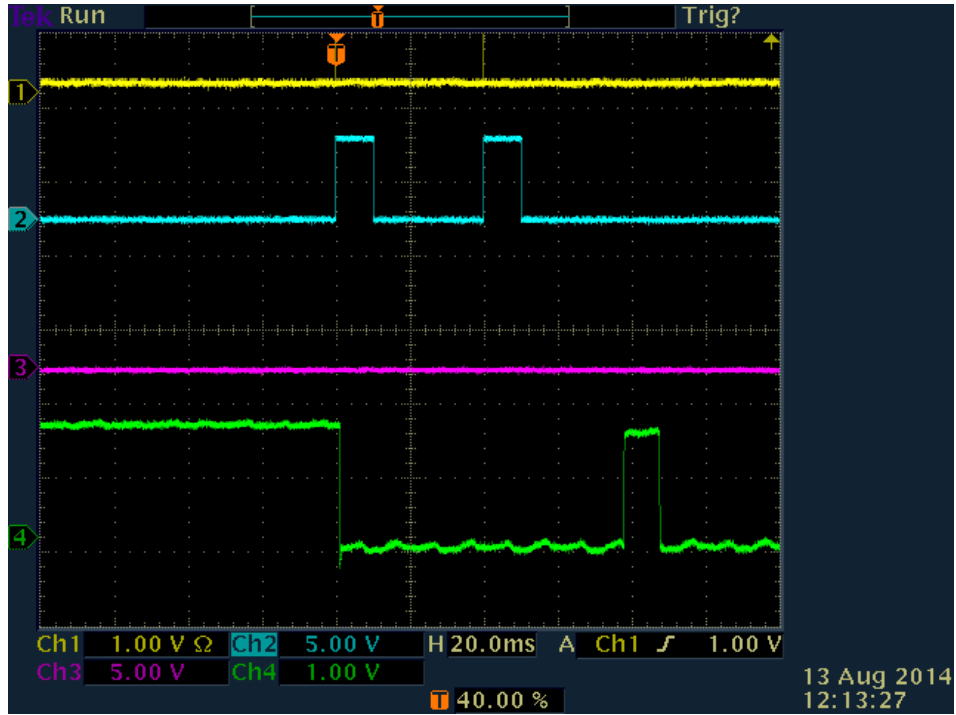
Figure 6.1: Screenshot from camera #1 integration time (blue line) on Tektronix Oscilloscope during measurement of after glow characteristic. The green line represents the beam current measured in SIS18 during acceleration (flat top, left) and extraction (straight drop in the middle), together with the standard calibration pulse (end of the line)
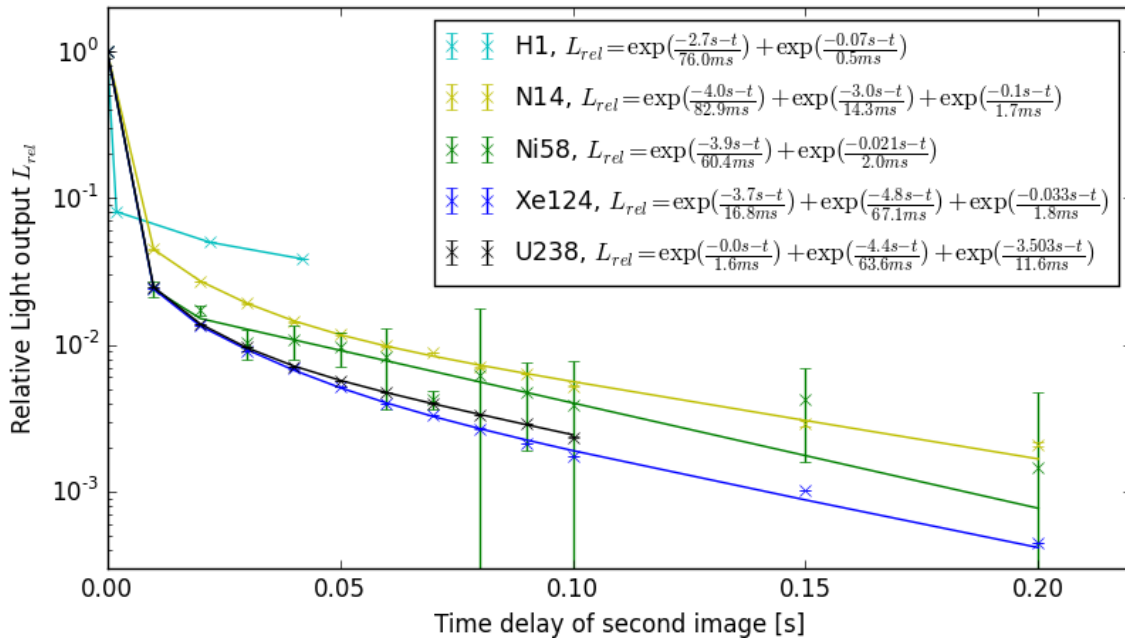
Figure 6.2: Comparison of after glow measurements with Al_2O_3:Cr target #7 for investigated projectiles

of decay time is in the same order for all incident ions with $t_1 \approx 1.8 \pm 0.2$ ms. The second decay after $t_2 \approx 64 \pm 4$ ms is observed during irradiation with Nickel, Xenon and Uranium. For the measurements with Nitrogen beam, the calculation even leads to decay times of more than 80 ms. The measurements with proton beam were performed with different values of delay time and are presented only for completeness. Here at least one decay time (the first mentioned, $t = 76$ ms) is in the same order, as found

for irradiation with the other projectiles. Higher decay times were observed in [122, 123] and also by eye during beam alignment for measurement campaigns. Nevertheless, an appropriate determination of these higher decay times was not possible with the limits of the used optical setup.

In figure 6.3 the values of 200 ms delay and 100 ms delay time from figure 6.2 are plotted as function of the atomic number Z. Due to the already explained limitation of the measurement the values for proton measurements are not shown here. The values for nitrogen, nickel and xenon confirm the dependence of the light output on the projectile size. The value for uranium measurement at 100 ms delay is in contrast to the observation, but can be the result of weak iris setting during scintillation record. A slight over-exposure of the camera during record of the initial light output would result in the observed shift to higher relative values in figure 6.2. A repetition of these measurements with higher resolution are recommended to analyze the observations closer.
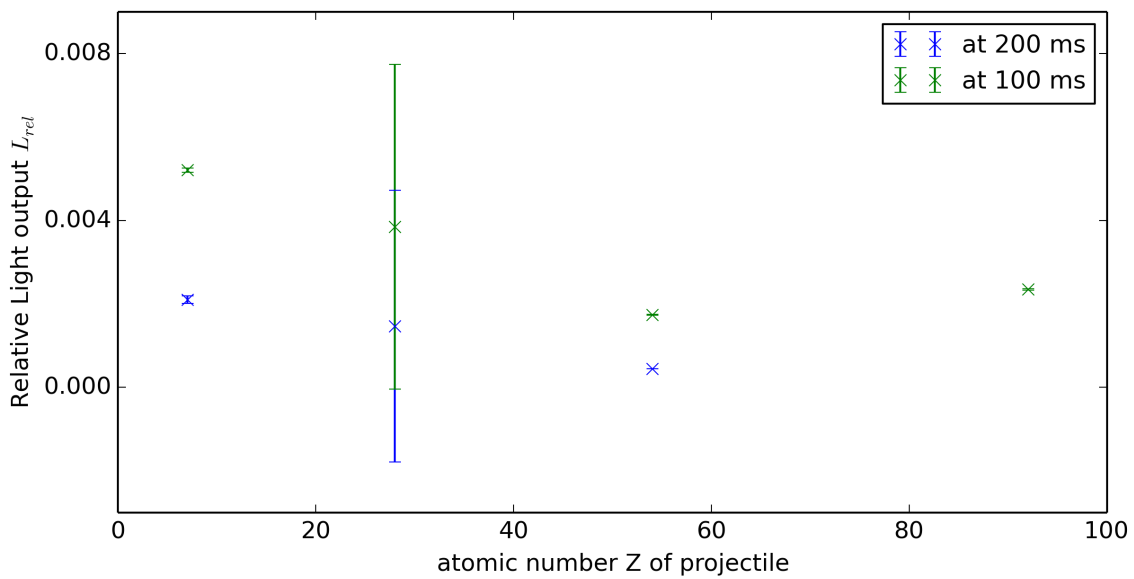
Figure 6.3: Fraction of L_{rel} in dependence of atomic number Z at different delay times

6.2 Varying Slow Extraction Time

Comparing the recorded scintillation during performed beam times, the difference in light output, induced by fast and slow extracted beams, were much smaller than the differences between the pulse durations. In order to give a better comparison between both measurement modes, dedicated experiments with a slow extracted nickel beam have been performed for further investigation in the difference of scintillation between irradiation with slow and fast extracted beam pulses. For this, the extraction time was varied between 300 ms and 4 s.[2] The specific energy was requested with 500 MeV/u to serve as alignment and preparation for an adjacent experiment. This energy was kept fix and is thus no important factor for the investigated characteristics. The targets were irradiated with 50 pulses per chosen extraction time and the beam intensity was kept fixed at $1.5 \cdot 10^9$ ppp. The integration time of camera #1 was always 50 - 90 ms higher than the extraction time to record the full luminescence at each chosen

---

[2] The exposure time of camera #1 is limited to approximately 4.1 s. Thus, it was not able to perform a full record at higher extraction times.

extraction time. Background pictures were recorded after irradiation with the same integration times as during scintillation record. Camera #2 recorded simultaneously but as in the previous measurements, no significant observations occurred.

On the recorded images of the beam spot a ROI was chosen to reduce the noise. The remaining area was normalized by the transmission value of the iris as well as by the beam intensity of the incident pulse. After background subtraction, the light output L was calculated as sum of gray scale values in the ROI.

(a) P43 phosphor #1 together with the chosen values for iris transmission

(b) Al2O3:Cr #7
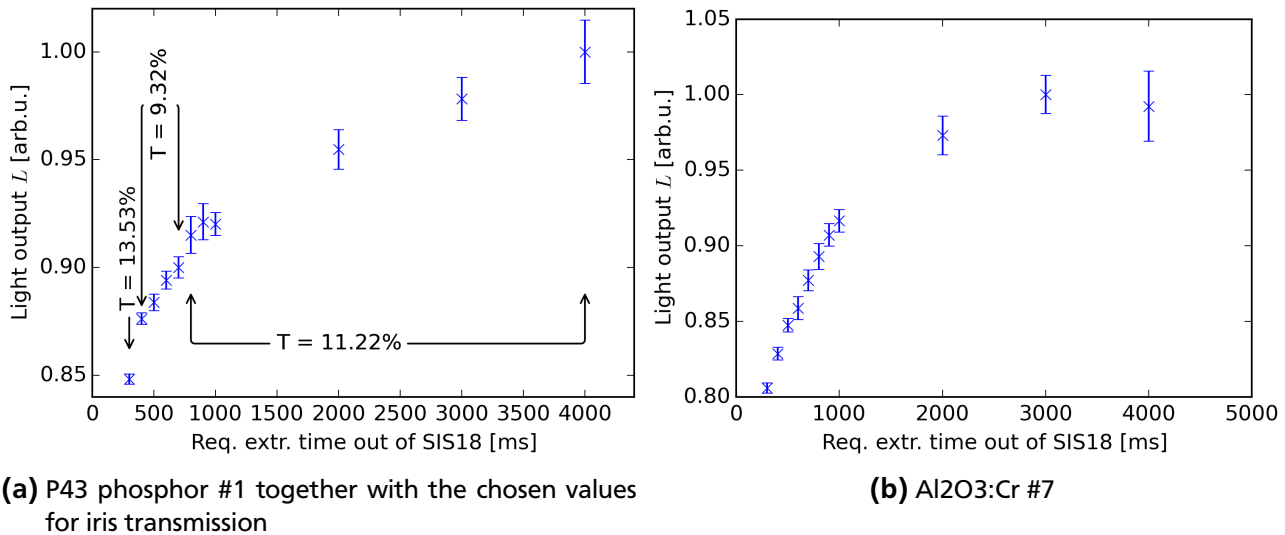
Figure 6.4: Light output L induced by slow extracted Nickel beam for different requested extraction times. L is given relative to the maximum recorded value.

Figure 6.4 shows the calculated average of L for each requested extraction time. The errorbars correspond to the calculated variance of L. The increase of errorbars is assigned to a decreasing accuracy of measured beam intensity for high extraction times. To prove the minor influence of chosen lens closing, the corresponding transmission value T is given, additionally. As can be seen, the relative light output increased even if the iris was widened. Theoretically, the division by a higher transmission value should lead to the decrease of L. However, L is increasing continuously with a non-linear slope. Thus, the observed behavior can not be assigned to an effect of iris transmission.

Even though the chosen range of extraction times is limited to 4.0 seconds, a saturation effect can be observed for both plotted targets already. As already explained in the previous section, Chromium-doped Aluminum Oxide target #7 showed an afterglow effect, that was probably not recorded fully with the adjusted integration time of $t_{extr.time} + 50.0$ ms. Nevertheless, the right plot of figure 6.4 shows a saturation of light output L as function of extraction time, that is similar to P43 phosphor #1 shown in the same figure on the left, where the relaxation time of the scintillation is given with only $t_{relaxation} = 2.6$ ms.

The observations show that the investigated materials are not able to perform with their full scintillation efficiency under irradiation with shortened beam pulses. This matches the model of temporal quenching, which was postulated by Papadopoulos [16, 17] and explained in section 2.4.3. Since energy and intensity of the beam pulses were kept constant, the quenching models explained in sections 2.4.1, 2.4.2 and 2.4.4 were not confirmed.

7 Characterizing ex-situ Measurements

A material can be described by its chemical formula on one hand and on the other hand by the inner structure. Taking e.g. an ideal crystal, it contains a number of layers k with a discrete distance to each other and the sector with a minimal value of k is called "1st Brillouin Zone" [36]. The crystal is built of equidistant unit cells, defined by the three solid angles surrounding the cell's origin, all in perpendicular direction [125].

The structural properties of a material have been investigated by three different methods (UV/Vis transmission, X-ray diffraction and Raman fluorescence spectroscopy), that are shortly described in the following paragraphs.

7.1 UV/Vis Transmission
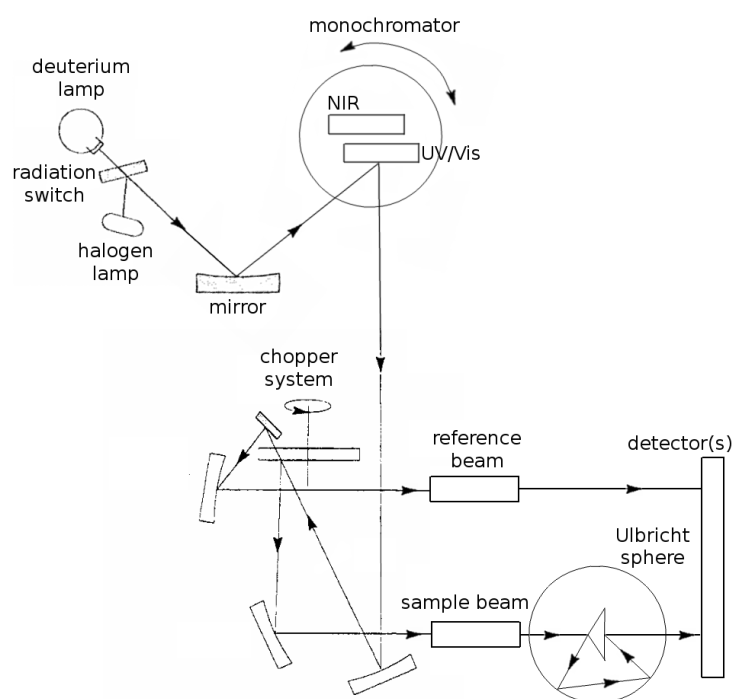
Figure 7.1: Scheme of *Perkin Elmer Lambda 900* device, used for UV/Vis transmission measurements, according to [126]

When irradiated by monochromatic light, the atoms in a material can absorb the incident photons and are lifted from the ground to an excited state (*Franck-Condon principle*, see section 2.3). In general a part of absorbed energy is lost, e.g. by thermal movement, and after a short time (typically ns–μs) the atom relaxes by photon emission of specific wavelength. Absorption measurements, based on this

principle, belong to the group of spectrophotometry and a typical application is the *UV/Vis transmission spectroscopy*. Here the transmission T is deduced from absorption A by [127]:

$$T = \frac{1}{10^A} \qquad (7.1)$$

For the present thesis such transmission measurements were performed using a *Perkin Elmer Lambda 900* UV/Vis transmission spectrometer [126]. A scheme of the device is shown in figure 7.1. It includes two calibrated radiation sources: One deuterium lamp, working in UV range, and one halogen lamp for Vis/IR range. The lamps are switched automatically from one to the other within the UV region by moving of backwards blocking mirror. During the switching process slight deviations in the calibration can not be excluded. After the choice of radiation source the light is transmitted through a monochromator system, which selects the irradiating wavelength. Afterwards a chopper system splits the monochromatic light by reflecting on different mirrors, so that one beam serves as reference and one beam irradiates the sample. In the end the transmission is calculated by the system as fraction of both signals. The detector system provides either a photomultiplier for UV/Vis range or a PbS detector for NIR range, switching automatically at $\lambda \approx 860$ nm. They can measure in a wavelength range from $\lambda = 200$ nm to $\lambda = 2000$ nm with an accuracy of 0.08 nm for UV/Vis range and of 0.32 nm for NIR range. However, the accuracy was limited by a slit to 1.0 nm during measurements for the present thesis. In general the transmission is measured with an accuracy of 0.08 %. To improve the homogeneity of the radiation an Ulbricht sphere is applied in the system.

The transmission of both Ce-doped YAG single crystals #4 and #5 was measured. Due to the lack of a non-irradiated (*pristine*) sample, T was compared with the measurement at the edge of the target screens, where the irradiation and thus also the material damage was minimum. For the Aluminum Oxide ceramics A999 #6 and Al_2O_3:Cr #7 it was not possible to measure the light transmission, due to their high thickness of 0.8 mm and the resulting high opacity. Also the phosphor screens were not measured, because the targets could not be mounted in the spectrometer without destructive contact to the target surface.

The result for YAG:Ce single crystal #4 is given in figure 7.2 and shows the optical transmission from 200 nm till 530 nm. The rest of the measured transmission is not presented, since it does not offer significant differences between both curves. The inset shows the according absorption spectra, calculated with equation (7.1). A difference in the order of 3 % is observed for the UV region, but can also be a result of scatter process at the edge. A significant difference between both measurements that would lead to evidences of material defect formation was not found. The detected minimum values at $\lambda \approx 233$ nm, $\lambda = 340$ nm and $\lambda = 455$ nm are a result of Cerium excitation from ^{4}f to ^{5}d state [83].

Meanwhile the YAG:Ce single crystal #5 appears in principle opaque and is much thicker than YAG:Ce single crystal #4 (factor $\sim$ 7.8). This affects the transmission in general and decreases the value for T as can be seen in figure 7.3. The figure is plotted with similar conditions like figure 7.2. The observed transmission difference between middle and edge of the target is quite small ($<$ 1 %). Since this target has a big screen thickness ($\approx$ 1 mm), the measurement of the edge promotes the scattering of photons at target boundary. Such a scattering is the most probable origin for the increased transmission in this measurement, so that a change of material properties, e.g. a defect formation, could not be proven by the measurement.
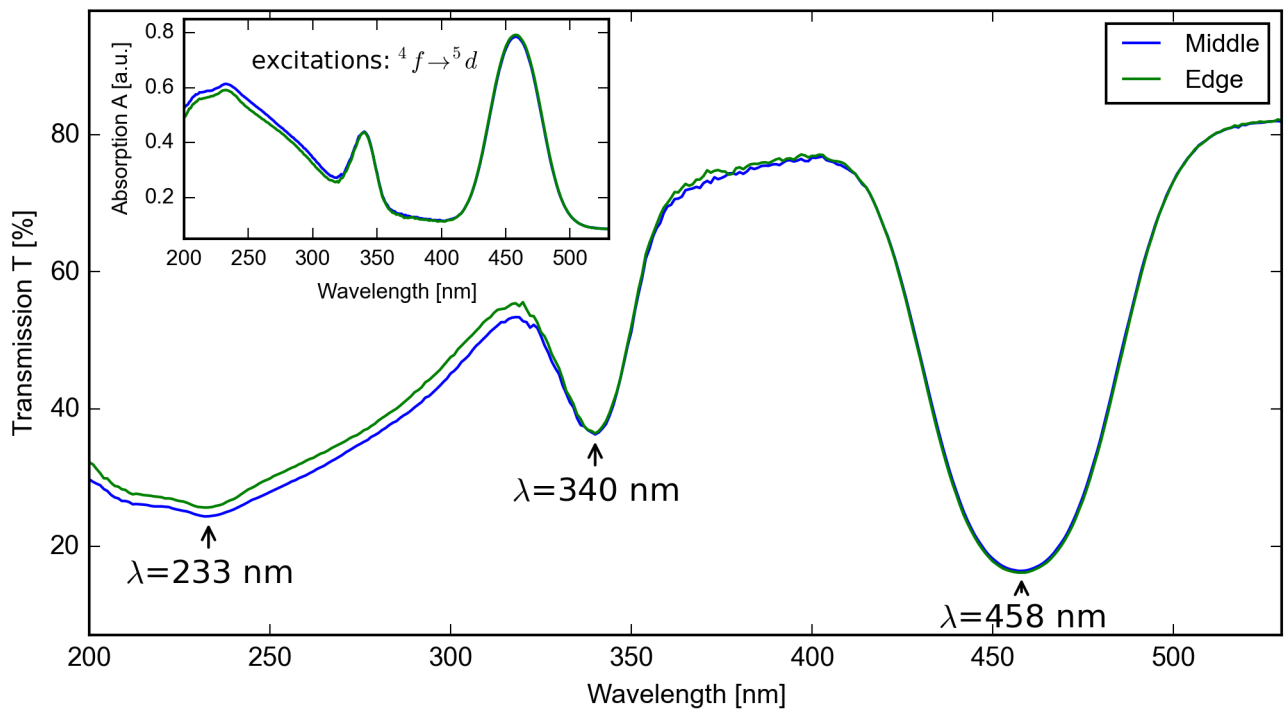
Figure 7.2: Optical transmission of Cerium-doped YAG single crystal #4 from Crytur, measured from 200 to 750 nm and from 200 to 2000 nm in the inset. The measurements were performed in the middle (mainly irradiated part) and at the edge (hardly irradiated part) of the target.
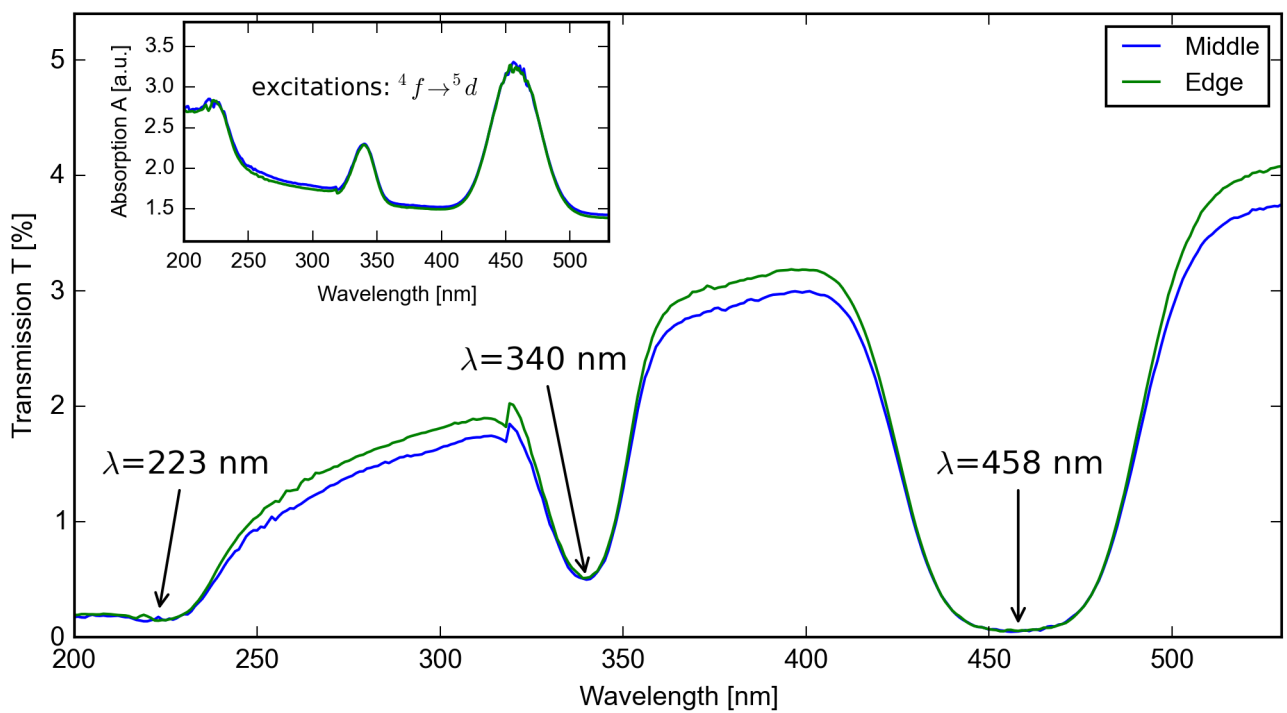

Figure 7.3: Optical transmission of Cerium-doped YAG single crystal #5 from SaintGobain, measured from 200 to 750 nm and from 200 to 2000 nm in the inset. The single crystal was measured in the middle (mainly irradiated part) and at the edge (hardly irradiated part) of the target.

7.2 X-ray Diffraction Analysis (XRD)

When X-rays hit a material, they are scattered and either change their wavelength due to Compton scattering or they are propagated at the same wavelength in a different angle (*Thomson scattering*). For the propagation of Thomson scattered X-rays the Bragg law has to be fulfilled, which is defined for crystalline structures for integers n with [125]

$$2d \sin \theta = n \cdot \lambda \tag{7.2}$$

Here d describes the distance between two atoms or crystal planes in the irradiated material and θ and λ are the scattering angle and wavelength of the scattered light [125]. The integer n is a result of the Laue condition, that demands that the angle of scattered light must be proportional to an integer multiple of the reciprocal lattice vector. Hence, the X-rays are only propagated at fixed points of the crystal. The process results in the observation of discrete patterns that are characteristic for each crystal structure, and any changes in the measured XRD diffraction pattern can serve as evidence for material defects, e.g. amorphization or material strain, in the long-order range of the structure [125].
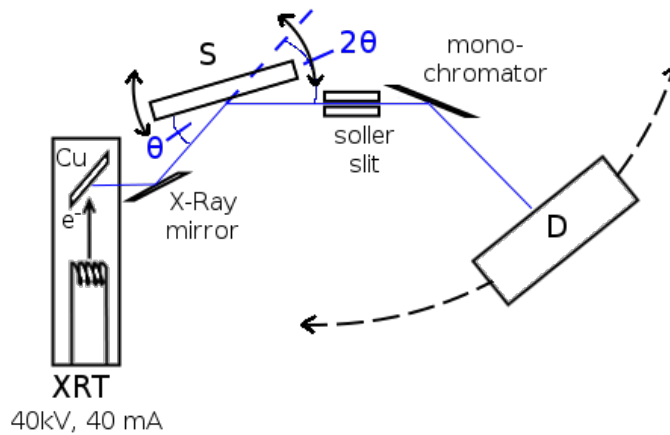
Figure 7.4: Principle of the *Stoe 4 circles diffractometer* used for XRD measurements [128]

A scheme of the used XRD instrumentation *Stoe 4 circles diffractometer* is shown in figure 7.4. It consists of an X-ray tube *XRT* with fixed position. The anode is made of copper and emits at a wavelength of 154.18 pm. A X-ray mirror reflects the rays to the sample *S*. As illustrated in the figure, the sample is mounted movable, so that different incident angles θ can be investigated. On the other side of *S* a long soller slit[1] and a monochromator separate the the Cu K_α line and reflects it on the detector *D*. By moving *D* circularly the 2θ dependence is detected, here in a measurement range from 20 till 100° [128–130]. The instrumentation was calibrated in reference to a silicon powder, so that the measurement accuracy can be estimated with $\Delta(2\theta) \leq 0.5°$.

XRD measurements were performed with both Aluminum Oxide targets. In figure 7.5 the measurement for A999 target #6 is shown for the complete range of 2θ. The according layer symmetries are

---

[1]   parallel metal plates, that collimate the X-rays in a small divergence, here $\Delta \approx 0.3°$
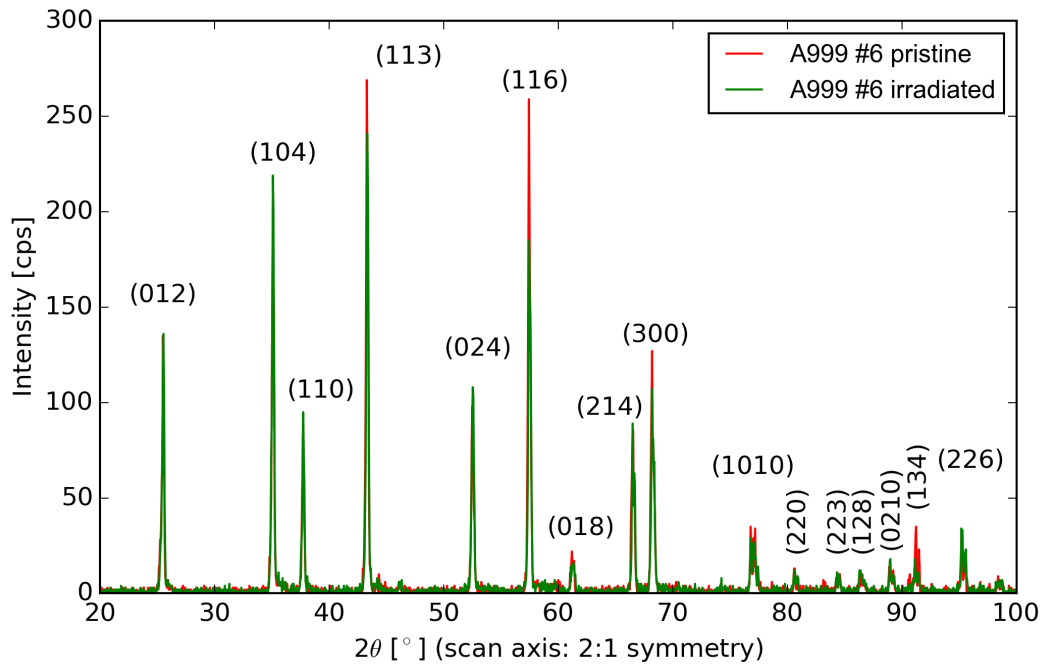
Figure 7.5: Results from XRD measurements for A999 target #6, measured at two different points on the target surface, in comparison with unirradiated material (pristine). Miller indices are given to label the measured layers.
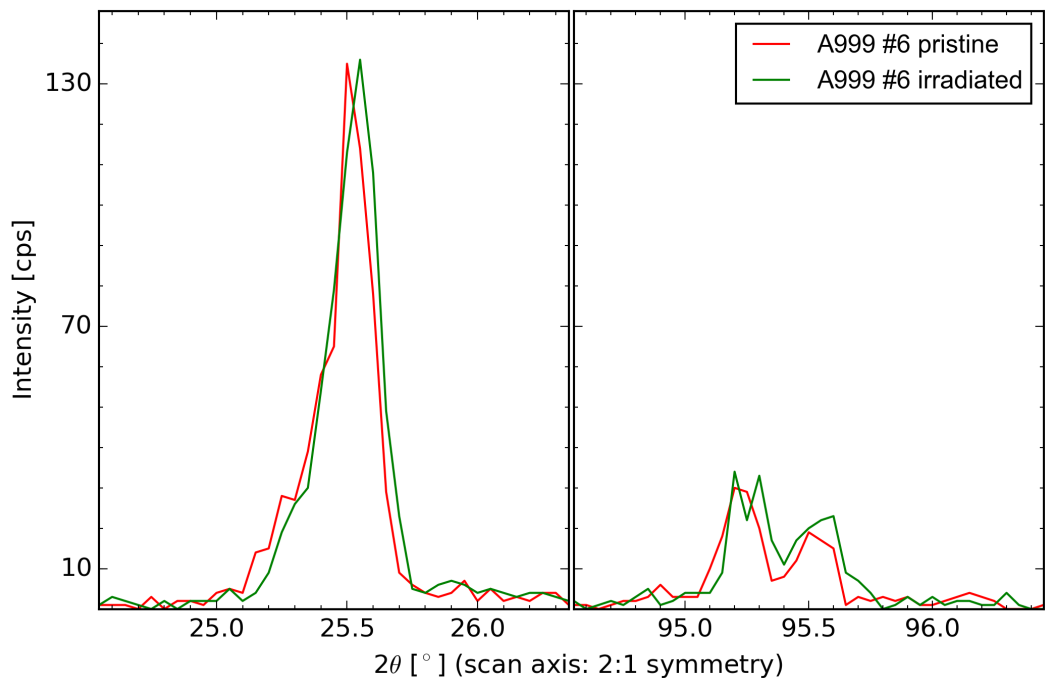
Figure 7.6: Detailed view on $2\theta = 25.5°$ ((012) layer) and $2\theta = 95.2°$ ((226) layer) from figure 7.5. The deviation of both patterns are a result from the sample mounting during measurements.

given in Miller indices at the peaks. Here, no differences can be observed by the eye, which is why figure 7.6 offers a detailed view on the layers at $2\theta = 25.5°$ and $2\theta = 95.2°$. At $2\theta = 25.5°$ the lines of $K_{\alpha 1}$

and $K_{\alpha 2}$ transition are overlayed. With increasing angle 2θ both lines are measured in a bigger accuracy so that they can be distinguished clearly at $2\theta = 95.2°$. In comparison both layers were measured in similar intensities. A small shift in the peak position can be found, similar in direction and order for both shifts. This observation was found for each peak in the measured diffraction pattern so that the origin of this "offset" is explained by small deviations in the sample mounting during XRD measurements. Thus, it can be concluded that the long-range order of the A999 target #6 was not changed by the performed beam times.
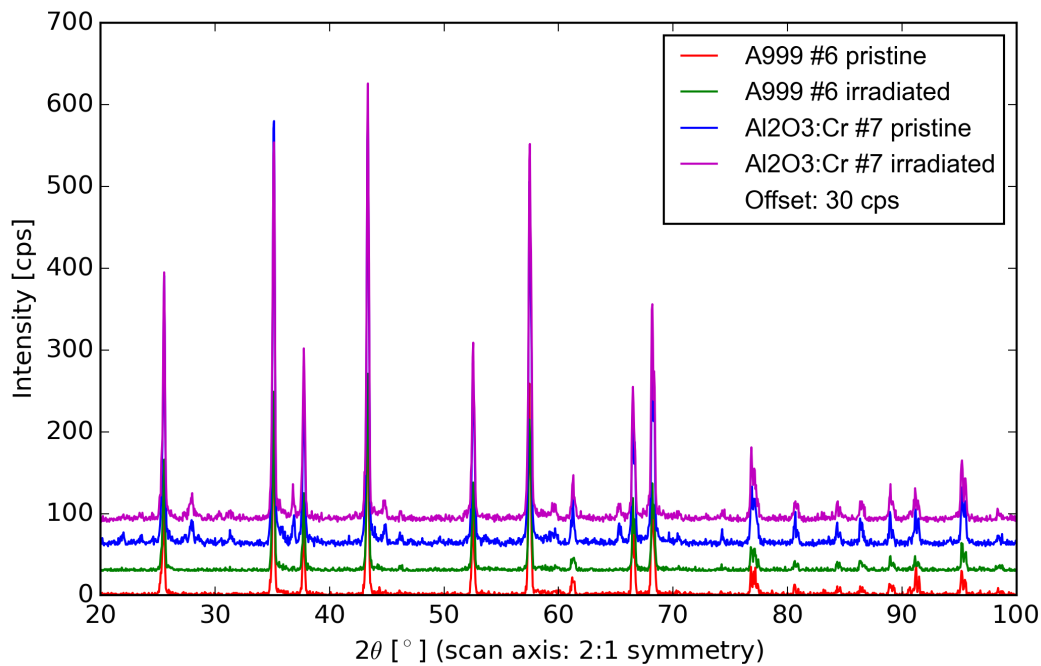
Figure 7.7: Stacked lines plot with y offset of performed XRD measurements on A999 target #6 (lower three plots, the same as in figure 7.5) and Al_2O_3:Cr target #7, together with pristine material. The plot shows the structural change occurring due to Chromium-doping.

The measurement with the Al_2O_3:Cr #7 showed similar results. For completeness figure 7.7 shows the performed measurement on both Aluminum Oxide targets as stacked lines plot. The measurements A999 target #6 from figure 7.5 are plotted lowest. The two upper plots show the measurements of irradiated Al_2O_3:Cr #7 and the according pristine material. The general structure of Al_2O_3:Cr #7 is the same as found for A999 target #6 and the additional lattice symmetries, resulting from the Chromium doping, are measured as reflexes. Also for this target, a change in the long-range order can be excluded by the performed XRD measurements.

7.3 Raman Fluorescence Spectroscopy

When photons of low energy scatter inelastically at a crystal unit, a part of their energy will be converted into excitation of vibrational modes (see also *Franck-Condon principle*, section 2.3). These modes are described by the quasi-particles *phonons* and have usually an energy in the range of *meV*. This process changes the electrical susceptibility χ of the crystal and results in *Raman*, *Stokes* or *Anti-Stokes scat-*

tering [36, 131, 132]. The mode of vibrational excitation can be detected indirectly by measuring the energetic difference between the incident and the re-emitted photon. Basically, the received spectrum is independent of the irradiating energy, which is why the measured spectrum is generally given as function of wavenumbers[2] ν_S or *Raman shift* in cm^{-1}. The choice of wavelength must be concerned well, since measurements with light that deposits to much energy on the material lattice will promote fluorescence. On the other hand phonons can only be released from the material, if the deposited photon energy is high enough. Nevertheless, measurements, that used different monochrome light sources can be compared by simple correction with coefficients, that describe the optical resonances of the target material [36].

The measured Raman spectra are characteristic for the short-range order of the investigated crystal structure. Examples are given in literature e.g. for YAG:Ce single crystals [77, 78, 133] and Aluminum Oxide [90, 91]. Small deviations from reference spectra can already indicate impurities in the material or production process. Also they can be an evidence for an induced changed in the material structure. By measuring the Raman scattered photons in backwards direction, most terms of the Raman tensor are neglected and it is concluded that the only remaining Raman shift component is increasing under compressive stress on the material, while the shift is decreased by tensile stress. A detailed calculation of the Raman tensor and the according variation under performing of stress is found in the publication of de Wolf [131].

For the present project, the irradiated target samples were measured with a *Horiba Jobin-Yvon HR800* System. It works with a laser system consisting of a Helium-Neon laser for irradiation with $\lambda = 633$ nm (red) and an Argon source. For the Argon laser a filter system can be applied to irradiate the samples either with $\lambda = 514.5$ nm (green) or with $\lambda = 488$ nm (blue). The resolution of ν_S is determined mainly by the focal length of 800 mm [134]. The device was calibrated before measurements with a silicon foil, that has a well-known Raman peak at $\nu_S = 520$ cm^{-1} in absence of material stress [131].

Raman spectra of the irradiated targets were recorded and either compared with an un-irradiated material (pristine, if available) or with a measurement of the edge zone of the target screen, where the material damage by ion irradiation was supposed to be minimal. The light source of the Raman spectrometer was chosen such that optic fluorescence was small during measurements.

Figure 7.8 shows the Raman spectrum of $Y_3Al_5O_{12}$:Ce single crystal #4, measured with the red laser ($\lambda = 633$ nm) in the range between 200 and 1200 cm^{-1}. Measurements with the green and the blue laser were performed as well, but did only show fluorescence. The recorded Raman shifts accord to those that can be found in literature for un-doped $Y_3Al_5O_{12}$ material [78, 91, 133]. They are labeled in the figure and listed in table 7.1 together with the assigned transition modes. Here, ν_i means the vibrational modes.

Some modes, given by *Mace et al.* [78], were not verified by the measurements with the targets $Y_3Al_5O_{12}$:Ce #2−#5. This can be attributed to two reasons: On the one hand the Raman peaks can be so weak that they can not be distinguished from the instrument's noise level. This is most probable for the modes that were already measured with a weak level in the reference, e.g. at 310 cm^{-1}, 536 cm^{-1} and 757 cm^{-1}. On the other hand the rare-earth dopant of the targets in the reference consisted of *Dy*, *Yb* and *Tb*, but not of Cerium, or the measurements in the reference were performed with an undoped crystal. This results in slightly different crystal structures and as already mentioned in [78] variations in

---

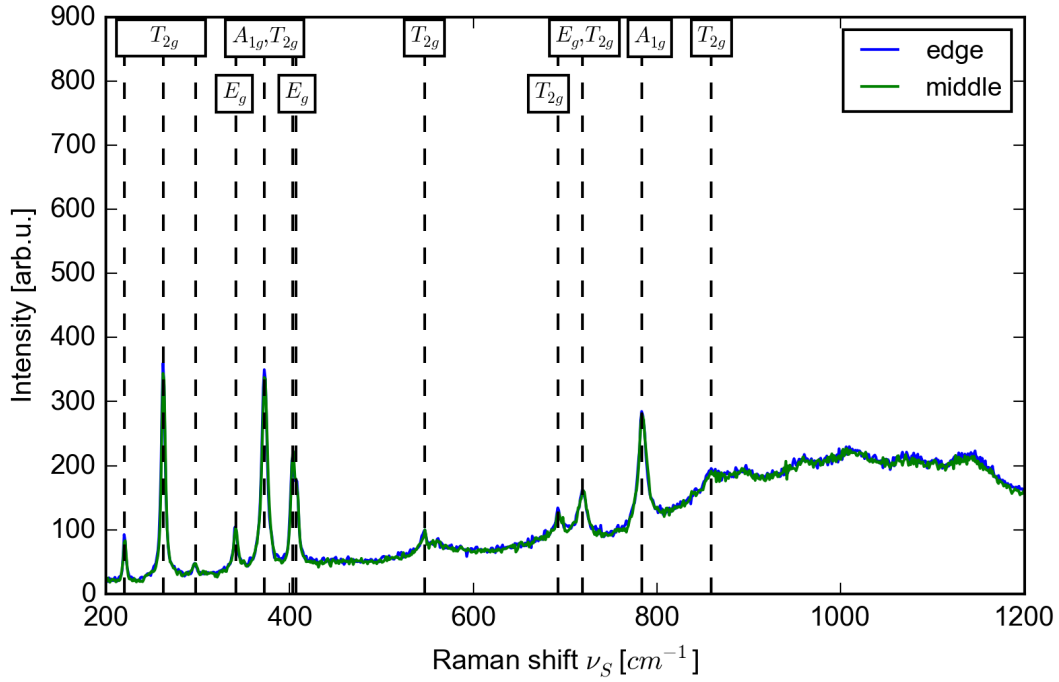2   difference between inverse wavelengths

Figure 7.8: Raman spectra of YAG:Ce #4, measured with a red LASER ($\lambda = 633$ nm). The spectra were measured at the mainly irradiated middle and the minimum irradiated edge of the target. The values of the observed Raman shifts ν_S are given in table 7.1.

Table 7.1: Raman modes found for YAG:Ce single crystal #4 as shown in figure 7.8. The observations are similar for the targets #2, #3 and #5, that have the same chemical composition

Raman Shift ν_S [cm^{-1}]		Assignement
measurement	reference [78]	
221	219	T_{2g} (Translatory + rotary + ν_3)
—	243	T_{2g} (Translatory + rotary + ν_3)
263	259	T_{2g} (Translatory + rotary + ν_3)
297	296	T_{2g} (Translatory + rotary + ν_3)
—	310	T_{2g} (Translatory + rotary + ν_3)
342	340	E_g (Translatory + rotary + ν_3)
373	372	A_{1g}, T_{2g} (Translatory + rotary + ν_3)
404	403	E_g (Translatory + rotary + ν_3)
—	530	T_{2g} (ν_2)
—	536	T_{2g} (ν_2)
547	544	T_{2g} (ν_2)
—	564	T_{2g} (ν_2)
693	690	T_{2g} ($\nu_1 + \nu_4$)
721	716	E_g, T_{2g} ($\nu_1 + \nu_4$)
784	794	A_{1g} ($\nu_1 + \nu_4$)
859	856	T_{2g} ($\nu_1 + \nu_4$)

the vibrational modes can appear. In summary the measured spectrum in figure 7.8 is in good accordance with the values in literature [78, 91, 133].

Also the Raman spectra of the $Y_3Al_5O_{12}$:Ce targets #2, #3 and #5 were measured under the same conditions as $Y_3Al_5O_{12}$:Ce targets #4. They gave peak values at the same position and are not shown explicitly here to avoid repetition. No change in peak position or shape of the measured modes was found in comparison to pristine material or measurements at the target edge. This means that the short-range order of the investigated materials was not modified by the ion irradiation.

The Raman spectra of the aluminum oxide targets A999 #6 and Al_2O_3:Cr #7 were measured with a blue laser ($\lambda = 488$ nm) and are shown in figures 7.9 and 7.10. Measurements with higher wavelengths did not deposit enough energy to the material lattice, so that no vibrational mode could be observed. The vibrational modes were assigned to the peak values in figures 7.9 with help of the reference by *Porto et al.* [91]. Table 7.2 gives a comparison between the performed measurements and the values in the reference. Since in the given accuracy of the instrumentation the Raman shifts were observed at the same positions for both aluminum oxide screens, it is concluded that the dopant in target #7 has no influence on the short-range order of the material.
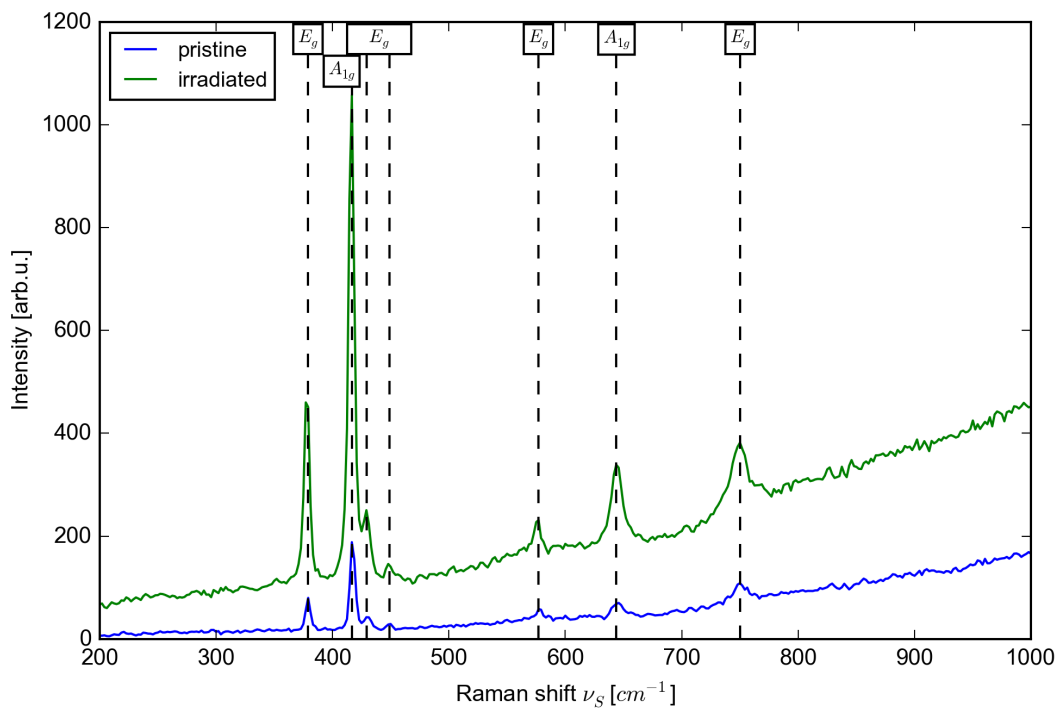
Figure 7.9: Raman spectrum of A999 #6, measured with a blue LASER ($\lambda = 488$ nm) at some irradiated part of the screen and at a dark spot. The blue line belongs to a measurement of a pristine A999 target for comparison. Vertical lines were added on the measured vibrational modes to guide the eye.

On base of reference [91] an explanation for the observed vibrational modes is given: Due to the $R\bar{3}c$ symmetry, explained in section 3.3.3, only two optical modes can be measured by Raman process: One is the symmetrical vibration A_{1g}, where the axes oscillate coherent to each other. The other one is the asymmetrical vibration E_g, where the oscillation of the lattice planes happen orthogonal or incoherent

Table 7.2: Raman modes found for A999 target #6 as shown in figure 7.9. The observations are similar for the Chromium-doped Aluminum Oxide targt #7.

Raman Peak [cm⁻¹]		Assignements
measurement	reference [91]	as given in [91]
379	378	E_g (external → rotation / translation)
417	418	A_{1g} $(xx + zz)$
430	432	E_g (external → rotation / translation)
449	451	E_g (external → rotation / translation)
577	578	E_g (internal)
644	645	A_{1g} (zz)
750	751	E_g (external)
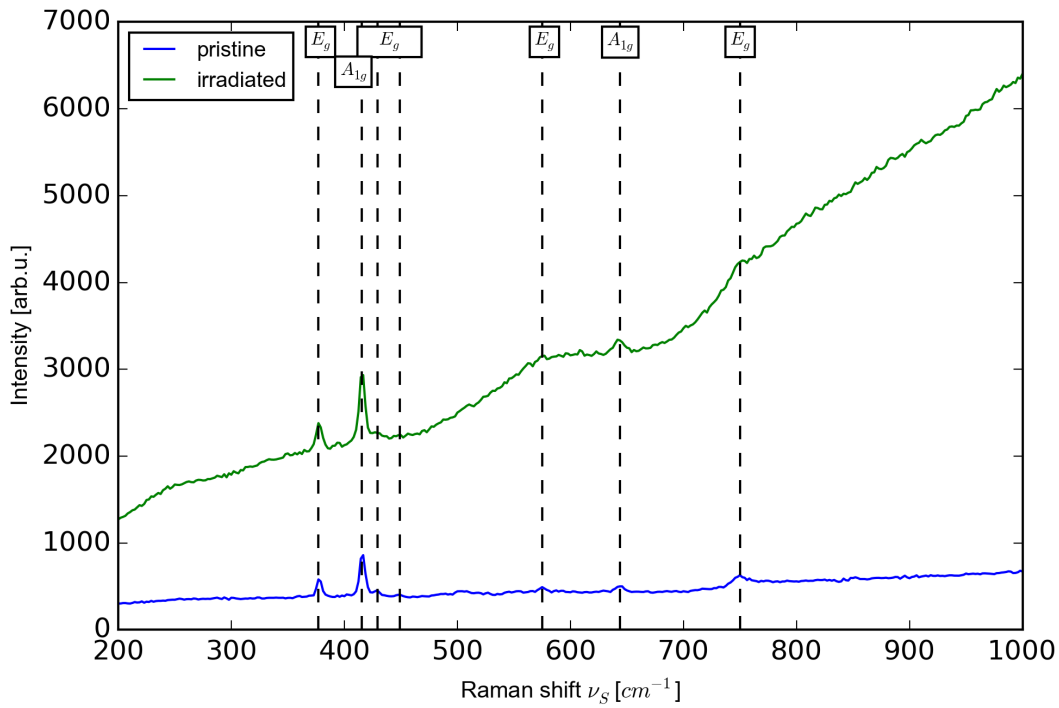
Figure 7.10: Raman spectrum of Chromium-dopted Aluminum Oxide #7, measured with a blue LASER ($\lambda = 488$ nm). The blue line belongs to a measurement of a pristine A999 target for comparison. Vertical lines were added on the measured vibrational modes to guide the eye.

to each other. Reference [91] reported on the Raman modes in four different planes to give an exact assignment of the vibrational modes, regarding to the polarizability tensor of the D_{3d} group [132]:

$$\vec{D} = \begin{pmatrix} \frac{d\mu_x}{dx} & \frac{d\mu_x}{dy} & \frac{d\mu_x}{dz} \\ \frac{d\mu_y}{dx} & \frac{d\mu_y}{dy} & \frac{d\mu_y}{dz} \\ \frac{d\mu_z}{dx} & \frac{d\mu_z}{dy} & \frac{d\mu_z}{dz} \end{pmatrix} = \begin{pmatrix} \alpha_{xx} & \alpha_{xy} & \alpha_{xz} \\ \alpha_{yx} & \alpha_{yy} & \alpha_{yz} \\ \alpha_{zx} & \alpha_{zy} & \alpha_{zz} \end{pmatrix} \tag{7.3}$$

Per definition two A_{1g} modes can be measured, where the matrix elements in (7.3) are non-zero at α_{xx}, α_{yy} and α_{zz}. The E_g modes can be found five times in the Raman spectra: Three of the modes

are a result of internal or "classical" vibrations, while the remaining two modes are called "external" vibrations and are a result of a strong and quasi-free move of the Al_2O_3 atom in the lattice (e.g. rotation or translation).

The vibrational assignments are given together with the peak positions in table 7.2 and are found in the measurements (see figure 7.9 and 7.10). In the spectra of the irradiated materials the Raman peaks for shift values $> 500\ cm^{-1}$ are weak, because the irradiation caused an increased fluorescence background. A significant change of the peak positions or an increase was not observed, so that a change of the material structure by the performed ion irradiation was not proven.

Raman spectra of the P43 phosphor target #1 were also measured. They are presented in this thesis, even though a discussion of the measurement is difficult, due to a small number of references in literature. The irradiated sample was measured with the red light source ($\lambda = 633$ nm) and compared with the measurement of a pristine sample. Both spectra are shown in figure 7.11. The change of absolute intensity is disregarded here, since it was influenced easily by change of optical focus. Peak values were observed at 110 cm^{-1}, 197 cm^{-1}, 430 cm^{-1} and 456 cm^{-1} and are comparable with measurements of Gd_2O_2S host crystals, recorded by Dr. Yan during his PhD studies [135]. Thus, the measured shifts are assigned to the medium material Gd_2O_2S. No significant difference could be found between measurement of the irradiated and the pristine material, that would implicate a material modification by the performed beam times.
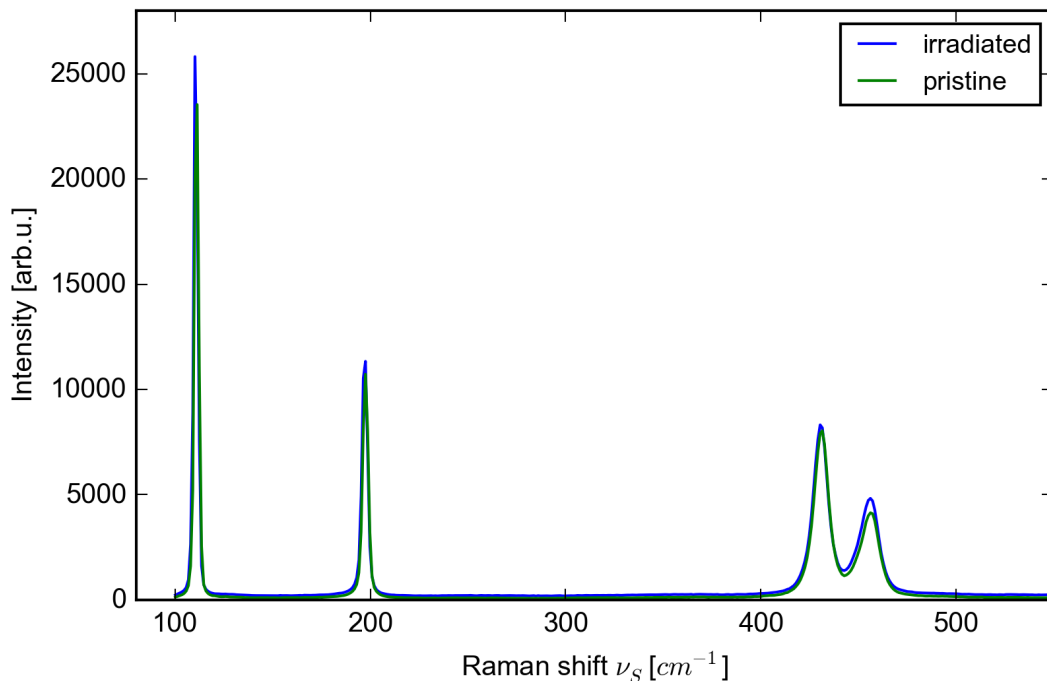
Figure 7.11: Raman spectrum of P43 phosphor #1, measured with a green LASER ($\lambda = 633$ nm), compared with the measurement of a pristine sample.

7.4 Résumé

Within the capabilities of the used instrumentations, all irradiated scintillation targets were investigated for modifications in the long-order or short-order range, respectively. Three analysis methods were used, namely UV/Vis transmission spectroscopy, X-ray Diffraction (XRD) and Raman fluorescence spectroscopy, and the measurements were compared either with a pristine material of the same composition or with measurements at the edge of the target surface, where the degree irradiation in the material was minimal. The recorded patterns were compared and characterized on hand of references in literature, if available. No significant deviations were observed during measurements that could serve as evidence for characteristic material defects.
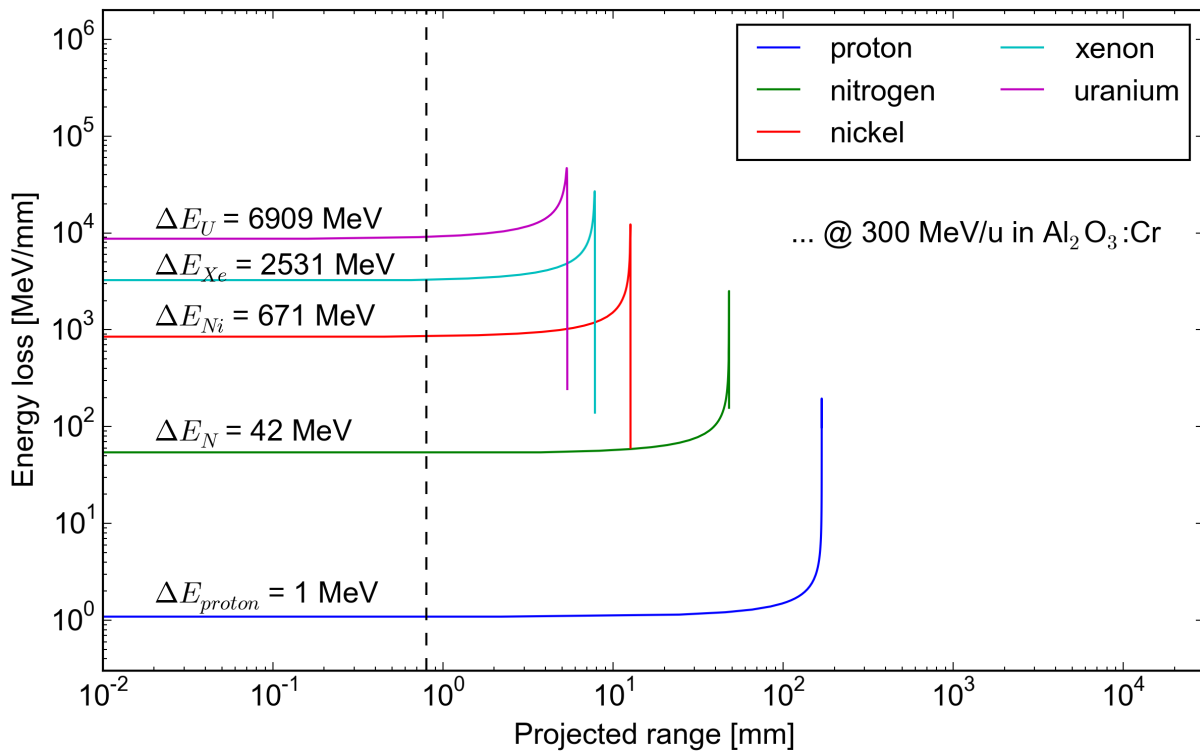
Figure 7.12: Bragg peak of investigated ions in Chromium-doped Aluminum Oxide #7, calculated with SRIM [27], the vertical line represents the target thickness

However, this result is no surprise, since calculations with SRIM [27] showed that only a fraction of the ion energy is deposited in the material: As shown in figure 7.12 for the Al_2O_3:Cr target #7, the Bragg peaks of all requested ions exceed the material thickness (indicated by the vertical dashed line). The calculated fraction of deposited energy E_{dep} was thus generally in orders of $0.5 \cdot 10^{-5}$ of the complete ion energy E_{ion}, and it was deposited linearly over the target depth. The resulting amount of deposited energy ΔE was calculated, using the rectangular spread by the Bragg curves and the target thickness. The values of ΔE are given with the according curves in figure 7.12.

Furthermore, SRIM was used for simulations of an uranium ion, irradiated at different beam energies on a Chromium-doped aluminum oxide target. As parameters a layer made of Al_2O_3 (material density $\rho = 3.73 \frac{g}{cm^3}$, 800 μm thick, tilted with 45°) was defined and the irradiation of 1000 uranium ions in

the material was calculated. Table 7.3 shows the results for three different specific energy values E_{spec}. The first row presents the calculation at 300 MeV/u and is thus similar to the conditions in the present thesis. The energy for the second row was chosen with E_{spec} =86 MeV/u, because the projected range spreads over the full width of the target. The third row in table 7.3 was calculated with a typical energy from the pre-accelerating system UNILAC in GSI (see section 3.1).

The table gives the values for the specific energy E_{spec}, the according total energy E_{total} of the uranium ion, the electronic energy loss $\frac{dE}{dx}$ and the energy ΔE, deposited in the target. As can be seen, the energy loss increases for decreasing ion energy, as result of different stopping power (see section 2.2). The calculated number of displacements per ion (dpi) shows a damage ratio of only 10 %, compared to the calculation for UNILAC energy, and thus confirms the observations of the present thesis. Moreover, dpi shows a dynamic behavior for the calculation with ions at 86 MeV/u: Here SRIM ran into a runtime error, indicating, that the number of displacements exceeded 200000 [27]. This shows that an irradiation with this parameters is causing the highest damage ratio in a Al_2O_3 target, similar to the investigated one.

Table 7.3: Calculation of energy, range and displacements per ion (dpi) of uranium in Al_2O_3:Cr target #7, calculated with SRIM [27].

$E_{spec} \frac{\text{MeV}}{\text{u}}$	E_{total} [GeV]	$\frac{dE}{dx} \left[\frac{\text{MeV}}{\text{mm}}\right]$	ΔE [MeV]	projected range [μm]	dpi
300 MeV/u	71.42	$8.636 \cdot 10^3$	6909	>800	17585
86.0 MeV/u	20.47	$17.49 \cdot 10^3$	1820421	796.37	>200000
11.4 MeV/u	2.71	$43.32 \cdot 10^3$	85210	68.91	160355

8 Conclusion and Outlook

8.1 Summary and Conclusion

Seven scintillation screens, made of inorganic material, were investigated with respect to their emission properties during irradiation with high energetic heavy ions. Each screen turns a deposited energy into photon emission in the visible range of the spectrum. This process, called scintillation, was described in chapter 2 in terms of electron-hole-pair creation and recombination. The ideal scintillation process is usually influenced by different aspects, e.g. the occurrence of material defects or the inability for linear transformation into light under specific irradiation parameters. The resulting change of emission properties was summarized with the term *quenching*, from which four dedicated models were described in chapter 2 as well.

The irradiation of the scintillation screens was performed with different heavy ions of high energy at GSI Helmholtzzentrum für Schwerionenforschung GmbH in Darmstadt. While the first part of chapter 3 gave an overview into the principles of heavy ion acceleration and the use of scintillation screens as beam diagnostic tool, the investigated materials were introduced in the second part of the chapter. The target collection consisted of phosphor screens (P43 and P46 phosphor), single crystals (Cerium-doped $Y_3Al_5O_{12}$) and Aluminum oxides (pure and Chromium-doped Al_2O_3). They were irradiated with five different ion types (proton, nitrogen, nickel, xenon and uranium), extracted in fast (1 μs) and slow (300-400 ms) extraction mode from heavy ion synchrotron SIS18 at a specific beam energy of E_{spec} = 300 MeV/u. The variation and measurement of irradiation parameters was described in the first part of chapter 4, while the second part explained the optical setup, used for record of the induced scintillation. The record included not only the measurement of light output and beam profile, but also the measurement of emission spectrum during irradiation. The third part of chapter 4 together with the first part of chapter 5 explained the basic principles of the performed data acquisition and analysis.

After the performed beam times, the light output L, light yield Y (i.e. L per deposited energy and particle), beam profile and emission spectra were calculated and analyzed from the recorded images. The results were presented in chapter 5 for measurements with different beam intensities, as well as for two performed radiation hardness tests with a nickel beam at 300 MeV/u (in slow and fast extraction mode, each). Chapter 6 described two dedicated measurement campaigns, investigating specific observations during beam alignment and measurements. Optical methods (UV/Vis transmission, XRD analysis, Raman fluorescence spectroscopy) were applied to the screens after beam times to investigate in structural changes and possible formation of defects. The measurements and results were summarized in chapter 7.

All target screens showed a linear behavior of light output L to the irradiation with different beam intensities. This dependence was observed for all performed beam times, independent of the requested projectile and extraction mode. A saturation of L under multiple-particle irradiation could thus not

be proven. The calculated profile characteristics in horizontal and vertical direction and the recorded emission spectra were invariant as well under irradiation with different numbers of particles per pulse.

The analysis of the light yield Y showed a different behavior: With increasing atomic number Z and so with increasing electronic energy loss $\frac{dE}{dx}$ the light yield decreased in comparison to the measurements with nitrogen beam. This observation stays in good accordance with the measurements from the proton beam time, where a change in the optical setup was necessary (removal of neutral density filter). The origin of the decrease is explained by the quenching model of Michaelian and Menchaca-Rocha (see section 2.4.2). Here, the recombination of electron-hole pairs to photons is substituted by non-radiative processes, which results in a non-linear dependence of the scintillation amplitude under irradiation with different heavy ions.

During radiation hardness tests with slow and fast extracted nickel beams, an increase in the light yield Y was observed for the targets from supplier Crytur (P46 phosphor #3 and YAG:Ce single crystal #4) and is explained by diffusion processes of charge carriers in the material. In the meantime, P46 phosphor #2 showed an invariant light yield Y, while in the YAG:Ce single crystal #5 the induced material defects overcome the charge carrier diffusion and lead to a decrease of Y. After an irradiation break of 15 minutes, followed by another scintillation record for verification, the target materials turned back to the initial level of light yield. Thus, it is concluded that any changes in the these materials were temporary permutations during the irradiation.

Meanwhile, the light yield Y of aluminum oxide ceramics decreased during both performed radiation hardness tests. The decrease was observed for the pure as well as for the chromium-doped aluminum oxide and saturated for measurements in both extraction modes on a level of 90-97 % of the initial light yield value. The ceramic with chromium doping degraded faster and saturated on a lower level (approximately 90 % of initial value) than the pure aluminum oxide. It is known from literature that the transformation from F to F^+ centers, induced by ion irradiation, can reduce the light yield of A999 [89]. For the chromium-doped target, the trap of chromium ions is the most probable reason for the light yield decrease. After irradiation break the light yield of both targets remained on the value of saturation. The material properties must have been changed permanently, but from the degree of light yield decrease we can conclude that the degree of modification in the material is in a small range in both target screens.

Different phenomena during beam alignment were investigated additionally to the main subject of ion induced quenching behavior. On the one hand, focus was set on the afterglow characteristic of the Al_2O_3:Cr target #7. For this, the light yield 2-200 ms after irradiation with fast extracted beam pulses was determined and compared to the light yield during irradiation. An exponential decay of $Y(t)$ was found for each of the requested ion types. Even though, the optical setup limits the measurement range to a few hundred ms after irradiation, the observation implicated a Z dependence of the afterglow and further investigations are proposed.

The difference of light output, measured in fast and slow extraction mode, was determined to be much smaller than expected by the differences of pulse duration. Thus, the P43 phosphor #1 and the Al_2O_3:Cr #7 were irradiated with a slow extracted nickel beam at 500 MeV/u. The extraction time was varied between 300 ms and 4 seconds. The light output showed a non-linear behavior as function of

extraction times, and a saturation for higher extraction times is implicated. Dedicated measurements, with signal amplifying cameras and measurement ranges up to seconds, would contribute to a further understanding of the observed phenomenon.

For the choice of a scintillation screen as diagnostic element in FAIR beam alignment, different materials are recommended: In the intersection parts between consecutive FAIR sections, a continuously high level of radiation is expected. Access to the areas, e.g. for maintenance of the diagnostic elements, is then difficult or even impossible. Besides, it is recommended to install only highly radiation hard materials, that inherit a minimum probability for quenching transitions. For these sections, cerium-doped $Y_3Al_5O_{12}$ single crystals should be installed. Using a low thickness (e.g. in the range of 300 μm), these screens provide a minimal influence on the imaging properties by photon scattering in the material. Referring to chapter 5, the YAG:Ce single crystal #4 proved a good visible beam projection in a wide range of beam intensity and a reliable response to ion irradiation even after $2 \cdot 10^{12}$ accumulated particles. In contrast to the phosphor screens, the single crystal offers the additional advantage of easy transport and handling. Nevertheless, YAG:Ce single crystals have a high cost-disadvantage, which is why for extraction out of the storage rings and for alignment experimental areas Al_2O_3:Cr is recommended, as already used commonly. If low ionizing ion beams, i.e. beams with low atomic number of a low number of particles per pulse, are aligned, a P43 phosphor screen is a better choice as diagnostic element, due to the high scintillation efficiency.

8.2 Outlook

In summary, a saturation of light output as function of beam intensity was not proven. However, the occurrence of such a quenching effect can not be excluded and is supposed for irradiation for higher orders of beam pulse intensity, than available in the performed beam times. Measurements with more than 10^{10} ppp are recommended to perform further investigations. At this high energy regime, the requested projectiles should have an atomic number $Z \geq 50$, due to the $\frac{Z}{A}$ dependence of the Bethe-Bloch-equation (2.1). This proposal is confirmed by exemplarily calculations of different Bragg peaks with SRIM in Al_2O_3:Cr #7 (see figure 7.12), showing the increased amount of deposited energy for irradiation with xenon and uranium.

As shown in figure 2.2 the deposited energy changes into a plateau for beam energies of $E_{spec} > 100$ MeV/u. A further increase of beam energy, as supposed for FAIR beam alignment, should thus lead to an equal or linearly decreased light output during irradiation. Such dependences should be investigated for a specific choice of targets under ionic irradiation with different energies E_{spec}. As shown by SRIM-calculations (see figure 6.2) only a fraction of ion energy is deposited in the scintillation screens. Thus, for experiments with varying ion energies, a projectile with high ionizing potential (e.g. uranium) is recommended.

Speaking of energy variation, the light yield dependence of the electronic energy loss should be measured at fixed beam energies. A region behind a fragment separator should be used for measurements, since the dependence, shown in figure 5.5, could than be presented in a better resolution.

Further investigations on the temporal dependence of each, the light output under varying extraction time and the scintillation afterglow characteristic of Chromium-doped Al_2O_3 are proposed. Dedicated measurements, with signal amplifying cameras and time variations up to ranges of a few seconds would contribute for a further understanding and characterizing of the observed phenomena.

To receive a factor of goodness for transverse beam alignment, the measure of emittance is commonly performed. The transverse emittance is defined by the position x of a beam particle and the angular spread of the particles transverse path x'. Both factors form an ellipse, as shown exemplarily in figure 8.1 for the horizontal plane of a beam. In the vertical plane (y-axis) the emittance looks similar or is mirror-inverted due to focusing by FODO elements.
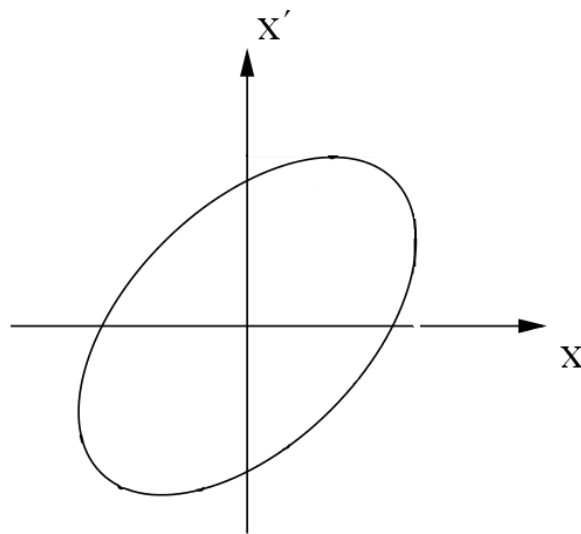
Figure 8.1: Examples for transverse emittance, on basis of [45]

The emittance (in one plane) is commonly measured by slit grid devices [57, 58]. The particles are passing a highly absorbing material through a thin slit. The slit opening is typically in the range of hundreds of micrometer. The dispersion of the particles is nowadays measured with a SEM-grid in a discrete distance after the slit. However the resolution of the emittance measurement is limited by the resolution of the grid taping and the radius of the grid wires. Higher resolutions can be achieved by replacing the SEM grid by a scintillation screen, as e.g. investigated in the present thesis. Furthermore, horizontal and vertical beam emittance can be determined in a single measure by replacing the slit with a pepper-pot-mask [1]. Investigations in this subject are thus proposed and since their linearity under irradiation with high energetic heavy ions was proven in this thesis, P43 phosphor, P46 phosphor, Cerium-doped YAG single crystal, as well as pure and Chromium-doped Aluminum Oxide screens are recommended as target screens.

---

[1] A mask of high absorbing material with a number of small holes in micrometer range, remembering on a pepper-pot.

Bibliography

[1] GSI Helmholtzzentrum für Schwerionenforschung GmbH, =http://www.gsi.de/, prior: July 2015.

[2] Facility for Antiproton and Ion Research in Europe GmbH, =http://www.fair-center.eu/, prior: September 2015.

[3] H. Gutbrod, I. Augustin, H. Eickhoff, K. Groß, W. Henning, D. Krämer, and G. Walter, "FAIR Baseline Technical Report, 2006."

[4] E. Gütlich, *Abbildungseigenschaften von Szintillatoren für Schwerionenstrahlen und diesbezügliche Modellrechnungen*. PhD thesis, TU Darmstadt, 2011. `http://tuprints.ulb.tu-darmstadt.de/id/eprint/2699`, [prior: July 2015].

[5] E. Gütlich, W. Ensinger, and P. Forck, "Light yield, imaging properties and spectral response of inorganic scintillators under intense ion irradiation," in *Proc of 14th Beam Instrumentation Workshop (BIW)* (C. Dillingham and J. Chew, eds.), (Santa Fe, USA), pp. 151–155, 2010.

[6] B. Walasek-Hohne, C. Andre, P. Forck, E. Gutlich, G. Kube, P. Lecoq, and A. Reiter, "Scintillating Screen Applications in Accelerator Beam Diagnostics," *Nuclear Science, IEEE Transactions on*, vol. 59, no. 5, pp. 2307–2312, 2012.

[7] K. Renuka, F. Becker, W. Ensinger, P. Forck, R. Haseitl, and B. Walasek-Hohne, "Imaging Properties of Scintillation Screens for High Energetic Ion Beams," *Nuclear Science, IEEE Transactions on*, vol. 59, no. 5, pp. 2301–2306, 2012.

[8] K. Renuka, W. Ensinger, C. Andre, F. Becker, P. Forck, R. Haseitl, and A. Reiter, "Transverse Beam Profile Monitoring using Scintillation Screens for High Energy Ion Beams," in *Proceedings of the 15th Beam Instrumentation Workshop (BIW)* (T. Satogata, J. Lab, and J. Chew, eds.), (Virginia, USA), pp. 183–185, 2012.

[9] K. Michaelian, A. Menchaca-Rocha, and E. Belmont-Moreno, "Scintillation response of nuclear particle detectors," *Nuclear Instruments and Methods in Physics Research Section A: Accelerators, Spectrometers, Detectors and Associated Equipment*, vol. 356, no. 2, pp. 297 – 303, 1995.

[10] A. Menchaca-Rocha, "A simplified scintillator-response formula for multiple-ion energy calibrations," *Nuclear Instruments and Methods in Physics Research Section A: Accelerators, Spectrometers, Detectors and Associated Equipment*, vol. 602, no. 2, pp. 421–424, 2009.

[11] K. Michaelian and A. Menchaca-Rocha, "Model of ion-induced luminescence based on energy deposition by secondary electrons," *Physical Review B*, vol. 49, pp. 15550–15562, 1994.

[12] W. Klamra, M. Balcerzyk, M. Kapusta, A. Kerek, M. Moszynski, L.-O. Norlin, D. Novak, and G. Poss-nert, "Studies of scintillation light nonproportionality of ZnSe (Te), CsI (Tl) and YAP (Ce) crystals using heavy ions," *Nuclear Instruments and Methods in Physics Research Section A: Accelerators, Spectrometers, Detectors and Associated Equipment*, vol. 484, no. 1, pp. 327–332, 2002.

[13] M. Jiménez-Ramos, J. G. López, M. García-Muñoz, M. Rodríguez-Ramos, M. C. Gázquez, and B. Zurro, "Characterization of scintillator materials for fast-ion loss detectors in nuclear fusion reactors," *Nuclear Instruments and Methods in Physics Research Section B: Beam Interactions with Materials and Atoms*, vol. 332, pp. 216–219, 2014.

[14] V. Tretyak, "Semi-empirical calculation of quenching factors for ions in scintillators," *Astroparticle Physics*, vol. 33, no. 1, pp. 40–53, 2010.

[15] D. Horn, G. Ball, A. Galindo-Uribarri, E. Hagberg, R. Walker, R. Laforest, and J. Pouliot, "The mass dependence of CsI (Tl) scintillation response to heavy ions," *Nuclear Instruments and Methods in Physics Research Section A: Accelerators, Spectrometers, Detectors and Associated Equipment*, vol. 320, no. 1, pp. 273–276, 1992.

[16] L. Papadopoulos, "Rise time of scintillation emission in inorganic and organic scintillators," *Nuclear Instruments and Methods in Physics Research Section A: Accelerators, Spectrometers, Detectors and Associated Equipment*, vol. 401, no. 2–3, pp. 322–328, 1997.

[17] L. Papadopoulos, "Scintillation response of organic and inorganic scintillators," *Nuclear Instruments and Methods in Physics Research Section A: Accelerators, Spectrometers, Detectors and Associated Equipment*, vol. 434, no. 2, pp. 337–344, 1999.

[18] W. Moses, S. Payne, W.-S. Choong, G. Hull, and B. Reutter, "Scintillator non-proportionality: Present understanding and future challenges," *Nuclear Science, IEEE Transactions on*, vol. 55, no. 3, pp. 1049–1053, 2008.

[19] A. N. Vasil'Ev, "From luminescence non-linearity to scintillation non-proportionality," *Nuclear Science, IEEE Transactions on*, vol. 55, no. 3, pp. 1054–1061, 2008.

[20] S. Payne, N. J. Cherepy, G. Hull, J. D. Valentine, W. W. Moses, W.-S. Choong, *et al.*, "Nonproportionality of scintillator detectors: theory and experiment," *Nuclear Science, IEEE Transactions on*, vol. 56, no. 4, pp. 2506–2512, 2009.

[21] W. Moses, G. Bizarri, R. Williams, S. Payne, A. Vasil'ev, J. Singh, Q. Li, J. Grim, and W.-S. Choong, "The origins of scintillator non-proportionality," *Nuclear Science, IEEE Transactions on*, vol. 59, no. 5, pp. 2038–2044, 2012.

[22] E. Rutherford, "LXXIX. The scattering of α and β particles by matter and the structure of the atom," *The London, Edinburgh, and Dublin Philosophical Magazine and Journal of Science*, vol. 21, no. 125, pp. 669–688, 1911.

[23] H. Bethe, "Zur Theorie des Durchgangs schneller Korpuskularstrahlen durch Materie," *Annalen der Physik*, vol. 397, no. 3, pp. 325–400, 1930.

[24] F. Bloch, "Zur Bremsung rasch bewegter Teilchen beim Durchgang durch Materie," *Annalen der Physik*, vol. 408, no. 3, pp. 285–320, 1933.

[25] B. Povh, M. Lavelle, K. Rith, C. Scholz, and F. Zetsche, *Particles and nuclei: an introduction to the physical concepts*. Springer Science & Business Media, seventh edition ed., 2015.

[26] P. A. Rodnyi, *Physical Processes in Inorganic Scintillators*. CRC Press LLC, 1 ed., 1997.

[27] J. F. Ziegler, M. D. Ziegler, and J. P. Biersack, "SRIM–The stopping and range of ions in matter (2010)," *Nuclear Instruments and Methods in Physics Research Section B: Beam Interactions with Materials and Atoms*, vol. 268, no. 11, pp. 1818–1823, 2010. Software Version SRIM-2013.00, `http://www.SRIM.org/`.

[28] J. Ziegler, "The electronic and nuclear stopping of energetic ions," *Applied Physics Letters*, vol. 31, no. 8, pp. 544–546, 1977.

[29] W. M. Yen, H. Yamamoto, *et al.*, *Fundamentals of Phosphors*. CRC press, 2006.

[30] T. Sidot, "Sur les propriétés de la blende hexagonale," *Comptes rendus de l'Académie des sciences*, vol. 63, pp. 188–189, 1866.

[31] F. Becchetti, C. Thorn, and M. Levine, "Response of plastic scintillator detectors to heavy ions, Z ≤ 35, E ≤ 170 MeV," *Nuclear Instruments and Methods*, vol. 138, no. 1, pp. 93–104, 1976.

[32] S. Ahlen, B. G. Cartwright, and G. Tarlé, "Return to unsaturated response of polymeric scintillators excited by relativistic heavy ions," *Nuclear Instruments and Methods*, vol. 147, no. 2, pp. 321–328, 1977.

[33] C. Pédrini, "Scintillation mechanisms and limiting factors on each step of relaxation of electronic excitations," *Physics of the Solid State*, vol. 47, no. 8, pp. 1406–1411, 2005.

[34] M. Weber, "Scintillation: mechanisms and new crystals," *Nuclear Instruments and Methods in Physics Research Section A: Accelerators, Spectrometers, Detectors and Associated Equipment*, vol. 527, pp. 9–14, jul 2004.

[35] P. Lecoq, A. Annenkov, A. Gektin, M. Korzhik, and C. Pedrini, *Inorganic scintillators for detector systems: physical principles and crystal engineering*. Springer Science & Business Media, 1 ed., 2006.

[36] H. Kuzmany, *Solid-state spectroscopy: an introduction*. Springer Science & Business Media, 2009.

[37] D. Meschede, *Gerthsen Physik*. Springer-Verlag, 2015.

[38] A. Meyer and R. Murray, "Effect of energetic secondary electrons on the scintillation process in alkali halide crystals," *Physical Review*, vol. 128, no. 1, p. 98, 1962.

[39] R. Katz, F. A. Cucinotta, and C. Zhang, "The calculation of radial dose from heavy ions: predictions of biological action cross sections," *Nuclear Instruments and Methods in Physics Research Section B: Beam Interactions with Materials and Atoms*, vol. 107, no. 1, pp. 287–291, 1996.

[40] K. Nakamura, P. D. Group, *et al.*, "Review of particle physics," *Journal of Physics G: Nuclear and Particle Physics*, vol. 37, no. 7A, p. 075021, 2010.

[41] Kanaya, K and Okayama, S, "Penetration and energy-loss theory of electrons in solid targets," *Journal of Physics D: Applied Physics*, vol. 5, no. 1, p. 43, 1972.

[42] G. Ising, "Prinzip einer Methode zur Herstellung von Kanalstrahlen hoher Voltzahl," *Ark. Mat. Astron. Fys.*, vol. 18, pp. 1–4, 1924.

[43] J. Cockcroft and E. Walton, "Experiments with high velocity positive ions," *Proceedings of the Royal Society of London. Series A, Containing Papers of a Mathematical and Physical Character*, pp. 477–489, 1930.

[44] R. J. Van De Graaff, "A 1,500,000 volt electrostatic generator," *Physical Review A*, vol. 38, pp. 1919–1920, 1931.

[45] F. Hinterberger, *Physik der Teilchenbeschleuniger und Ionenoptik*. Springer-Verlag, 2008.

[46] R. Wideröe, "Über ein neues Prinzip zur Herstellung hoher Spannungen," *Archiv für Elektrotechnik*, vol. 21, no. 4, pp. 387–406, 1928.

[47] L. W. Alvarez, "The design of a proton linear accelerator," in *Physical Review*, vol. 70(9-10), pp. 799–800, American Phyiscal Soc One Physics Ellipse, College PK, MD 20740-3844 USA, 1946.

[48] P. Bryant, "Introduction to Accelerators." Lecture notes, Joint Universities Accelerator School (JUAS), 2013.

[49] I. Kapchinskiy and V. Teplyakov, "Linear Ion Accelerator With Spatially Homogeneous Strong Focusing," *Pribory i Tekhnika Eksperimenta*, no. 2, p. 322, 1970.

[50] T. Sieber, *Entwicklung von 4-Rod-und IH-Radio-Frequenz-Quadrupol (RFQ)-Beschleunigern für radioaktive Ionenstrahlen bei REX-ISOLDE und MAFF*. PhD thesis, Ludwig-Maximilians-Universität München, 2001. `https://edoc.ub.uni-muenchen.de/455/1/Sieber_Thomas.pdf`, [prior: December 2015].

[51] R. Singh, *Tune Measurement at GSI SIS-18: Methods and Applications*. PhD thesis, Technische Universität, Darmstadt, July 2013. `http://tuprints.ulb.tu-darmstadt.de/id/eprint/3976`, [prior: July 2015].

[52] T. Perron and L. Farvacque, "Injection / Extraction." Lecture notes, Joint Universities Accelerator School (JUAS), 2013.

[53] P. Forck, H. Eickhoff, A. Peters, and A. Dolinskii, "Measurements and improvements of the time structure of a slowly extracted beam from a synchrotron," in *Proceedings of 7th European Particle Accelerator Conference (EPAC)* (J. Laclare, W. Mitaroff, C. Petit-Jean-Genaz, J. Poole, and M. Regler, eds.), (Vienna (Austria)), pp. 2237–2239, 2000.

[54] G. Rees, "Extraction," *CAS CERN accelerator school: 5 general accelerator physics course Vol 2*, p. 537, 1994. European Organization for Nuclear Research (CERN).

[55] S. Derenzo, M. Weber, E. Bourret-Courchesne, and M. Klintenberg, "The quest for the ideal inorganic scintillator," *Nuclear Instruments and Methods in Physics Research Section A: Accelerators, Spectrometers, Detectors and Associated Equipment*, vol. 505, no. 1, pp. 111–117, 2003.

[56] R. Haseitl, C. Andre, F. Becker, and P. Forck, "BeamView - A Data Acquisition System for Optical Beam Instrumentation," in *Proceedings of 7th international workshop on Personal Computers and Particle Accelerator Controls (PC@PAC)*, vol. 8, (Ljubljana, Slovenia), 2008.

[57] P. Strehl, *Beam instrumentation and diagnostics*, vol. 120. Springer, 2006.

[58] P. Forck, "Lecture notes on beam instrumentation and diagnostics, Joint Universities Accelerator School (JUAS), `http://www-bd.gsi.de/conf/juas/juas_script.pdf`, GSI Darmstadt, Germany." Script, 2011.

[59] W. R. Leo, *Techniques for nuclear and particle physics experiments*. Springer, 1994.

[60] M. Schwickert, C. Andre, F. Becker, P. Forck, T. G. E. Guetlich, T. Hoffmann, A. Lieberwirth, S. Loechner, A. Reiter, B. Voss, *et al.*, "Transverse Beam Profiling for FAIR," in *Proceedings of 2nd International Beam Instrumentation Conference (IBIC)* (I. Martin and G. Rehm, eds.), (Oxford, United Kingdom), pp. 232–234, 2013.

[61] L. Wartski, J. Marcou, and S. Roland, "Detection of Optical Transition Radiation and Its Application to Beam Diagnostics," *Nuclear Science, IEEE Transactions on*, vol. 20, pp. 544–548, June 1973.

[62] S. Shionoya, W. M. Yen, T. Hase, *et al.*, *Phosphor handbook*, vol. 1. CRC press, 1999.

[63] S. Wang, O. Laudi, H. Lucks, K. Wickersheim, and R. Buchanan, "X-Ray Image Intensifier Tubes Using Rare Earth Oxysulfide Phosphors," *Nuclear Science, IEEE Transactions on*, vol. 17, pp. 49–56, Feb 1970.

[64] K. Wickersheim, R. Alves, and R. Buchanan, "Rare Earth Oxysulfide X-Ray Phosphors," *Nuclear Science, IEEE Transactions on*, vol. 17, pp. 57–60, Feb 1970.

[65] E. Gorokhova, V. Demidenko, S. Mikhrin, P. Rodnyi, and C. van Eijk, "Luminescence and scintillation properties of Gd2O2S: Tb Ce ceramics," *IEEE Transactions on Nuclear Science*, vol. 52, pp. 3129–3132, 2005.

[66] S. Safai, S. Lin, and E. Pedroni, "Development of an inorganic scintillating mixture for proton beam verification dosimetry," *Physics in Medicine and Biology*, vol. 49, no. 19, p. 4637, 2004.

[67] A. Koch and H. Rosenfeldt, "Powder-phosphor screens combined with interference filters for X-ray imaging with increased brightness," *Nuclear Instruments and Methods in Physics Research Section A: Accelerators, Spectrometers, Detectors and Associated Equipment*, vol. 432, no. 2, pp. 358 – 363, 1999.

[68] K. Y. Sasaki and J. B. Talbot, "Deposition of Powder Phosphors for Information Displays," *Advanced Materials*, vol. 11, no. 2, pp. 91–105, 1999.

[69] ProXiVision GmbH, Bensheim, Germany, `http://www.proxivision.de/`, prior: July 2015.

[70] G. Chen, Y. Yang, D. Zhao, F. Xia, S. Baccaro, A. Cecilia, and M. Nikl, "Composition Effects on Optical Properties of Tb3+-Doped Heavy Germanate Glasses," *Journal of the American Ceramic Society*, vol. 88, no. 2, pp. 293–296, 2005.

[71] J. Mares, M. Nikl, K. Nitsch, N. Solovieva, A. Krasnikov, and S. Zazubovich, "A role of Gd 3+ in scintillating processes in Tb-doped Na–Gd phosphate glasses," *Journal of luminescence*, vol. 94, pp. 321–324, 2001.

[72] A. A. da Silva, M. A. Cebim, and M. R. Davolos, "Excitation mechanisms and effects of dopant concentration in Gd2O2S:Tb3+ phosphor," *Journal of Luminescence*, vol. 128, no. 7, pp. 1165 – 1168, 2008.

[73] L. G. V. Uitert, D. A. Pinnow, and J. C. Williams, "Photoluminescent Conversion of Laser Light for Black and White and Multicolor Displays. 1: Materials," *Applied Optics*, vol. 10, pp. 150–153, Jan 1971.

[74] R. C. Linares, "Growth of garnet laser crystals," *Solid State Communications*, vol. 2, no. 8, pp. 229 – 231, 1964.

[75] A. E. Paladino and B. D. Roiter, "Czochralski Growth of Yttrium-Gallium Garnet," *Journal of the American Ceramic Society*, vol. 49, no. 1, pp. 51–51, 1966.

[76] J. Rubin and L. Van Uitert, "Growth of sapphire and ruby by the Czochralski technique," *Materials Research Bulletin*, vol. 1, no. 3, pp. 211 – 214, 1966.

[77] J. Koningstein and O. Mortensen, "Laser-excited phonon Raman spectrum of garnets," *Journal of Molecular Spectroscopy*, vol. 27, no. 1, pp. 343 – 350, 1968.

[78] G. Mace, G. Schaack, T. Ng, and J. Koningstein, "Optical phonons of terbium-, dysprosium-, and ytterbium-garnet," *Zeitschrift für Physik*, vol. 230, no. 5, pp. 391–402, 1970.

[79] J. Santos, E. Silva, D. Sampaio, N. Souza, Y. Alves, and R. Silva, "Radioluminescence emission of YAG:RE laser-sintered ceramics," *Materials Letters*, vol. 160, pp. 456–458, 2015.

[80] Crytur spol. s r.o., Turnov, Czech Republic, `http://www.crytur.cz/`, prior: July 2015.

[81] Saint-Gobain Crystals, Hiram (OH), USA, `http://www.crystals.saint-gobain.com/`, prior: July 2015.

[82] T. Ludziejewski, M. Moszyński, M. Kapusta, D. Wolski, W. Klamra, and K. Moszyńska, "Investigation of some scintillation properties of YAG:Ce crystals," *Nuclear Instruments and Methods in Physics Research Section A: Accelerators, Spectrometers, Detectors and Associated Equipment*, vol. 398, no. 2, pp. 287 – 294, 1997.

[83] E. Zych, C. Brecher, and H. Lingertat, "Depletion of high-energy carriers in YAG optical ceramic materials," *Spectrochimica Acta Part A: Molecular and Biomolecular Spectroscopy*, vol. 54, no. 11, pp. 1771 – 1777, 1998.

[84] A. Murokh, J. Rosenzweig, V. Yakimenko, E. Johnson, and X. Wang, "Limitations on the resolution of YAG:Ce beam profile monitor for high brightness electron beam," in *The Physics of High Brightness Beams*, vol. 1, pp. 564–580, World Scientific, 2000.

[85] E. Zych, C. Brecher, A. Wojtowicz, and H. Lingertat, "Luminescence properties of Ce-activated YAG optical ceramic scintillator materials," *Journal of luminescence*, vol. 75, no. 3, pp. 193–203, 1997.

[86] V. Bachmann, C. Ronda, and A. Meijerink, "Temperature quenching of yellow Ce3+ luminescence in YAG:Ce," *Chemistry of Materials*, vol. 21, no. 10, pp. 2077–2084, 2009.

[87] E. Mihokova, M. Nikl, J. Mareš, A. Beitlerova, A. Vedda, K. Nejezchleb, K. Blažek, and C. D'Ambrosio, "Luminescence and scintillation properties of YAG:Ce single crystal and optical ceramics," *Journal of luminescence*, vol. 126, no. 1, pp. 77–80, 2007.

[88] C. Johnson, "The development and use of alumina ceramic fluorescent screens (CM-P00059425)," tech. rep., European Laboratory for Particle Physics Report CERN, 1990.

[89] S. Lederer, *Strahlenschäden in Szintillator-Materialien für die Hochstrom-Diagnose von Schwerionenstrahlen*. PhD thesis, TU Darmstadt, 2016. `http://tuprints.ulb.tu-darmstadt.de/id/eprint/5282`, [accessed personally, February 2016].

[90] A. Misra, H. Bist, M. Navati, R. Thareja, and J. Narayan, "Thin film of aluminum oxide through pulsed laser deposition: a micro-Raman study," *Materials Science and Engineering: B*, vol. 79, no. 1, pp. 49–54, 2001.

[91] S. Porto and R. Krishnan, "Raman effect of corundum," *The Journal of Chemical Physics*, vol. 47, no. 3, pp. 1009–1012, 1967.

[92] BCE Special Ceramics GmbH, Mannheim, Germany, `http://www.bce-special-ceramics.de/`, prior: July 2015.

[93] Dr. T. Prescher (2015), *personal communication*, BCE Special Ceramics, Mannheim, Germany.

[94] B. D. Evans, "A review of the optical properties of anion lattice vacancies, and electrical conduction in α-Al 2 O 3: their relation to radiation-induced electrical degradation," *Journal of nuclear materials*, vol. 219, pp. 202–223, 1995.

[95] K. J. McCarthy, J. G. López, F. M. Hernández, B. Zurro, A. Baciero, and M. Respaldiza, "The response of a chromium doped alumina screen to kev and mev ions," *Journal of Nuclear Materials*, vol. 321, no. 1, pp. 78–83, 2003.

[96] GSI Helmholtzzentrum für Schwerionenforschung GmbH, edited by A. Lieberwirth.

[97] H. Reeg (2013), *personal communication*, GSI Helmholtzzentrum für Schwerionenforschung GmbH - LOBI, Darmstadt, Germany.

[98] P. Forck, T. Hoffmann, and A. Peters, "Detectors for slowly extracted heavy ions at the GSI facility," in *Proceedings of 3rd European Workshop on Beam Diagnostics and Instrumentation for Particle ACcelerators (DIPAC)* (A. Ghigo, M. Giabbai, and G. Possanza, eds.), (Frascati, Italy), 1997.

[99] H. Reeg, "A current digitizer for ionisation chambers/sems with high resolution and fast response," in *Proceedings of 4th European Workshop on Beam Diagnostics and Instrumentation for Particle ACcelerators (DIPAC)DIPAC Proceedings* (B. Martlew and R. Smith, eds.), (Chester, United Kingdom), p. 147, 1999.

[100] A. Reiter, "Calibration of IFC current-to-frequency converters for slow-extraction reference detectors at HTP." GSI Helmholtzzentrum für Schwerionenforschung GmbH - LOBI, internal report, January 2015.

[101] Berger Lahr, "IclA easy." Software Version V1.106 Release 01.08.2007.

[102] European Machine Vision Association, "EMVA Standard 1288 3.0," tech. rep., European Machine Vision Association, november 2010. `http://www.emva.org/`.

[103] Stemmer Imaging GmbH, *Das Handbuch der Bildverarbeitung*. Stemmer Imaging GmbH, 2013.

[104] Allied Vision Technologies GmbH (2008), AVT Marlin Technical Manual V2.4.0, Stadtroda (Germany), `https://www.alliedvision.com/`, prior: January 2014.

[105] Allied Vision Technologies GmbH (2012), AVT Stingray Technical Manual V4.4.4, Stadtroda (Germany), `https://www.alliedvision.com/`, prior: January 2014.

[106] D. Gardner, "Characterizing Digital Cameras with the Photon Transfer Curve." Application Note. Summit Imaging, `http://www.couriertronics.com/docs/notes/cameras_application_notes/Photon_Transfer_Curve_Charactrization_Method.pdf`, Accessed:(26 June 2012).

[107] Kodak Image Sensor Solutions, "CCD Image Sensor Noise Sources." Application Note Rev. 2.1, 2005.

[108] A. Belousov, *Radiation Effects on Semiconductor Devices in High Energy Heavy Ion Accelerators*. PhD thesis, Technische Universität, Darmstadt, November 2014.

[109] HOYA CORPORATION USA Optics Division, Milpitas (CA), USA, , `http://www.hoyaoptics.com/`, prior: November 2014.

[110] HORIBA Europe GmbH, Darmstadt, Germany, `http://www.horiba.com/`, prior: July 2015.

[111] HORIBA Europe GmbH, Darmstadt, Germany, `http://www.horiba.com/scientific/products/optics-tutorial/monochromators-spectrographs/`, prior: August 2015.

[112] F. Kohlrausch, "Praktische Physik 2: Magnetismus, Optik, Radioaktivität, Strahlung, Struktur und Eigenschaften Von Materie," *Teubner, Stuttgart*, vol. 24, 1996.

[113] O. B. Tarasov and D. Bazin, "LISE++: a simulation of fragment seperators." Software Version V9.9.4 Release 10.04.2015, `http://lise.nscl.msu.edu/lise.html`.

[114] W. H. Press, *Numerical recipes 3rd edition: The art of scientific computing*. Cambridge university press, 2007.

[115] R. Taylor, "Interpretation of the Correlation Coefficient: A Basic Review," *Journal of Diagnostic Medical Sonography*, vol. 6, no. 1, pp. 35–39, 1990.

[116] V. Blobel and E. Lohrmann, *Statistische und numerische Methoden der Datenanalyse*. Teubner Verlag, 1998.

[117] J. Chappell and S. Murray, "Relative efficiencies and physical characteristics for a selected group of x-ray phosphors," *Nuclear Instruments and Methods in Physics Research*, vol. 221, no. 1, pp. 159–167, 1984.

[118] J. Moy, A. Koch, and M. Nielsen, "Conversion efficiency and time response of phosphors for fast x-ray imaging with synchrotron radiation," *Nuclear Instruments and Methods in Physics Research Section A: Accelerators, Spectrometers, Detectors and Associated Equipment*, vol. 326, no. 3, pp. 581–586, 1993.

[119] M. Pârlog, B. Borderie, M. Rivet, G. Tăbăcaru, A. Chbihi, M. Elouardi, N. Le Neindre, O. Lopez, E. Plagnol, L. Tassan-Got, *et al.*, "Response of CsI (Tl) scintillators over a large range in energy and atomic number of ions. Part II: calibration and identification in the INDRA array," *Nuclear Instruments and Methods in Physics Research Section A: Accelerators, Spectrometers, Detectors and Associated Equipment*, vol. 482, no. 3, pp. 693–706, 2002.

[120] A. F. Holleman and E. Wiberg, *Lehrbuch der Anorganischen Chemie*. Walter de Gruyter, 102 ed., 2007.

[121] S. Lederer, S. Akhmadaliev, J. von Borany, E. Gütlich, A. Lieberwirth, J. Zimmermann, and W. Ensinger, "High-temperature scintillation of alumina under 32 MeV ^{63}Cu^{5+} heavy-ion irradiation," *Nuclear Instruments and Methods in Physics Research Section B: Beam Interactions with Materials and Atoms*, vol. 359, pp. 161 – 166, 2015.

[122] G.-L. Lin, "The Energy Measurement of Ultrahigh Energy Cosmic Rays," 2005. (chinese), `http://ir.nctu.edu.tw/handle/11536/90881/`, prior: March 2016.

[123] T. Liu, F. Chang, C. Chen, M. Huang, W.-Y. Hwang, and G. Lin, "FLASH-TW experiment status report," in *International Cosmic Ray Conference*, vol. 8, p. 275, 2005.

[124] K. Ushida, H. Shibata, S. Tagawa, Y. Yoshida, K. Kimura, and A. Kira, "Characteristics of phosphor used for beam monitoring: Intensity growth of scintillation and long-lived residual emission observed on steady state γ-radiolysis," *Applied radiation and isotopes*, vol. 49, no. 1, pp. 55–58, 1998.

[125] M. Kakudo and N. Kasai, *X-ray diffraction by macromolecules*. Kodansha Limited and Springer-Verlag, 2005.

[126] Perkin Elmar Lambda 800/900 User's Guide, 2001.

[127] D. Skoog, D. West, F. Holler, and S. Crouch, *Fundamentals of analytical chemistry*. Cengage Learning, 2013.

[128] Dr. J. Brötz (2015), *personal communication*, TU Darmstadt, Departement of Structure Research, Germany.

[129] D. A. Skoog and J. J. Leary, *Instrumentelle Analytik: Grundlagen-Geräte-Anwendungen*. Springer-Verlag, 2013.

[130] B. McGaw, *Instrumentation in analytical chemistry,* vol. 2. Chichester, United Kingdom: Ellis Horwood Ltd., 1995.

[131] I. De Wolf, "Micro-Raman spectroscopy to study local mechanical stress in silicon integrated circuits," *Semiconductor Science and Technology,* vol. 11, no. 2, p. 139, 1996.

[132] B. Schrader, *Infrared and Raman spectroscopy: methods and applications*. John Wiley & Sons, 1995.

[133] Y. Chen, P. Lim, S. Lim, Y. Yang, L. Hu, H. Chiang, and W. Tse, "Raman scattering investigation of Yb: YAG crystals grown by the Czochralski method," *Journal of Raman Spectroscopy*, vol. 34, no. 11, pp. 882–885, 2003.

[134] HORIBA Jobin Yvon GmbH (2001), LabRAM Series Brochure, Bensheim, Germany.

[135] X. Yan, *Phosphors for lighting applications*. PhD thesis, Brunel University (London, UK), 2012. `http://bura.brunel.ac.uk/handle/2438/6954/`, prior: December 2015.

List of Figures

List of Tables

List of Abbrevations

A999   **A**luminum oxide Al_2O_3 with **9**9**.99** % purity

AF995R   Screen from Desmarquest Co., sintered **a**luminum oxide (**f**lourescent), **99.5** % Al_2O_3, doped with 0.5 % chromium oxide (**r**uby)

CCD   **C**harge **c**oupled **d**evice

FAIR   **F**acility for **A**ntiporoton and **I**on **R**esearch

FODO   **Fo**cosuing -**D**efocusing quadrupole structure

GSI   **GSI** Helmholzzentrum für Schwerionenforschung GmbH, formerly: Gesellschaft für Schwerionenforschung mbH

HEBT   **H**igh **e**nergy **b**eam **t**ransfer, section after SIS18

HTP   **H**igh energy **t**arget hall dum**p**

HTPDT1   **HTP d**iagnostic **t**ransformer **1**

HTPDI1I   **HTP di**agnostic chamber **1 I**onization chamber

HTPDI1S   **HTP di**agnostic chamber **1 S**econdary electron emission monitor

IC   **I**onization **c**hamber

LASER   **L**ight **a**mplification by **s**timulated **e**mission of **r**adiation

LED   **L**ight-**e**mitting **d**iode

LINAC   **Lin**ear **Ac**celerator

P43   Commercially available **p**hosphor type, short for $Gd_2O_2S{:}Tb$

P46   Commercially available **p**hosphor type, short for $Y_3Al_5O_{12}{:}Ce$

ppp   **P**articles **p**er **p**ulse

RE   **R**are **e**arth

RF   **R**adio **f**requency

RFQ   **R**adio **f**requency **q**uadrupole

ROI   **R**egion **o**f **i**nterest

RT   **R**esonant **t**ransformer

SEM	**S**econdary **e**lectron emission **m**onitor
SIS18	**S**chwer**i**onen **S**ynchrotron, heavy ion synchrotron, at GSI
UNILAC	**Uni**versal **l**inear **ac**celerator, at GSI
UV/Vis	**U**ltraviolet-**vis**ible range of spectrum
XRD	**X**-**r**ay **d**iffraction
YAG:Ce	short for **Y**ttrium **A**luminum **G**arnet doped with **Ce**rium, single crystal, chemical composition: $Y_3Al_5O_{12}$:Ce

Appendix

A.1 Parts of Developed Python 2.7 Source Code

A source code was developed in Python (version 2.7) to perform a generalized analysis on the measured data. To give an overview of the developed data processing, parts of the code will be reported in the following sections. The source code will not be given in its full amount to avoid an excessive number of pages with partly repetitive and/or intuitive commands. Instead code blocks will be presented in summarized style to explain the general motivation of the programming. They will be given in numbered boxes labeled with *Listing*. Listings that contain functions or classes will start with the according call of the function (or class, respectively) and exemplary choice of variables. After one blank line, the definition of the function (or class, respectively) will be given.

Five aspects of the image processing will be described closer, namely

- Initial Image Processing - Import Recorded Image as Array

- Noise Reduction

- Calculation of Beam Profiles and Statistical Moments

- Plot of Data with Varying Beam Intensity and Linear Regression

- Extrapolation of Spectral Efficiency of PCO1600

Initial Image Processing - Import Recorded Image as Array

The code starts with the sorting of picture pairs into background image and the record of scintillation (in general abbreviated with `spot`). This is performed for a row of files in a given directory. An integer number (index) in the start can be used to choose the picture for start of processing in the directory. Afterwards both images, background and spot, are imported as array. The dimensions of this array are given by the chip, i.e. image size of the recording camera, as given in table A.1.

Table A.1: Image size for recording cameras in used record mode

camera	image size [pixel]
AVT Marlin	656x494
AVT Stingray	656x492
PCO 1600	1600x1200

Due to the bias angle of the target ladder to the beam direction, the vertical axis of the images were recorded bigger as they were in reality. Thus, this axis is compressed by help of the `Image` package from the Python Image Library (`PIL`). The code is listed in listing L.1.

Listing L.1: Read-in process for png files

```python
array_spot = read_single_png(file_spot,tilting_angle=entry.tilting_angle)

from PIL import Image
def read_single_png(fname,workdir='',tilting_angle=0.0):
        plain_img = Image.open(workdir+fname)
        if ( tilting_angle != 0.0 ):
                width,height = plain_img.size
                tilting_factor = 1/numpy.sin(tilting_angle*2*numpy.pi/360.0)
                new_height = numpy.int(height/tilting_factor)
                new_img = numpy.asfarray(plain_img.resize((width,new_height)))*
                    tilting_factor
        else:
                new_img = numpy.asfarray(plain_img)
        return new_img
```

As shown in row 6 of listing L.1, the axis compression is only executed in case that the parameter for the bias angle `tilting_angle` is not equal to zero. Than, a `tilting_factor` is calculated, according to equation (4.3) (see section 4.2) and the image is resized by the `Image` package. The `tilting_factor` is again used in row 10 to normalize the resized image (`new_img`) to the original sum of area and so to the originally recorded light output L.

Noise Reduction

As explained in section 4.2 the experimental environment has an influence on the measurements. Especially the CCD chip in the recording camera can show characteristic noise types (see especially section 4.2.1). Nevertheless, most characteristics can be deleted from the recorded images, i.e. from the imported arrays `array_spot`. The code performs noise reduction in the following order:

1. Background subtraction: `array_background` is subtracted (directly) from `array_spot`, as shown in listing L.2. One requirement is that both arrays need to have the same dimensions. Otherwise a standard error is raised.

Listing L.2: Detailed description of general calculations

```python
subtr_background(array_spot, array_background)

def subtr_background(ndarray_img,ndarray_bg):
        return ndarray_img - ndarray_bg
```

Some background subtraction methods, different to listing L.2, were tested as well. In the alternative way, the horizontal and vertical projections of `array_spot` were calculated first. In a second step the calculated background profile was subtracted from the beam profile. As shown in figure A.2 both methods showed the same beam profiles in the end and the same sum of area was calculated, independent from the chosen method. For the figure, a randomly chosen beam record

was used and the profiles in horizontal and vertical direction were calculated in both methods. However, the method of listing L.2 was chosen for the general image processing, because hot and cold pixels, recognized in the background picture, could be used as general two dimensional map of defect pixels. This was regarded as advantage in contrary to a preceding calculation of projections, where on the one hand two dimensional positions of defect pixels will be lost and on the other hand hot and cold pixels in one row / column of the image would have compensate to a wrong background level.
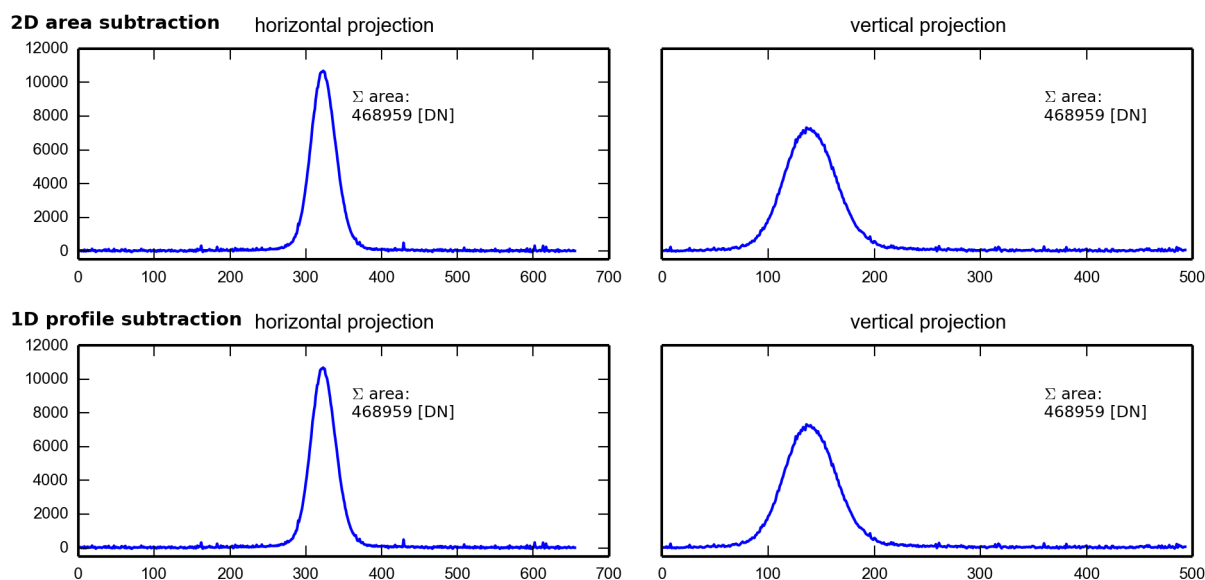
Figure A.2: Result of different background subtraction modes for horizontal and vertical profiles, all without set of ROI

2. Region Of Interest (ROI): To reduce the remaining noise after step 1 a two dimensional ROI was set. For images from camera #1 an ellipse was defined around the beam spot, using the parameters `width` and `height` around a middle point with `xmiddle` and `ymiddle`. The code is presented in listing L.3.

Listing L.3: Cut of a ROI with elliptical shape

```
1  cut_roi_2d(img=result, middle=roi_middle, width=roi_width, height=roi_height)
2
3  def cut_roi_2d(img,middle,height,width,sensitivity=10):
4          ymiddle,xmiddle = middle
5          mask = numpy.zeros_like(img)
6          y,x = numpy.mgrid[0:img.shape[0],0:img.shape[1]]
7          mask[y,x] = numpy.sqrt( (x-xmiddle)**2/(width/sensitivity)**2 + (y-
                ymiddle)**2/(height/sensitivity)**2 ) <= sensitivity
8          return mask*img
```

Line 6 shows the calculation of meshed grids (`numpy.mgrid[start,stop]`), which are defined as two arrays with equidistant cell values. The cell values are equal to the position in the row/column. The first and third given parameters (here zero) define the value to start the counting over the grid. The

second and fourth parameters `img.shape[0]` and `img.shape[1]` tell where to stop the counting and simultaneously give the size of the grids. One mesh grid is counted row-wise (increments from top to bottom), the other one is counted column-wise (from left to right). In the developed code for image processing, the grids were used as coordinates in y and x direction.

The limits of the ROI were calculated in line 6 by using the mathematical condition of an elliptical area. Here the `sensitivity` was introduced, to avoid roughness of the ROI at the border. The `sensitivity` was tested with different values and the value `sensitivity=10` was found as best choice for the recorded data. Each point, fulfilling the mathematically condition in line 7, was set `True` or 1.0, respectively. Since all other positions of the mask were set to Zero by definition in line 5 the calculated result `mask*img` in line 8 corresponded to the ROI cut of the image.

Different methods to cut a ROI of an image were tested and the results are given in figure A.3 for comparison. The figure shows the beam projection in horizontal axis for single images during nickel and xenon beam times as example. Two different cameras were used for record (*AVT Marlin* and *AVT Stingray*). Even though a lot of pixels were already defect on the CCD of "cam 1", it recorded during more than 50 % beam times. Shortly before xenon beam time the replacement of "cam 1" through "cam 3" became necessary. Pictures from both cameras were used for comparison of the ROI cut to investigate the result for different noise levels.
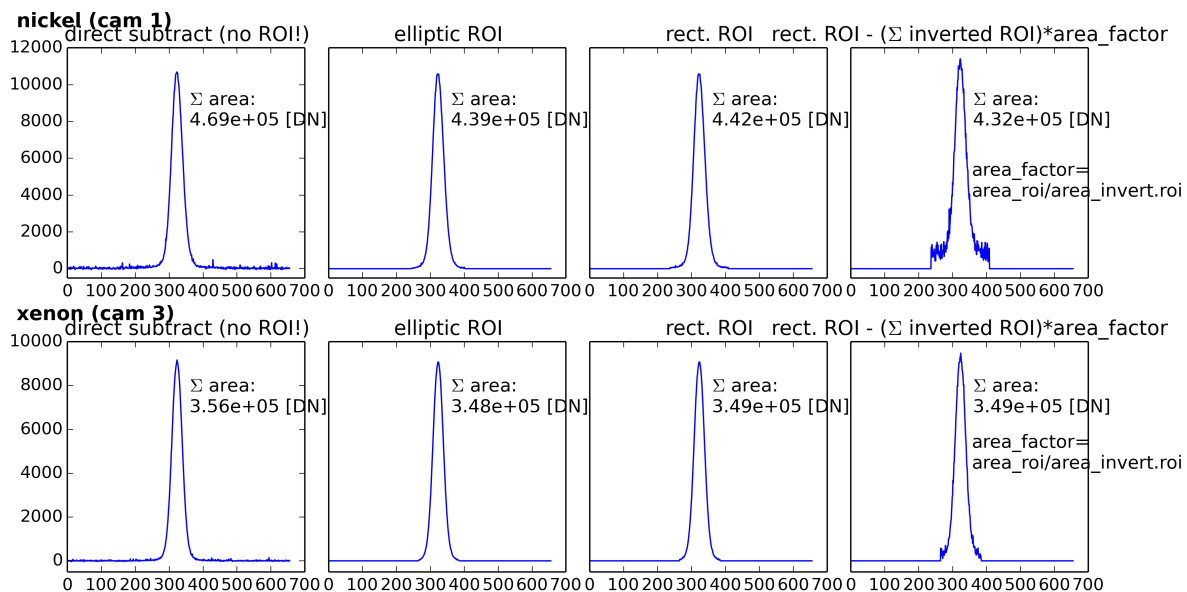
Figure A.3: Different methods of ROI set and resulting sum of area, chosen method for the investigations is 'elliptic ROI'

In the first column of figure A.3, a simple beam projection without cut of a ROI is given as reference. The second column shows the performed cut with an elliptical ROI, while for the third column a rectangular ROI was used. The rectangular ROI resulted in a higher value of total area, as result from remaining noise in the ROI edges. The last row in figure A.3 shows a complete different method of noise reduction: Here a rectangular ROI was cut from the measurement (i.e. from `array_spot`) and a value was subtracted that corresponds to the background outside the ROI, but

normalized to the ROI area. As can be seen, this algorithm does not result in a completely wrong sum of area, but a high noise level is left in the foot of the projected profile.

Images from camera #2 (*PCO 1600*) recorded the emission spectra as function of wavelength and the ROI was defined as rectangular, as shown in listing L.4 with intuitive parameters.

Listing L.4: Cut of a rectangular ROI

```
result = result[roi_vertical_start:roi_vertical_end,roi_horizontal_start:
    roi_horizontal_end]
```

3. Normalization to the optical setup: To calculate a factor for the original scintillation output from the targets, the transmission through the iris and the neutral density filter (if used, see sections 4.2 and 4) were multiplied and the preprocessed array `picarray` was normalized to it. The code is shown in listing L.5.

Listing L.5: Calibration to iris setting and neutral density filter

```
entry.overall_calculation_factor = entry.iris_transmission_value * entry.
    optical_filter_value
optical_scale(result,entry.overall_calculation_factor)

def optical_scale(picarray,scalefactor):
        return picarray/scalefactor
```

Listing L.5 is only important for measurements with camera #1. For camera #2 no optical filter was used and the iris was not changed during measurements. Here the `entry.overall_calculation_factor` was set to 1.0 per default.

From these results, the light output L and the light yield Y were calculated for single pulses, analog to equations (5.1) and (5.3). The according code is listed below.

Listing L.6: Calculation of light output and light yield

```
light_output = numpy.sum(result)

deposited_energy = entry.de_dx_total
light_yield = (light_output)/(deposited_energy*specific_beam_intensity)
```

In order to decrease the influence of data outliers, the light yield Y for the measurements with increasing beam intensities was calculated analog to equation 5.4 by use of the determined slope m_L. A description will be given in the next section.

Plot of Data with Varying Beam Intensity and Linear Regression

---

The calculated results were exported as table into an ASCII file. The table included also the time stamp of record and the beam pulse intensity. The ASCII file were named group-wise by dedicated and user-defined names to avoid repetition. As example: All data of P43 phosphor #1

recorded with camera #1 during beam time with fast extracted Xenon pulses were named with `p43pv_7e7_fast_cam3-htp_cam3grey`. All ASCII files were exported in directories with well-defined tree structure. The data trees were defined by, *date of beam time projectile, specific beam energy* as well as by investigated characteristic (e.g. *light output*).

Using the preliminary defined file names, the data tables were then imported and plotted in different styles (e.g. light output L as function of beam intensity, light yield Y for different targets in slow extraction mode and so on). In general, the data plots were exported into PNG images.

The method for the plot of one data group is explained in listing L.7. The function called all investigated characteristics, i.e. light output L, light yield Y, beam profiles and the second statistical moments at once and exported it into a PNG image. For simplicity only the plot method of light output L as function of number of irradiated particles is shown here and the remaining methods work analog.

Line 3 tests, if the previously explained data tree does contain data or is existing at all. In lines 5 to 7 the data tables are imported from the ASCII files and sorted in increasing order by the beam intensities. The indices of outliers can be given by the parameter `outliers_lightoutput` and will be deleted from the data in line 11. The different data types, according to x, Δx, y and Δy values, are defined as variables in lines 14 to 17. Even though this step is redundant, it gives a better overview. Besides it can be supportive during an eventual manipulation, e.g. to shift the beam intensities to lower or higher values due to wrong estimated measurements (see section 4.1.2). The window that contains the plot (`figure`) is started in line 21, while line 20 defines the path and file name of the exported data image.

A try-except-block is initiated in line 23. Here the imported data set is given to a dedicated function `linear_fit([...,...],...)` for linear data regression (see listing L.8 and according description) and the calculated parameters (slope `popt_lin[0]`, error of slope `err_m_sys` and coefficient of determination `cofdet`) are used to plot the data points on the one hand and a line, corresponding to the linear regression, on the other hand. Most of the calculated parameters are exported into an ASCII file and an Excel data sheet and are printed additionally in the console. If any of the steps in lines 24 to 36 can not be executed, e.g. due to an error, the conditions of the except block are executed. Here, some messages are printed in the console, as can be seen in lines 38 and 39.

From line 40 on (outside the try-except-block) some graphical parameters for the figure are defined, e.g. the title of the plot window and the axis labeling. Line 48 adjusts the whitespace around the plot window. The parameters were set empirically to use the full size of the exported PNG image effectively. Line 49 exports the graphical data with a 300 dpi resolution into the path, given in line 20. The window is closed in line 50.

Listing L.7: Plot algorithm for one data group

```
1  def plot_group_of_one_target(first_session_element,outliers_lightoutput=None,
       outliers_statmom=None,figsize=(def_figure_width,0.75*def_figure_width)):
2          # create or find export string (path of files)
3          first_session_element.initexport()
4          # read in and sort data files
5          file_to_plot_lightoutput = open(first_session_element.export_dir_calc+'
               lightoutput/'+first_session_element.exportstring_calc+'-lightoutput.txt
               ','r')
```

```python
        array_lightoutput = numpy.genfromtxt(file_to_plot_lightoutput,delimiter='\
            t',usecols=(2,3,4,9,10),names=('intensity','lightoutput','lightyield','
            error_nsr','error_intensity'))
        array_lightoutput = numpy.sort(array_lightoutput,axis=0,order='intensity')

        # remove outliers, given by parameters outliers_lightoutput
        if (outliers_lightoutput is not None):
                array_lightoutput = numpy.delete(array_lightoutput,
                    outliers_lightoutput)


        # define parameters beam intensity, lightoutput and errors by choice of
            column
        beam_intensities = array_lightoutput['intensity']
        error_x = array_lightoutput['error_intensity']
        lightoutput = array_lightoutput['lightoutput']
        error_y_rel = array_lightoutput['error_nsr']


        # figure
        path_of_figure = first_session_element.export_dir_pictures+'lightoutput/'
            + str(first_session_element.extr_mode) + '_' + str(int(
            first_session_element.beam_energy/1.0e3)) + 'MeV/'+
            first_session_element.exportstring_calc+'-lightoutput.png'
        plt.figure(figsize=figsize)
        # linear regression - make it before plot, so that I can use the resulting
             equation within legendbox
        try:
                popt_lin, lin_fit_func, perr_lin = linear_fit([beam_intensities,
                    lightoutput],datayerrors=(error_y_rel*lightoutput),dataxerrors=
                    error_x,force_zero_intercept=True)
                (err_m_sys,err_b_sys), cofdet = perr_lin
                plt.plot(beam_intensities,lin_fit_func,marker='',linestyle='--',
                    label='L=(%.3g$\pm$%.2g)*ppp ($R^2$=%.2f%%)'%(popt_lin[0],
                    err_m_sys,cofdet*100.0))
                deposited_energy = first_session_element.de_dx_total
                print >>first_session_element.export_file_log,
                    first_session_element.exportstring_calc, 'overall lightyield
                    calculated from slope m divided by (dE/dx * delta x): ' + str(
                    popt_lin[0]/(deposited_energy))   # + ', error: ' + str(numpy.
                    diag(pcov_fit)[0]/(deposited_energy))
                print >>first_session_element.export_file_log, 'y-axis intercept
                    from lightoutput (if y = m*x+b, than intercept is b): ' + str(
                    popt_lin[1]) # + ', error: %.1f %%'%(100.0*numpy.sqrt(numpy.
                    diag(pcov_fit))[1]/popt_lin[1])
                print >>first_session_element.export_file_log, 'x-axis intercept
                    from lightoutput (if y = m*x+b = 0, than intercept is -b/m): '
                    + str(-popt_lin[1]/popt_lin[0])
```

```python
                # write calculated data to export file
                write_to_export_table(wb_filename='file_export_results_lightyield.
                    xlsx',targetname=first_session_element.target_name,projectile=
                    str(first_session_element.req_ion)+'_'+str(
                    first_session_element.extr_mode)+'_'+str(first_session_element.
                    year)+'_'+str(first_session_element.month),z_number=
                    first_session_element.atomic_number,slope_l=popt_lin[0],
                    dep_energy=deposited_energy,yield_y=(popt_lin[0]/(
                    deposited_energy)),err_slope_ml=err_m_sys,rsquared=cofdet,
                    err_camera=numpy.average(error_y_rel),err_ppp_rel=numpy.average
                    (numpy.divide(error_x,beam_intensities)))
                print str(first_session_element.exportstring_calc) + ' overall
                    lightyield calculated from slope m divided by (dE/dx * delta x)
                    : %.2e'%(popt_lin[0]/(deposited_energy))
                print str(first_session_element.exportstring_calc) + 'y-axis
                    intercept from lightoutput (if y = m*x+b, than intercept is b):
                     ' + str(popt_lin[1])      # + ', error: %.1f %%'%(100.0*numpy.
                    sqrt(numpy.diag(pcov_fit))[1]/popt_lin[1])
                print str(first_session_element.exportstring_calc) + ': x-axis
                    intercept from lightoutput (if y = m*x+b = 0, than intercept is
                     -b/m): %.2e'%(-popt_lin[1]/popt_lin[0])
                print '\n'
        except:
                print 'linear fit failed for lightoutput of ' + str(
                    first_session_element.exportstring_calc)
                print >>first_session_element.export_file_log, str(datetime.
                    datetime.now()) + ' - ' + 'linear fit failed for lightoutput of
                     ' + str(first_session_element.exportstring_calc)
    plt.title(str(first_session_element.target_name)+ ' - ' + str(
        first_session_element.extr_mode)+' extraction', **title_font)
    plt.xlabel('number of irradiated particles per pulse [ppp]', **axis_font)
    plt.gca().set_xscale('log')
    plt.ylabel('light output $L$ (arb.u.)', **axis_font)
    plt.gca().set_yscale('log')
    plt.xticks(**axis_font)
    plt.yticks(**axis_font)
    plt.legend(loc="upper left", prop=font_prop)
    plt.tight_layout(rect=(-0.04,-0.07,1.05,1.05))
    plt.savefig(path_of_figure,dpi=300)
    plt.close()
```

In line 24 of listing L.7 the call of a linear regression was introduced as part of a try-except-block. The command is repeated in line 1 of listing L.8 to give a better overview. For a successful continuation of the image processing, it is necessary to delete clear outliers from the data. Since the PNG images are exported in log-log-presentation, negative data values are not shown, which is why a preliminary check is performed in lines 6 to 10, using the function `find_negative_error_values` (see set of parameters in line 4). If the x- or the y-data contain any negative values, a message with the according data indices will be printed in the console and it is recommended to repeat the plot command after the adjustment of the parameter for outliers.

At the end of the preliminary check, the data set is given to a dedicated fitting algorithm, called `linear_fit_weight_twodim_bootstrap`, which is shown in lines 13 to 93. This function is weighted in two dimensions by a bootstrap method (for mathematical explanations, see e.g. reference [114]). The method shifts the given data points by a value, that is maximum as big as the given errors (lines 44 till 59). As can be seen from line 44 on, the absolute value of the shift is generated randomly and the regression parameters are calculated over a number of 100 sets (line 43). Afterwards, the slope and intercept (`mean_pcov`) are calculated as average (line 70). The error of slope and intercept (`perr_bootstrap`, i.e. `err_pfit`) is calculated as standard deviation value within a confidence interval `Nsigma` in line 74. Additionally, `linear_fit_weight_twodim_bootstrap(...)` calculates the coefficient of determination `rsquared_bootstrap`, i.e. the factor of goodness of the calculated regression parameters to the set data points (see [114] and [115] for mathematical details).

Listing L.8: Algorithm of linear regression

```
1  popt_lin, lin_fit_func, perr_lin = linear_fit([beam_intensities,lightoutput],
       datayerrors=(error_y_rel*lightoutput),dataxerrors=error_x,force_zero_intercept=
       True)
2  (err_m_sys,err_b_sys), cofdet = perr_lin
3
4  def linear_fit(data, p0=None, datayerrors=None, dataxerrors=None,
       force_zero_intercept=False,**kwargs):
5          are_there_more_outliers = find_negative_error_values(dataxerrors,
               datayerrors)
6          try:
7                  are_there_more_outliers[0]
8                  print 'you have to delete more outliers: ',
                       are_there_more_outliers
9          except:
10                 pass
11         return linear_fit_weight_twodim_bootstrap(data, p0, datayerrors,
               dataxerrors, force_zero_intercept=force_zero_intercept,**kwargs)
12
13 def linear_fit_weight_twodim_bootstrap(data, p0=None, datayerrors=None,
       dataxerrors=None, force_zero_intercept=False, **kwargs):
14         datax, datay = data
15         if (datayerrors == None):
16                 datayerrors = numpy.ones_like(datay)
```

```python
        # define function and create first parameter estimation
        if (force_zero_intercept == False):
                linear_function = lambda params, x: params[0] * x + params[1]     #
                        create fitting function of form mx+b
        else:
                linear_function = lambda params, x: params[0] * x     #create
                        fitting function of form mx
                errfunc = lambda p, x, y: linear_function(p, x) - y               #
                        create error function for least squares fit

        init_a = 0.5                             #find initial value for a (
            gradient)
        if (force_zero_intercept == False):
                init_b = min(datay)                          #find initial value
                        for b (y axis intersection)
                p0 = numpy.array((init_a, init_b))  #bundle initial values in
                        initial parameters
        else:
                p0 = numpy.array((init_a,0.0))         #bundle initial values in
                        initial parameters

        #first calculation of leastsq estimation
        pfit, pcov, infodict, errmsg, success = leastsq( errfunc, p0.copy(), args
            =(datax, datay), full_output=True)

        residuals = errfunc( pfit, datax, datay)
        s_res = numpy.std(residuals)
        ps = []
        ps_cov = []
        chisq = []
        rsquared_bs = []
        rsquared_bs_k = []
        # 100 random data sets are generated and fitted
        for i in range(100):
                if datayerrors is None:
                        randomDelta = numpy.random.normal(0., s_res, len(datay))
                        randomdataY = datay + randomDelta
                else:
                        randomDelta =  numpy.array( [ \
                        numpy.random.normal(0., derr,1)[0] \
                                for derr in datayerrors ] )
                        randomdataY = datay + randomDelta
                if dataxerrors is None:
                        randomDelta = numpy.random.normal(0., s_res, len(datax))
                        randomdataX = datax + randomDelta
```

```python
                else:
                        randomDelta =  numpy.array( [ \
                        numpy.random.normal(0., derr,1)[0] \
                                for derr in dataxerrors ] )
                        randomdataX = datax + randomDelta
                randomfit, randomcov, randominfodict, randomerrmsg, randomsuccess
                    = leastsq( errfunc, p0, args=(randomdataX, randomdataY),
                    full_output=True)
                ps.append( randomfit )
                ps_cov.append( randomcov )
                chisq.append( (errfunc(randomfit, datax, randomdataY)**2).sum() )
                rsquared_temp = 1-( (randominfodict['fvec']**2).sum() / ((
                    randomdataY-randomdataY.mean())**2).sum() )
                rsquared_bs.append( rsquared_temp )
                rsquared_korr_temp = 1-(( (randominfodict['fvec']**2).sum() /(len(
                    randomdataY)-len(p0)-1))/( ((randomdataY-randomdataY.mean())
                    **2).sum() /(len(randomdataY)-len(p0))))
                rsquared_bs_k.append( rsquared_korr_temp )

        ps = numpy.array(ps)
        mean_pfit = numpy.mean(ps,0)
        Nsigma = 1. # 1sigma gets approximately the same as methods above
                                # 1sigma corresponds to 68.3% confidence interval
                                # 2sigma corresponds to 95.44% confidence interval
        err_pfit = Nsigma * numpy.std(ps,0)

        # calculation of statistical errors of leastsq fit
        if force_zero_intercept == True:
                mean_pcov = 1.0
        else:
                ps_cov = numpy.array(ps_cov)
                mean_pcov = numpy.sqrt(numpy.diag( numpy.mean(ps_cov,0) ))

        pfit_bootstrap = mean_pfit
        perr_bootstrap = err_pfit
        perr_statistic = mean_pcov
        s_sq_bootstrap = numpy.mean(chisq)
        rsquared_bootstrap = numpy.mean(rsquared_bs)
        rsquared_korr_bootstrap = numpy.mean(rsquared_bs_k)

        # function to plot
        f_plot = linear_function(pfit_bootstrap, datax)

        return pfit_bootstrap, f_plot, (perr_bootstrap, rsquared_bootstrap)
```

The two dimensional beam response of the screens, recorded by camera #1, was calculated into the horizontal and vertical profiles. The code is shown exemplarily in listing L.9 only for the calculation in horizontal axis. For the vertical axis, the calculation was performed similarly.

The boolean parameter `norm` is used to normalize the calculated profile to a maximum value of 1.0. This code was also used to calculate the emission spectra from the images recorded with the PCO 1600 camera.

Listing L.9: Calculation horizontal image projection , for vertical projection the axis choice is '1'

```
def make_profile_horizontal(picarray,norm=False):
        if (norm == False):
                result = numpy.sum(picarray,axis=0)
        elif (norm == True):
                result = numpy.sum(picarray,axis=0)/numpy.max(result)
        return result
```

The so calculated beam profiles were analyzed for investigations in the first and second statistical moments (see section 5.2). The source codes, used for calculations, are given below. The code follows the mathematical definition, given in equation (5.6) for a one dimensional profile (line 1-3) and a two dimensional profile (line 5-7). For the one dimensional profile, the position is defined as array with equal size, as the profile and with equidistant entries (`numpy.mgrid`, see definition of ROI in listing L.3).

Listing L.10: Weighted mean value of a 1D profile - 1st statistical moment

```
def calc_xmean(profile):
        result = numpy.sum(numpy.multiply(profile,numpy.mgrid[0:numpy.shape(
            profile)[0]]))/numpy.sum(profile)
        return result

def calc_2d_xmean(data):
        position, profile = data
        result = numpy.sum(numpy.multiply(profile,position))/numpy.sum(profile)
        return result
```

For the calculation of second statistical moment σ, the position of the data points is given as number `i` and the profile distribution has a specific length of `len(profile)`. The weighting of each point was than given as `profile[i]`. The dominator corresponds to the light output, here calculated with `numpy.sum(profile)`. The code is given in listing L.11 in line 1-9. Here the calculation was not performed in a single line, to avoid the calculation with negative values (see line 6). For two dimensional profiles the single line algorithm is used in line 11 till 15, similar to listing L.10.

Listing L.11: Weighted standard deviation of a 1D profile - 2nd statistical moment

```
def calc_stdvariance(profile):
    return numpy.sqrt(calc_variance(profile))
def calc_variance(profile):
```

```
4        mu = calc_xmean(profile)
5        result = 0
6        for i in numpy.argwhere(profile>=0):
7                result = result + profile[i]*(i-mu)**2
8        result = result/numpy.sum(profile)
9        return result
10
11 def calc_2d_stdvariance(data):
12        position, profile = data
13        mu = calc_2d_xmean(data)
14        result = numpy.sqrt(numpy.sum(numpy.multiply(profile,numpy.multiply((
             position - mu),(position - mu))))/numpy.sum(profile))
15        return result
```

Extrapolation of Spectral Efficiency of PCO1600

The used spectrometer setup consisted of different optical components (see section 4.2). The spectral efficiency of each component (lens, camera CCD and spectrometer) was used to calculate the total efficiency. Since the single efficiencies started and ended at different points, the total efficiency was calculated as an extrapolation. The code and explaining comments are given in listing L.12.

Listing L.12: Extrapolation of PC1600 Quantum Efficiency below 400 nm

```
1 # import of necessary packages
2 import numpy
3 import matplotlib.pyplot as plt
4 import matplotlib.font_manager as font_manager
5 from scipy.interpolate import interp1d
6 from scipy.interpolate import UnivariateSpline
7 # read in transmission-file - used DataGrabber application to create txt-file with
       coordinates
8 pco_withmicrolenses = numpy.genfromtxt('../../various spectras and transmissions/
     cameras/pco1600_monochrome_withmicrolensescover.txt'),skiprows=4,names=['
     wavelength','intensity'])
9 pco_withmicrolenses_lambda = pco_withmicrolenses['wavelength']
10 pco_withmicrolenses_eff = pco_withmicrolenses['intensity']
11 # generate interpolation / function of given data for further calculations
12 pco_withmicrolenses_interpol_f = interp1d(x=pco_withmicrolenses_lambda,y=
     pco_withmicrolenses_eff,kind='linear')
13 new_wavelength_range_with = numpy.linspace(pco_withmicrolenses_lambda[0],
     pco_withmicrolenses_lambda[-1],num=numpy.shape(pco_withmicrolenses_lambda)[0])
14 with_interpol_array = pco_withmicrolenses_interpol_f(new_wavelength_range_with)
15 # create extrapolation by use of UnivariateSpline, k gives the degree of the
       interpolation polynomial
16 with_interpol_expand_f = UnivariateSpline(x=pco_withmicrolenses_lambda, y=
     pco_withmicrolenses_eff, k=4)
```

```python
17  # set first entry of 'with_interpol_array' to the same value as second entry (for
        some reason, it's 'nan')
18  with_interpol_array[0] = with_interpol_array[1]
19  # calculate residuals of original data sheet from calculated Spline to calculate
        back to original values later
20  with_interpol_expand_array_residuals = numpy.divide(with_interpol_array,
        with_interpol_expand_f(new_wavelength_range_with))
21  new_wavelength_expand = numpy.insert(new_wavelength_range_with, 0, numpy.arange
        (200.0, new_wavelength_range_with[0], step=(new_wavelength_range_with[1]-
        new_wavelength_range_with[0])))
22  delta_x_range = numpy.shape(new_wavelength_expand)[0] - numpy.shape(
        new_wavelength_range_with)[0]
23  # interpolate expanded wavelength range to Spline function
24  with_interpol_expand_array = with_interpol_expand_f(new_wavelength_expand)
25  # set right part of curve to original values
26  with_interpol_expand_array[(delta_x_range-1):-1] = numpy.multiply(
        with_interpol_expand_array[(delta_x_range-1):-1],
        with_interpol_expand_array_residuals)
27  # there is a jump of values now! recalculate the left side of Spline-array down
        with help of first residual value
28  with_interpol_expand_array[0:(delta_x_range-1)] = with_interpol_expand_array[0:(
        delta_x_range-1)]*with_interpol_expand_array_residuals[1]
29  # set first entries (appr. till lambda=300 nm) to a minimum value = value of end
        of the curve:
30  with_interpol_expand_array[0:620] = with_interpol_array[-1]
31  # save to txt file
32  numpy.savetxt(fname=open('pco1600_monochrome_withcover_expanded.txt','w'), X=numpy
        .array([new_wavelength_expand, with_interpol_expand_array]).T, delimiter='\t')
33  # plot foldings together
34  plt.figure()
35  plt.plot(new_wavelength_range_with,with_interpol_array, label='with microlenses -
        from datasheet')
36  plt.plot(new_wavelength_expand,with_interpol_expand_array, label='with microlenses
        - expanded forward to 200nm')
37  plt.xlabel('wavelength [nm]')
38  plt.ylabel('quantum efficiency')
39  font_prop = font_manager.FontProperties(fname='C:\Windows\Fonts\Arial.ttf', size
        =12)
40  plt.legend(loc='upper right', prop=font_prop)
41  plt.ylim(0.0,0.75)
42  plt.legend(loc='best')
43  plt.tight_layout(rect=(-0.01,-0.02,1.01,1.02))
44  plt.show()
```

A.2 Danksagung

Bei der Erarbeitung meiner Promotion gab es in den letzten vier Jahren viele positive Einflüsse und zahlreiche Untersützer. Für Beides möchte ich mich an dieser Stelle bedanken. Alle Namen einzeln zu nennen, würde jedoch nicht nur den Rahmen sprengen: sicherlich würden - ohne böse Absicht - die ein oder anderen Namen dabei untergehen. Deshalb beschränke ich mich auf die Personen, die entscheidend beteiligt waren.

Zu allererst möchte ich Prof. Dr. Wolfgang Ensinger danken, der mir zusammen mit Dr. Peter Forck vom GSI Helmholtzzentrum für Schwerionenforschung GmbH die Arbeit an Projekt ermöglicht hat. Trotz seiner vielfältigen Aufgaben hat sich mein Doktorvater immer Zeit für die Besprechung meiner Fortschritte genommen.

An dieser Stelle möchte ich auch Prof. Dr. Oliver Kester für die Erarbeitung des Zweitgutachtens, sowie die Verlängerung meiner Beschäftigung über die ursprüngliche Projektzeit hinaus danken.

Die Promotion wäre nicht möglich gewesen ohne die Messungen am GSI Helmholtzzentrum für Schwerionenforschung GmbH. Für die Einführung in die komplexe Anlage und für viele wissenschaftlich angeregte Diskussionen möchte ich Dr. Peter Forck danken. Seinem Stellvertreter Dr. Thomas Sieber gilt besonderer Dank für seine Unterstützung bei meiner Promotionsschrift.

Bei Beata Walasek-Höhne und ihrer Gruppe *HEBT Instruments* möchte ich mich für die Unterstützung im Bereich Optik und Szintillationsaufnahme bedanken. Weitere Unterstützung bei der Datanaufnahme erhielt ich von der Gruppe *Data Acquisition and Software* unter Tobias Hoffmann und Rainer Haseitl. Hierfür und für die persönlichen Hilfestellungen während der Strahlzeiten möchte ich mich bei euch herzlich bedanken. Bei der Auswertung der Daten erhielt ich entscheidende Hilfe von Dr. Andreas Reiter, bei dem ich mich hier ebenso bedanken möchte, wie bei Manfred Hartung für die umfangreiche Konstruktion meiner Kamerahalterung. Für die reibungslose Zusammenarbeit mit der Gruppe *Accelerator Operations* und dem Operateurs-Team des Hauptkontrollraums möchte ich mich hier ebenfalls bedanken.

Auch Dr. Marcus Schwickert soll hier nicht ausbleiben: Trotzdem er als Leiter der Abteilung *LOBI* schon genug ausgelastet ist, nahm er sich stets für sehr hilfreiche persönliche Mitarbeitergespräche Zeit. Dafür ein großes Dankeschön.

Auch von den Mitarbeitern der *Materialanalytik* an der TU Darmstadt wurde ich aufgenommen und unterstützt, wofür ich mich bei der Gruppe bedanken möchte. Besonders hervorheben möchte ich die Zusammenarbeit mit meinem Kollegen Dr. Stephan Lederer. Ich habe ihn als geistreichen und zuverlässigen Materialwissenschaftler kennen und schätzen gelernt. Die Diskussionen während unserer Projekte waren immer hilfreich und gaben oft genug einen wichtigen Impuls für den nächsten Schritt.

Zu guter Letzt möchte ich auch meinen Freunden Dank aussprechen. Durch eure Unterstützung seid ihr für mich in den letzten Jahren zu einer zweiten Familie geworden. Dieser private Ausgleich, aber natürlich auch eure motivierenden Worte haben mich durch halten lassen, egal ob die Arbeit gerade gut lief oder sich mühsam dahin schleppte.

Personal Data   Alice Lieberwirth

Am Birkenwald 2

64390 Erzhausen

Tel.: 06 159/ 71 20 48

E-Mail: a.lieberwirth@gsi.de

born July, 5th 1985 in Frankfurt (Main)

School education

08/2001 – 04/2004   Final school examination - Ernst-Reuter-Schule I, Frankfurt (Main)

08/1995 – 06/2001   Secondary - Ernst-Reuter-Schule II, Frankfurt (Main)

08/1991 – 07/1995   Primary School - Heinrich-Kromer-Schule, Frankfurt (Main)

Academic Studies

09/2004 – 11/2011   Goethe University Frankfurt (Main), Physics (Diploma)

Graduation Studies

since 08/2012   Technische Universität Darmstadt, Material Science deperatement (Material Analysis Group)

A.4 Publications, Reports and Proceedings

List of Publications

- A. Lieberwirth, W. Ensinger, P. Forck, S. Lederer: "Response from inorganic scintillation screens induced by high energetic ions", *Nuclear Instruments and Methods in Physics Research Section B: Beam Interactions with Materials and Atoms* (2015), **365**, pp. 533 - 539. doi:10.1016/j.nimb.2015.07.111

- S. Lederer, S. Akhmadaliev, J. von Borany, E. Gütlich, A. Lieberwirth, J. Zimmermann, W. Ensinger: "High-temperature scintillation of alumina under 32 MeV $^{63}Cu^{5+}$ heavy-ion irradiation", *Nuclear Instruments and Methods in Physics Research Section B: Beam Interactions with Materials and Atoms* (2015), **359**, pp. 161 - 166. doi:10.1016/j.nimb.2015.07.131

- S. Lederer, S. Akhmadaliev, P. Forck, E. Gütlich, A. Lieberwirth, W. Ensinger: "Thermal annealing behavior of α-Al_2O_3 scintillation screens", *Nuclear Instruments and Methods in Physics Research Section B: Beam Interactions with Materials and Atoms* (2015), **365**, pp. 548 - 552. doi:10.1016/j.nimb.2015.08.024

List of Reports

- A. Lieberwirth, B. Walasek-Höhne, P. Forck, W. Ensinger: "Response of scintillating screens for fast and slow extracted beams from SIS18", *GSI Scientific Report 2012*, p. 283

- A. Lieberwirth, P. Forck, S. Lederer, W. Ensinger: "Light Output of Inorganic Scintillating Screens induced by Fast and Slow extracted Beams from SIS18", *GSI Scientific Report 2014*, p. 424, DOI:10.15120/GR-2015-1-FG-GENERAL-07

- A. Lieberwirth, P. Forck, S. Lederer, W. Ensinger: "Lumineschence Spectra of Inorganic Scintillating Screens induced by Fast and Slow extracted Beams from SIS18", *GSI Scientific Report 2014*, p. 425, DOI:10.15120/GR-2015-1-FG-GENERAL-08

- S. Lederer, P. Forck, E. Gütlich, A. Lieberwirth, W. Ensinger: "Luminescence degradation behavior of alumina irradiated with heavy ions of high fluences", *GSI Scientific Report 2014*, p. 261, DOI:10.15120/GR-2015-1-APPA-MML-MR-09

- P. Boutachkov, A. Reiter, C. Andre, H. Bräuning, C. Dorn, P. Forck, E-M. Glück, H. Graf, T. Hoffmann, V. S. Lavrik, A. Lieberwirth, Y. Shutko, and B. Walasek-Höhne: "In-beam Tests of PMTs and Voltage Dividers for Particle Detectors at FAIR", *GSI Scientific Report 2014*, p. 464, DOI:10.15120/GR-2015-1-FG-GENERAL-46

List of Proceedings

- A. Lieberwirth, W. Ensinger, P. Forck, B. Walasek-Höhne: "Response of Scintillating Screens to Fast and slow Extracted ion Beams", in Proceedings of *2nd International Beam Instrumentation Conference 2013 (IBIC'13)*, (J. Martin and G. Rehm, eds.), Oxford (United Kingdom), pp. 553-556.

- M. Schwickert, C. Andre, F. Becker, P.Forck, T. Giacomini, E. Gütlich, T.Hoffmann, A. Lieberwirth, S. Löchner, A. Reiter, B. Voss, B. Walasek-Höhne, M. Witthaus: "Transverse Beam Profiling for FAIR", in Proceedings of *2nd International Beam Instrumentation Conference 2013 (IBIC'13)*, (J. Martin and G. Rehm, eds.), Oxford (United Kingdom), pp. 232-234.

- P. Forck, C. Andre, C. Dorn, W. Ensinger, R. Haseitl, A. Lieberwirth, S. Lederer, S. Löchner, A. Reiter, M. Schwickert, T. Sieber, B. Walasek-Höhne, M. Witthaus: "Beam-based Tests of intercepting transverse profile diagnostics for FAIR", in Proceedings of *5th International Particle Accelerator Conference 2014 (IPAC'14)*, (C. Petit-Jean-Genaz and G. Arduini and P. Michel and V. Schaa, eds.), Dresden (Germany), pp. 3480-3482.

Erklärung zur Dissertation

Hiermit versichere ich, die vorliegende Dissertation ohne Hilfe Dritter nur mit den angegebenen Quellen und Hilfsmitteln angefertigt zu haben. Alle Stellen, die aus Quellen entnommen wurden, sind als solche kenntlich gemacht. Diese Arbeit hat in gleicher oder ähnlicher Form noch keiner Prüfungsbehörde vorgelegen.

Darmstadt, den 7. September 2016

_____

(Alice Lieberwirth)